

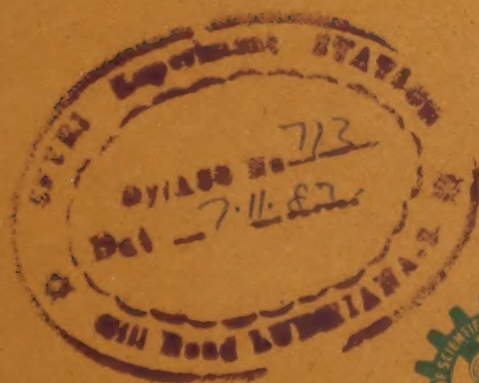
Lib  
①  
7/11/83  
Central Science Library  
Indian J Pure & Appl Phys, Vol 21 No. 8 pp. 435-492

AUGUST 1983

CODEN: IJOPAU ISSN: 0019-5596

21(8) 435-492 (1983)

# INDIAN JOURNAL OF PURE & APPLIED PHYSICS



Published by  
PUBLICATIONS & INFORMATION DIRECTORATE, CSIR  
NEW DELHI

in association with  
THE INDIAN NATIONAL SCIENCE ACADEMY, NEW DELHI





# Let us take pride in our achievements

**W**e grow enough to feed ourselves—no small achievement considering that India is the second most populous country in the world which had had to spend heavily on imports of foodgrains.

We are one of the leading industrialised nations of the world—we produce everything from radios to computers, needles to the most sophisticated machinery and equipment.

We have more trained scientists and technicians than any country in the world (except USA and USSR). Joint industrial ventures are being set up with our help, in many developing countries.



These achievements have given us the skill and ability to fulfil the tasks set out in the Five Year Plan and 20 Point Programme.

**We March Forward To  
A Confident Future**



# Indian Journal of Pure & Applied Physics

## EDITORIAL BOARD

Prof. D Basu  
Indian Association for  
the Cultivation of Science  
Calcutta

Prof. B Buti  
Physical Research Laboratory  
Ahmedabad

Prof. S C Dutta Roy  
Indian Institute of Technology  
New Delhi

Dr R Hradaynath  
Instruments Research & Development  
Establishment Dehra Dun

Prof. D Premaswarup  
Nagarjuna University  
Nagarjuna Nagar

Prof. A N Mitra  
Indian National Science Academy  
New Delhi/University of Delhi  
Delhi

Prof. Probir Roy  
Tata Institute of Fundamental  
Research  
Bombay

Prof. E S Raja Gopal  
Indian Institute of Science  
Bangalore

Prof. G Rajasekaran  
Madras University  
Madras

Dr A P B Sinha  
National Chemical Laboratory  
Pune

Prof. C V Vishveshwara  
Raman Research Institute  
Bangalore

Prof. M S Sodha  
Indian National Science Academy  
New Delhi/Indian Institute of  
Technology New Delhi

Shri Y.R. Chadha, Editor-in-Chief, *Ex-officio* Secretary

---

## EDITORIAL STAFF

### *Editors*

D S Sastry, K S Rangarajan & R P Goel

### *Assistant Editors*

G N Sarma, J B Dhawan & Tarun Banerjee

### *Scientific Assistant*

(Mrs) Poonam Bhatt

---

**Published by the Publications & Information Directorate, CSIR, Hillside Road, New Delhi 110012**

Editor-in-Chief: Y R Chadha

The Indian Journal of Pure & Applied Physics is issued monthly. The Directorate assumes no responsibility for the statements and opinions advanced by contributors. The editorial staff in its work of examining papers received for publication is assisted, in an honorary capacity, by a large number of distinguished scientists, working in various parts of India.

Communications regarding contributions for publication in the journal should be addressed to the Editor, Indian Journal of Pure & Applied Physics, Publications & Information Directorate, Hillside Road, New Delhi 110012.

Correspondence regarding subscriptions and advertisements should be addressed to the Sales & Distribution Officer, Publications & Information Directorate, New Delhi 110012.

### **Annual Subscription**

Rs. 120.00 £20.00 \$45.00

### **Single Copy**

Rs. 12.00 £2.00 \$4.50

50% Discount is admissible to research workers and students and 25% discount to non-research individuals, on annual subscription. Payments in respect of subscriptions and advertisements may be sent by cheque, bank draft, money order or postal order marked payable *only* to **Publications & Information Directorate, New Delhi 110012**. Claims for missing numbers of the journal will be allowed only if received within 3 months of the date of issue of the journal plus the time normally required for postal delivery of the journal and the claim.



## MEDICINAL & AROMATIC PLANTS ABSTRACTS

This bimonthly publication reports scientific information culled out from periodicals published from India and abroad on different aspects of medicinal and aromatic plants under classified subject heads with informative abstracts. Each issue includes about 350 abstracts with an exhaustive subject index.

MAPA will be an indispensable guide for the individual research workers, educational and research institutes, government agencies, industrial houses and men in drugs and perfumery industries. Subscription amount (Rs 40/-, \$ 17/-, £ 7/-) per annum may be remitted in favour of "PUBLICATIONS & INFORMATION DIRECTORATE", New Delhi 110012.

Manager (Sales & Advertisement)  
PUBLICATIONS & INFORMATION DIRECTORATE, CSIR  
Hillside Road, New Delhi 110012

### OUR PHYSICS PUBLICATIONS

FOR GRADUATE AND POST GRADUATE STUDENTS

- MATHEMATICAL PHYSICS
- HAND BOOK OF ELECTRONICS
- BASIC NUCLEAR PHYSICS AND COSMIC RAYS
- ESSENTIALS OF QUANTUM MECHANICS
- ADVANCED PRACTICAL PHYSICS VOL I & II
- SOLID STATE PHYSICS
- ELECTRICITY AND MAGNETISM
- ELECTRODYNAMICS
- RELATIVISTIC MECHANICS
- STATISTICAL MECHANICS
- CLASSICAL MECHANICS
- ELEMENTS OF SPECTROSCOPY
- VIVA-VOCE IN ADVANCED PHYSICS VOL I & II
- ELEMENTS OF GROUP-THEORY
- TRANSFORMS METHOD FOR ENGINEERS AND PHYSICISTS
- NON-NEWTONIAN FLUID FLOWS
- SPECIAL FUNCTIONS

Dr. Rajput B. S.  
Dr. Gupta S. L. & Dr. Kumar V.  
Dr. Srivastava B. N.  
Dr. Srivastava B. N.  
Singh S. P.  
Saxena B. S., Gupta R. C. & Saxena P. N.  
Dr. Gupta S. L., Singh S. P. & Dr. Kumar V.  
Dr. Gupta, S. L., Singh, S. P. & Dr. Kumar, V.  
Prakash S.  
Dr. Gupta S. L. & Dr. Kumar V.  
Dr. Gupta S. L., Dr. Kumar V. & Dr. Sharma R. C.  
Gupta R. C. & Saxena P. N.  
Dr. Karanda H. M.  
Dr. Mukhopadhyaya A. K.  
Prof Kapur J. N., Dr. Bhatt & Dr. Sacheti  
Dr. Sharma, Dr. Trivedi & Saran

- ELEMENTS OF MECHANICS
- THERMODYNAMICS & STATISTICAL PHYSICS
- HEAT AND THERMODYNAMICS
- OPTICS AND ATOMIC PHYSICS
- ELECTRICITY & ELECTRONICS
- ELECTRICITY & MAGNETISM
- MODERN PHYSICS
- PRACTICAL PHYSICS
- VIVA-VOCE IN PHYSICS

Agarwal & Prakash  
Sangal, Prakash & Agarwal  
Sangal, Prakash & Agarwal  
Singh & Agarwal  
Dr. Saxena, Prakash & Dr. Arora  
Dr. Saxena, Prakash & Dr. Arora  
Dr. Bansal, Madhani & Singh  
Dr. Gupta S. L. & Dr. Kumar V.  
Gupta R. C.

### HELP BOOKS

- MECHANICS
- HEAT AND THERMODYNAMICS
- OPTICS
- ELECTRICITY & MAGNETISM

Dr. Gupta S. L., Dr. Kumar V. & Dr. Sangal S. K.  
Dr. Gupta S. L., Dr. Kumar V. & Dr. Sangal S. K.  
Dr. Gupta S. L., Dr. Kumar V. & Dr. Sangal S. K.  
Dr. Gupta S. L., Dr. Kumar V. & Dr. Sangal S. K.

International  
Research Journal  
**ACTA CIENCIA  
INDICA**

FOR DETAILED CATALOGUE WRITE TO :  
**PRAGATI PRAKASHAN**  
61-63, Lajpat Rai Market, Begun Bridge, Meerut-250001

Available at all leading bookshellers throughout India.

RR Advtg Service 82/1/PP



# Indian Journal of Pure & Applied Physics

VOLUME 21

NUMBER 8

AUGUST 1983

## CONTENTS

### Solid State Physics

- Studies on Morphology and Habit of Gel-grown Alkaline Earth Metal Iodate Crystals ... 435  
M S Joshi\* & S G Trivedi

- Growth of High Purity Indium Antimonide Crystals for Infrared Detectors ... 441  
R K Bagai\*, G L Seth & W N Borle

### Chemical Physics

- CNDO/2 and INDO SCF Calculations on Polar Fluorobenzenes ... 445  
S D Sharma & S Doraiswamy\*

### Dielectrics & Microwaves

- Dielectric Studies & Structure of -NCO Group in some Isocyanates ... 453  
P Brahma & S K Roy\*

### Nuclear Physics

- Attenuation and Scattering Coefficients of  $\gamma$ -Rays through Compressed Powdered Clay ... 457  
A H El-Kamel, M H Saied & Al El-Attar\*

- Multiple Scattering of Gamma Rays in Semi-infinite Water ... 460  
J Swarup\*, L H Peshori & K K Uppal

### Spectroscopy

- Singlet-Singlet Absorption Spectra of 1-Amino- and 2-Methoxynaphthalenes ... 466  
O P Sharma, H S Bhatti, N V Unnikrishnan Nair & R D Singh\*

### NOTES

- Fermi Levels in MIS(n) Solar Cells ... 471  
K Sen\* & P S Mathur

- Magnetic Studies of the System  $\text{ZnFe}_{1-x}\text{Mn}_x\text{CrO}_4$  ... 473  
P S Jain & V S Darshane\*

- Structure of  $\text{As}_2\text{S}_3$  Glass ... 476  
A K Nandi & B Mukherjee\*

- Dependence of Mechanoluminescence on the Area of Newly Created Surfaces of Crystals ... 479  
B P Chandra\*, T R Chandraker & S V Deshpande

- Lattice Waves in bcc Transition Metals ... 481  
K C Gupta & R P S Rathore\*

- Hindered Rotation of the Terminal Group in a Schiff Base Mesogen HBT ... 484  
Jai Prakash\*, B Rai & Rahul

*Continued overleaf*



## CONTENTS

Study of $^{50}_{22}\text{Ti}$ Ion Tracks in Soda Glass ... ..	487
Subhash Chander, Shyam Kumar, J S Yadav, S K Gupta & A P Sharma*	
Electronic & Infrared Absorption Spectra of 3-Methylpyridazine ... ..	490
Narasimha H Ayachit, K Suryanarayana Rao & M A Shashidhar*	

---

\* The author to whom all correspondence is to be addressed is indicated by the (\*) mark.



## Studies on Morphology and Habit of Gel-grown Alkaline Earth Metal Iodate Crystals

M S JOSHI\* & S G TRIVEDI†

Department of Physics, Sardar Patel University, Vallabh Vidyanagar 388120

Received 23 June 1981; accepted 14 March 1983

Crystals of iodates of barium, strontium and calcium were grown in silica gels. Three grades—very transparent, translucent and opaque—of crystals having different morphologies and habits were obtained under different growth conditions. Effects of concentration of the reactants, pH of gel solution, ionic concentration, impurities, etc on habit modification are described and discussed. Prismatic, prismatic pyramidal and dendritic crystals of barium iodate; platy, prismatic, prismatic pyramidal, needles and lamellar crystals of strontium iodate; and prismatic, prismatic pyramidal and hopper crystals of calcium iodate, are illustrated and described. Correlation is established between the quality, habit, etc. with growth parameters.

### 1 Introduction

Substantial work has been done by many investigators<sup>1-8</sup> on crystal morphology and habit of a variety of crystals grown under different conditions by different methods. Crystal habit plays a vital role in growth of large, good quality, single crystals. Now-a-days, the crystal grower is more interested in finding explanations for habit modifications in artificially-grown crystals.

Habit of crystals is determined by the slowest growing faces. Gibbs<sup>9</sup> showed that for equilibrium form of crystals, these faces have the lowest energy. It has been observed that crystal habit is governed by kinetic rather than by equilibrium conditions. A number of factors, such as degree of supersaturation, nature of solvent, pH of gel medium, presence of impurities, etc., have significant influence on crystal habit. Growth of alkaline earth metal iodate crystals has been reported by the present authors<sup>10</sup>. A systematic study on habit of these crystals, with reference to growth conditions, is reported in this paper.

### 2 Experimental Details

Test tubes (single diffusion) and U-tubes (double diffusion) were used as crystallization vessels. Gels were prepared by mixing sodium metasilicate solution (sp. gr., 1.04) with either 2 N acetic acid or 1 N iodic acid. Barium chloride (0.025-0.1 M) or barium nitrate (0.025-0.1 M), strontium chloride (0.1-1.0 M), calcium chloride (0.5-0.2 M) and sodium iodate (0.1-0.4 M) were used as reactants. Here, *M* means molar mass.

### 3 Observations

#### 3.1 Crystals of Barium Iodate

3.1.1. *Prismatic pyramidal crystals*—Prismatic pyramidal crystals, like those shown in Figs. 1(a) and 1(b), were found to grow when barium chloride was used as one of the reactants. The majority of these crystals were opaque; only few crystals were fairly transparent. It is interesting to note that on these crystals {100} faces were fairly large, while  $m'\{110\}$  and  $p\{110\}$  faces were very small. Portions, (b) of all figures are the corresponding schematic diagrams.

When barium nitrate (mixed with a small amount of nitric acid) was used as a feed solution, a few prismatic pyramidal, transparent crystals were found to grow. Some of these are illustrated in Figs 2(a) and 2(b). This observation indicates that change of the reactant leads to habit modification. It is worthwhile to note that addition of nitric acid to barium nitrate helps in improving transparency of the crystals. Here, faces  $a\{100\}$  and  $b\{010\}$  are dominating, while faces  $v\{221\}$  and  $c\{001\}$  are very small.

In the later stage of growth, say after about two weeks, in the region far away from the gel-solution interface, another variety of transparent, well developed, prismatic pyramidal crystals, as shown in Figs 3(a) and 3(b), result. This suggests that slow growth rate favours more perfect crystals. On these crystal faces  $a\{100\}$  and  $n\{011\}$  are predominant.

The results described above were obtained in single diffusion experiments. No good crystals were obtained in double diffusion experiments.

3.1.2. *Dendritic growth*—In single diffusion experiments dendritic barium iodate crystals were usually found to grow at high concentrations of one or both the reactants. These crystals were opaque. In the early stage, concentration gradient of the reactant in the gel

† Present address: Department of Physics, Navyug Science College, Surat 395 005, Gujarat





Fig. 1a

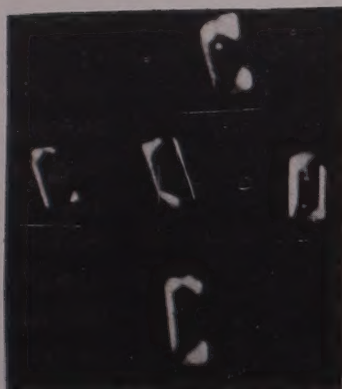


Fig. 2a



Fig. 3a

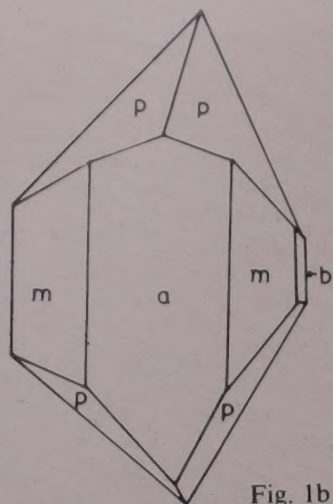


Fig. 1b

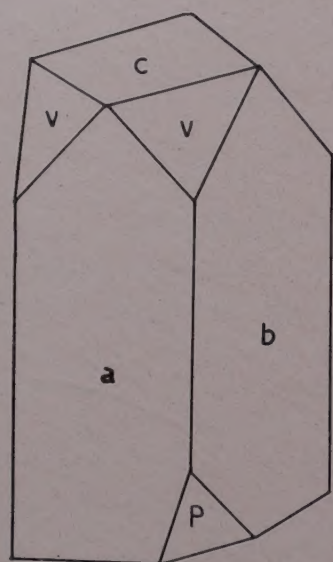


Fig. 2b

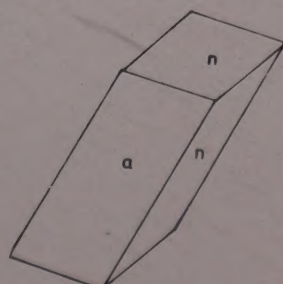


Fig. 3b

Figs 1-3—(a), Prismatic crystals of of barium iodate under different conditions; (b), corresponding schematic representation of the crystals

medium is very high which causes dendritic growth along fast growth directions. Similar results were obtained in double diffusion experiments also.

### 3.2 Crystals of strontium iodate

**3.2.1 Platy crystals**—In single diffusion experiments, at low concentration of sodium iodate in the gel, and at high concentration of strontium chloride above the gel, platy crystals, as shown in Figs 4(a) and 4(b), were found to grow. On these crystals, faces  $c\{001\}$  and  $m\{110\}$  are large, while faces  $d\{102\}$  are very small. Gel incorporation was often observed, without affecting the crystal morphology. These crystals were transparent except in the region of gel inclusion.

No platy crystals resulted in double diffusion experiments.

**3.2.2 Prismatic pyramidal crystals**—In single diffusion experiments at high concentration of sodium iodate in the gel and low concentration of strontium chloride above the gel, prismatic pyramidal crystals, as illustrated in Figs 5(a) and 5(b) and Figs 6(a) and 6(b), were found to grow. These crystals were transparent. On crystals illustrated in Figs 5(a) and 5(b)  $m\{110\}$  faces are very big, and  $r\{101\}$  faces are very small. On crystals illustrated in Figs 6(a) and 6(b) faces  $a\{100\}$  and  $b\{010\}$  predominate. These crystals look like almost prismatic crystals. Double diffusion experiments do not yield such crystals.

Another variety of prismatic pyramidal crystals, like those shown in Figs 7(a) and 7(b) and Figs 8(a) and 8(b), were also obtained. These transparent crystals grew when solution of strontium chloride was incorporated in the gel and a low concentration of sodium iodate feed solution was used. They resulted from single diffusion experiments. No such crystals were found to grow in the double diffusion experiments.

Figs 9(a) and 9(b) illustrate prismatic pyramidal crystals obtained by double diffusion experiments. These are distinctly different from prismatic pyramidal crystals described above. It is noteworthy that on these crystals, faces  $m\{110\}$ ,  $l\{120\}$ ,  $b\{010\}$ ,  $n\{011\}$  are fairly big, while faces  $p\{111\}$  are not well developed.

**3.2.3 Prismatic elongated crystals**—Figs 10(a) and 10(b) illustrate prismatic elongated crystals grown in the present investigation. Such crystals were obtained on using high concentrations of both the reactants, more so in the double diffusion experiments than in the single diffusion ones.

Habit changes of crystals illustrated in Figs 4-10 can be attributed to different concentration gradients of the reactants in different regions of the gel. All crystals referred to here were transparent.

**3.2.4 Lamellar and aggregate crystals**—In U-tube experiments, for all concentrations of both the reactants, lamellar and elongated, transparent crystals were found to grow in the limb containing sodium iodate solution. On the other hand, crystal aggregates were found to grow in the limb containing strontium chloride. Figs 11 and 12 illustrate lamellar crystals and crystal aggregates respectively. The lamellar crystals have uneven surfaces which are divided into several strips.

**3.2.5 Small needle crystals**—In single diffusion experiments, needle-shaped transparent crystals were found to grow in gels set with iodic acid when strontium chloride, with low concentration, was used as a feed solution. Fig. 13 shows some of these crystals.

It may be noted that no such crystals were obtained in double diffusion experiments.





Fig. 4a

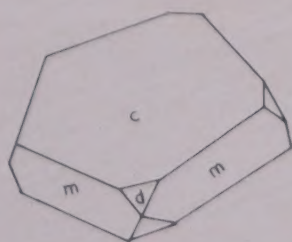


Fig. 4b



Fig. 8a

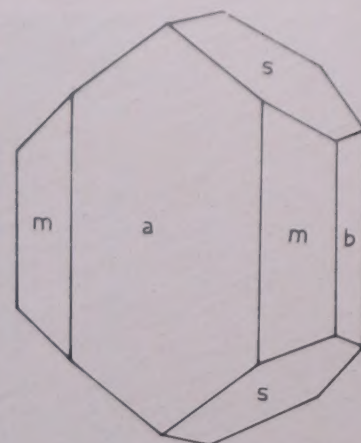


Fig. 8b



Fig. 5a

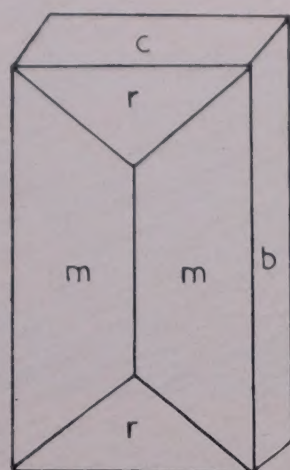


Fig. 5b



Fig. 9a

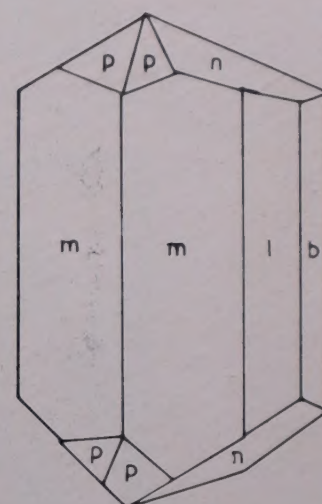


Fig. 9b



Fig. 6a

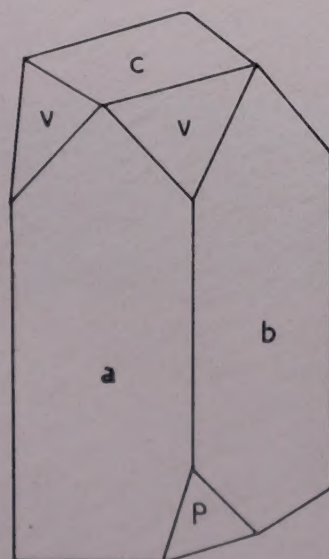


Fig. 6b



Fig. 10a

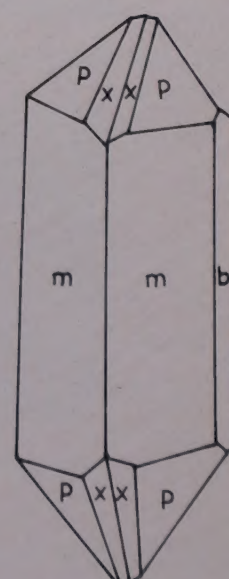


Fig. 10b



Fig. 7a

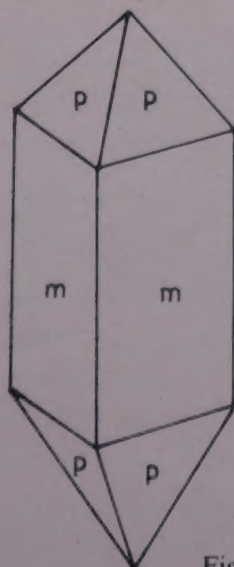


Fig. 7b

Figs 4-10—Crystals of strontium iodate under different conditions [(a); Fig. 4, platy crystals; Figs 5 & 6, prismatic crystals; Figs 7-10, prismatic pyramidal crystals; (b), corresponding schematic representation of the crystals]



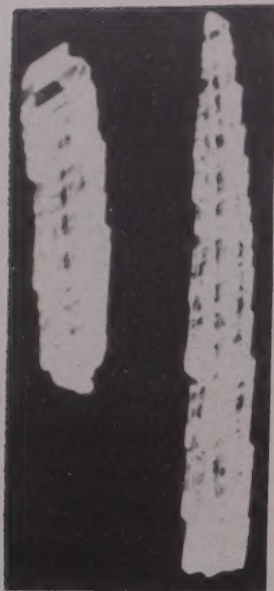


Fig. 11—Lamellar elongated crystals of strontium iodate



Fig. 12—Aggregate crystals of strontium iodate

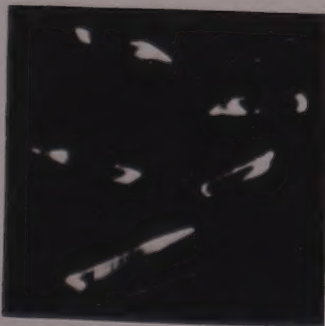


Fig. 13—Needle-shaped crystals of strontium iodate



Fig. 14a

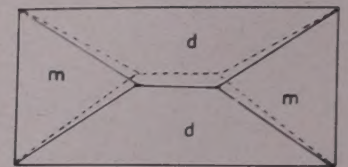


Fig. 14b

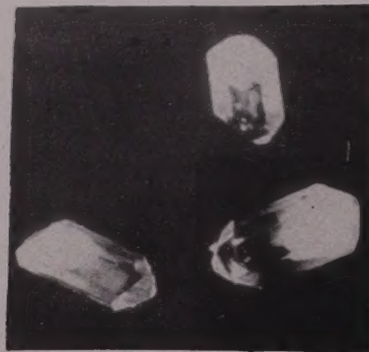


Fig. 15a

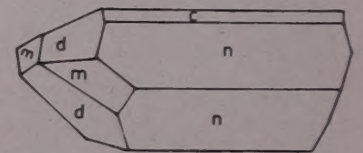


Fig. 15b

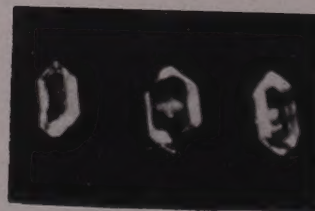


Fig. 16a

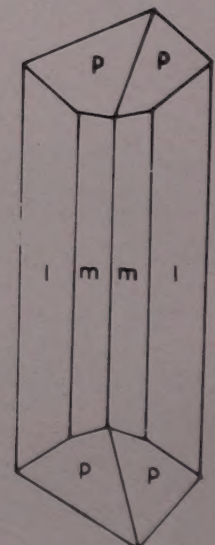


Fig. 16b

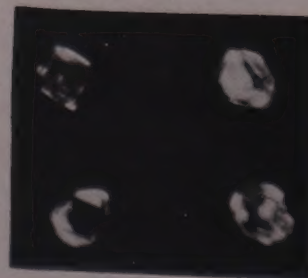


Fig. 17a

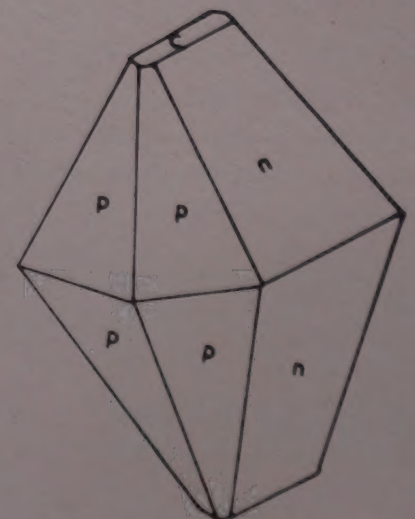


Fig. 17b

Fig. 14-17—Crystals of calcium iodate under different conditions: [(a): Figs 14 & 15, prismatic crystals; Figs 16 & 17, prismatic pyramidal crystal]

### 3.3 Crystals of Calcium Iodate

3.3.1 *Prismatic pyramidal crystals*—Single diffusion experiments, using acetic acid set gels, were found to yield prismatic pyramidal crystals. A couple of such crystals are illustrated in Figs 14(a) and 14(b). Prism  $m\{110\}$  and dome  $d\{102\}$  faces predominate on them. They were found to develop in the later stage of growth, in the region far away from the gel-solution interface. These crystals were small but transparent.

Comparatively large single crystals were obtained in the early stage of growth near the gel-solution interface. A few such crystals are illustrated in Figs



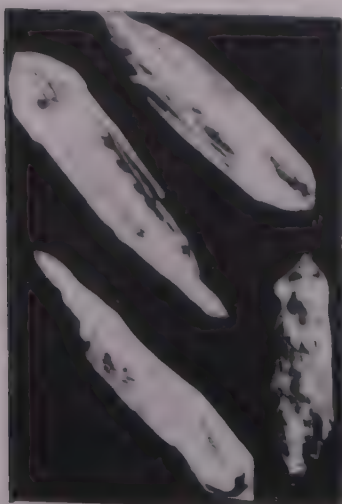


Fig. 18—Hopper elongated crystals of calcium iodate

15(a) and 15(b). These crystals exhibit predominance of dome  $n\{011\}$ ,  $d\{102\}$  and prism  $m\{110\}$  faces on them. They were transparent towards their pyramidal terminations. As against this, their other blunt terminations were highly opaque which may be attributed to gel inclusion. Double diffusion experiments did not yield such crystals.

Another variety of prismatic pyramidal crystals, like those shown in Figs 16(a) and 16(b), were obtained in single diffusion experiments. They were secured in the region far away from the gel-solution interface. Their prism faces  $l\{120\}$  and  $m\{110\}$  were predominant, while pyramidal  $p\{111\}$  faces were very small. As against this, a few elongated crystals were obtained in the region near the gel-solution interface.

In gels set with iodic acid, at low concentration of calcium chloride feed solution, bipyramidal crystals were found to grow. They are shown in Figs 17(a) and 17(b). The dome  $n\{011\}$  and  $p\{111\}$  faces were predominant on them. These crystals were translucent.

Double diffusion experiments also yielded crystals similar to those shown in Figs 16(a) and 16(b), and 17(a) and 17(b).

**3.3.2 Hopper crystals**—Filamentary, hopper crystals were found to grow near the gel-solution interface, when the gel was impregnated with calcium chloride solution, and solution of sodium iodate was used as a feed solution. Figs 18(a) and 18(b) illustrate some of these crystals which resulted from single diffusion experiments.

In double diffusion experiments, hopper crystals were also found to grow in the regions of predominance of iodate ions. By and large, these crystals were opaque which may be attributed to fast growth rates and very high concentration of iodate ions.

#### 4 Discussion

Habit modification depends on phenomena occurring at and near crystal surface during the growth

of crystals. Diffusion of molecules on surfaces of growing crystals is an important parameter in this regard. In very early stages of growth, the relative rates of surface diffusion on basal and prism faces are responsible for determining crystal habit. Once the habit is established, diffusion field around the crystal will orient itself to confine to the crystal geometry and tend to maintain it.

Parameters such as concentration of the reactants, pH of gel, impurities in the solvent, growth temperature, etc. have considerable influence on diffusion rate (or growth rate), which, in turn, governs the crystal habit. In the steady state of concentration gradient, diffusion rate also becomes steady, which favours growth of well developed crystals. However, relatively very slow rate of growth along one direction results in the growth of platy crystals. Preferentially fast growth rate in one particular direction leads to the formation of elongated crystals.

At moderate supersaturations of the reactants, the crystals continue to develop as polyhedra. In such cases, excess material arriving at edges and corners of the crystal is redistributed over the surfaces by surface diffusion. At high supersaturation, surface diffusion becomes unable to cope up with the non-uniform deposition, with the result that the corners and edges begin to sprout to result into dendrites, hopper crystals and other skeleton forms. In the present investigation, dendritic growth of barium iodate, lamellar and elongated growth of strontium iodate and hopper growth of calcium iodate are observed under such conditions.

#### 5 Conclusions

1. Prismatic pyramidal, transparent as well as opaque, barium iodate crystals are obtained. Occasionally, dendritic growth is also observed.

2. Under different growth conditions, platy, prismatic pyramidal, prismatic bi-pyramidal, elongated, lamellar elongated, etc., habits of transparent strontium iodate crystals result.

3. Prismatic bi-pyramidal and prismatic elongated are the habits found in the case of transparent calcium iodate crystals. Opaque crystals result in the event of gel inclusion. Under typical conditions hopper crystals also grow.

#### Acknowledgement

One of us (SGT) sincerely thanks the University Grants Commission, New Delhi for the award of a teacher fellowship under the Faculty Improvement Programme, and the Principal, Navyug Science College, Surat for granting study leave.



## References

- 1 Burton W K, Cabrera N & Frank F C, *Phil Trans Roy Soc A (GB)*, **243** (1951) 299.
- 2 Buckley H E, *Crystal growth* (Wiley, New York) 1951.
- 3 Chernov A A, *Sov Phys (USA)*, **4** (1961) 116.
- 4 Hartman P, *Growth of crystals*, Vol 7, edited by N N Sheftal (Consultants Bureau, New York), 1969.
- 5 Kern R, *Growth of crystals*, edited by N N Sheftal (Consultants Bureau, New York) Vol 8 1969.
- 6 Mullin J W, *Crystallization* (Butterworths, London) 1961.
- 7 Mullin J M, *The inaugural lecture on crystallization: a study in molecular engineering*, University College, London, 1970.
- 8 Elwell D & Scheel H J, *Crystal growth from high temperature solutions*, (Academic Press, London) 1975.
- 9 Gibbs J W, *Phil Mag (GB)*, **37** (1946) 184.
- 10 Joshi M S & Trivedi S G, *Kristal und Technik (Germany)*, **15** (1980) 1131; **16** (1981) 19.



# Growth of High Purity Indium Antimonide Crystals for Infrared Detectors

R K BAGAI\*, G L SETH & W N BORLE

Solid State Physics Laboratory, Delhi 110007

Received 2 November 1982; revised received 3 March 1983

Synthesis, purification and growth of device quality indium antimonide single crystals are described. A horizontal zone melting apparatus with semicircular heaters is used. The crystals are grown in dynamic vacuum. Intrinsic n-type InSb single crystals with mobility of the order  $3 \times 10^5 \text{ cm}^2/\text{V-sec}$  and carrier concentration of the order  $1 \times 10^{14}/\text{cc}$  have been grown.

## 1 Introduction

Indium antimonide has been known for a long time for infrared detectors and Hall sensor applications<sup>1,2</sup>. The possibilities of its use for charge coupled device, Schottky diode, as laser material, etc., have been reported only recently<sup>3-5</sup>. Because of its limited and strategic area of use, details of the technology for the growth of pure and good quality single crystals are not available in the literature to the extent of other semiconductor materials. However, a few successful attempts have been made by various workers for its growth using different approaches<sup>6-11</sup>. Synthesis and growth of high purity InSb crystals suitable for infrared detectors are reported in this paper using horizontal zone melting technique. The synthesis, volatilization, zone refining and the crystal growth have been carried out in the same boat under vacuum, thereby reducing the possibility of contamination of InSb material. Problems concerning the boat and heater designs are discussed and the simple apparatus used for growing crystals is described.

Intrinsic n-type InSb single crystals with carrier concentration of the order of  $1 \times 10^{14}/\text{cc}$  and mobility of the order of  $3 \times 10^5 \text{ cm}^2/\text{V-sec}$  have been obtained.

## 2 Experimental Arrangement

The equipment designed and fabricated at our laboratory is shown in Fig. 1. It consists of a quartz tube sealed at one end and is connected to vacuum pumps at the other end for evacuating it. A quartz boat is placed inside this tube in which synthesis, volatilization and crystal growth are carried out. Semicircular as well as circular type heaters (resistance heated) have been used for forming molten zone. The heaters are mounted on a carriage with wheels. They can be pulled along the guide rails at a desired speed by a motor-driven, slow-speed gear and pulley arrangement. The vertical position of the heaters can be easily adjusted in their stands. All possible care is taken to minimize the vibrations in the system. Zone

refining and crystal growth are done by pulling the heaters from one end to the other.

## 3 Boat Material and Its Preparation

A proper choice for boat material is an important step for the growth of high purity and good quality single crystals of InSb. Quartz has been used most commonly as the boat material. However, earlier reports indicate<sup>12</sup> that molten InSb sticks to quartz and can cause problems. Graphite boats were tried to avoid the wetting problem. But this contaminates InSb as carbon is found to be electrically active impurity in it. Moreover, because of its good thermal conductivity it poses practical problems in forming a sharp and well defined molten zone. At present, use of quartz boat suitably coated with carbon is recommended<sup>10,11</sup>. This makes it non-wettable to molten InSb and does not introduce any chemical impurities. Different approaches have been outlined for applying carbon coating. This is usually done after sandblasting the boat surface.

For the fabrication of boats, the translucent quartz is preferred over the transparent one because of its matty surface. This avoids the need for sandblasting of

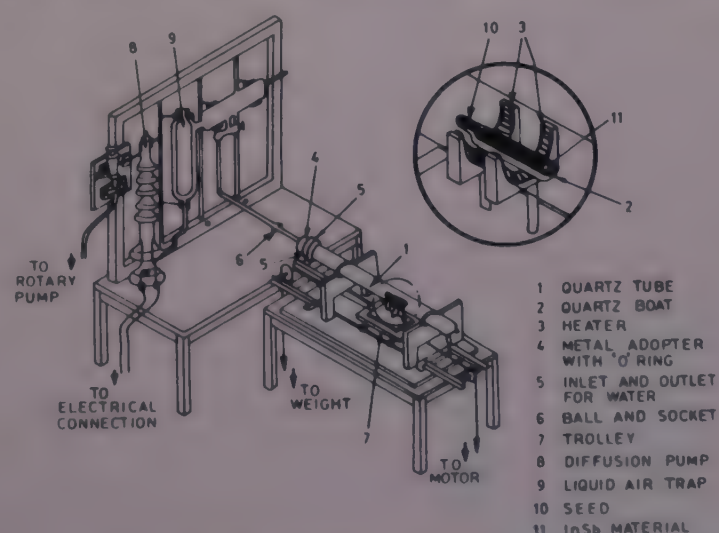


Fig. 1—Experimental arrangement for growing indium antimonide crystals



boat surface. For synthesis, volatilization and zone refining a semicircular boat closed at both ends is used and for crystal growth, a platform is made at one end for supporting a seed (Fig. 1).

Boats are thoroughly cleaned by boiling first in  $\text{HNO}_3$  and then etching with quartz cleaning solution ( $\text{HF}:\text{HNO}_3$  mixture). It is then baked in vacuum at a temperature around  $700^\circ\text{C}$  for 1 hr.

The carbon coating has been carried out by placing the boat in a quartz tube kept vertically inside a resistance-heated furnace for nearly an hour at a temperature of about  $1100^\circ\text{C}$  (constant temperature zone). A few drops of electronic grade acetone are allowed to fall through a funnel. The hydrocarbon compound decomposes at this temperature forming a carbon coating on the entire surface of the boat in an oxygen-deficient atmosphere. This coating is uniform, shining and firmly adhering to the boat. A very important factor observed by us for avoiding the wetting and sticking of InSb to the boat is to ensure that all the time Sb remains in excess of the stoichiometric amount. Even a very minute quantity of In phase creates the sticking problem and deteriorates the quality of the ingot. This is presumably due to the reaction of In with the quartz at the prevalent temperature.

#### 4 Synthesis and Purification

Weighed amounts of In and Sb with an extra amount of Sb added to account for its loss during purification and crystal growth are taken in a quartz boat (about 10 cm long and 20 mm in diameter) kept inside the quartz tube chamber which is evacuated continuously. The material is first synthesized by melting it using resistance heaters. Semicircular heaters of the form shown in Fig. 1 are used. The position and temperature of the heaters are adjusted so that the entire mass remains molten during synthesis and volatilization. The material is kept in a molten state for nearly an hour. During this stage, along with the synthesis, volatilization also takes place.

Volatilization prior to zone refining is an important step towards purifying the material and has got certain advantages. It is well known that Zn and Cd are the main acceptor impurities present in InSb. The distribution coefficient of Zn in InSb is more than 1 and Zn cannot be removed easily by zone refining. Large number of zone passes are essential for its removal. Cd removal is also difficult. Fortunately both Zn and Cd are volatile impurities and hence can be removed by volatilization. During this stage, Sb is also evaporated copiously. This Sb loss has to be taken care of by adding extra Sb in the initial charge. The quantity to be added depends upon the time required for volatilization which in turn depends upon the

concentrations of Zn and Cd in the elemental materials available for the synthesis. This is to be decided empirically for given materials. In our case, both '59' grade and '69' grade materials have been used. The '59' grade In and Sb materials were procured from Nuclear Fuel Complex, Hyderabad (India) and '69' grade material and Al grade Sb were purchased from M/s Cominco, U.S.A. and Johnson Matthey & Co., U.K. respectively.

If the atmosphere of Sb vapour is allowed to stay over the molten InSb during the volatilization, then there is a possibility of back diffusion of the evaporated impurities into the molten charge. To avoid this, semicircular heaters at the bottom side of the boat are found to be helpful. This keeps the upper surface of the quartz chamber tube just above the boat at sufficiently lower temperature to condense the Sb vapours immediately after they are issued from the molten charge.

The volatilization is followed by zone refining *in situ*. A zone is formed at one end by using effectively only one heater. The temperature of the other heater is slightly lowered so that its heat is not sufficient to melt InSb but helps in keeping the rest of the solid ingot clean of any condensed layer of Sb. The zone length is kept in between 1.5 and 2 cm and the pulling speed is around 1.6 cm/hr. This makes the material more pure by removing the remaining impurities to one end. This also gives proper shape to the material for crystal growth. Volatilization is normally done in static vacuum to keep the losses of Sb minimum. However, zone refining and crystal growth are carried out in dynamic vacuum.

#### 5 Crystal Growth

For growing single crystal, the material is transferred to another boat which has got an extra platform to accommodate a seed. A seed having dimensions of  $3\text{ mm} \times 3\text{ mm} \times 30\text{ mm}$  is cut from single crystal of InSb grown along [111] direction. It is suitably prepared by standard methods of lapping and polishing. Seeds having orientation along [111] are used. To confirm that it has [111] orientation and not  $\bar{1}\bar{1}\bar{1}$ , preferential etching technique is used. The etching solution CP-4A develops etch pits only on (111) surface and no pits are delineated on  $\bar{1}\bar{1}\bar{1}$  surface. A molten zone is then formed which is brought in contact with the seed. Sufficient time is allowed and the temperature is maintained sufficiently high so that a small portion of seed is melted and its surface is properly wetted by the zone melt. Zone length is again kept in between 1.5 and 2 cm. The heater is then slowly pulled at a speed of 1.6 cm/hr for single crystal growth.

A significant feature of our technique is the use of semicircular heaters for the crystal growth. There are



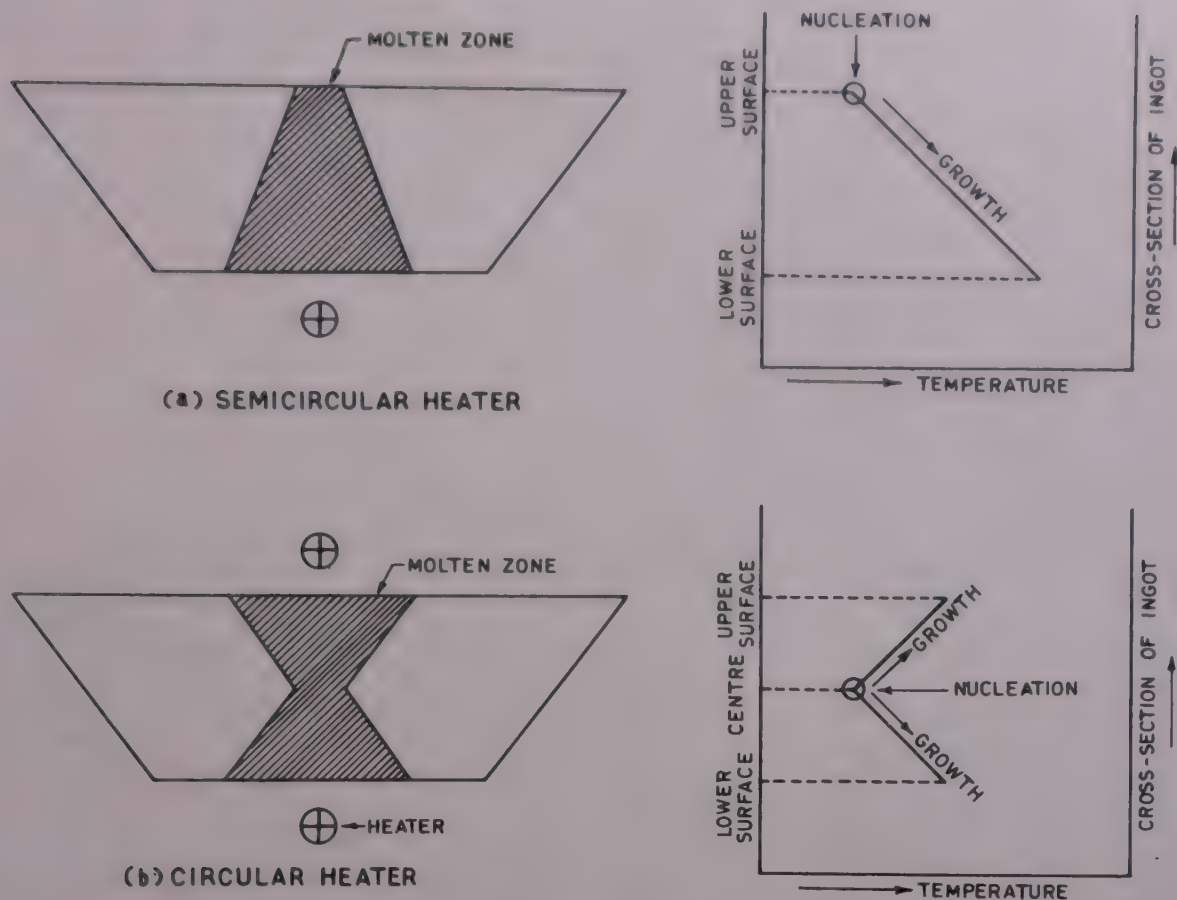


Fig. 2—Nature of solid-liquid interface and temperature profile for:  
(a) semicircular and (b) circular heaters

several advantages of this over the symmetrical circular heater. The nature of the molten zone and the shape of the solid-liquid interfaces are shown schematically for both the cases in Fig. 2 along with the corresponding nature of the temperature profiles. The lowest temperature region, being on the upper surface of the ingot, provides for operational ease and better control in the case of semicircular heater and also surety of molten phase throughout the cross-section. The exposed surface area of the zone also remains minimum. This reduces the losses of Sb and keeps the back diffusion to the minimum. The growth front remains planar making good quality monocrystals possible as the nucleation and growth takes place from top towards bottom and the region of nucleation is not in contact with the boat. On the other hand, the conditions in the case of symmetrical heater are unfavourable and these crystals are always prone to twinning and multicrystalline growth.

Crystals were grown along [111] and [331] directions and it was found that the growth along the [331] direction is more prone to twinning than along [111]. A crystal grown along the [111] direction is shown in Fig. 3.

## 6 Electrical Measurements

The mobility  $\mu$  and carrier concentration  $n$  were measured at liquid air temperature (LAT) using Hall effect measurements<sup>13</sup>. The thickness of the sample

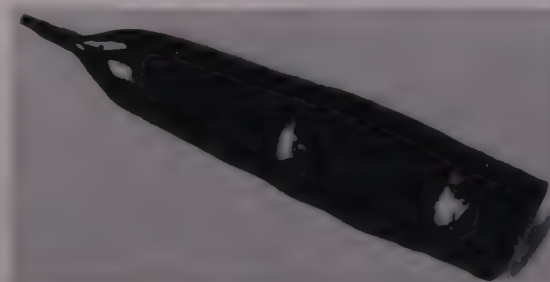


Fig. 3—Photograph of a typical single crystal of InSb grown along the [111] direction [Magnification X1]

wafer was nearly 1 mm. Wafers were cut along the entire length of the crystal at different distances and  $\mu$  and  $n$  values measured. There is not much significant change in the values except near the tail end. At LAT, all the wafers were found to be  $n$ -type.

Experimental data for a few typical cases are presented in Table 1.

## 7 Conclusions

Volatilization is found to be an essential and effective step for the purification of starting material. For further improving the quality of the material, zone refining is necessary. Usually one or two zone passes are sufficient prior to crystal growth. The starting elements indium and antimony need not be of '69' grade purity. Nearly same values of  $\mu$  and  $n$  can be achieved with '59' grade In and A1 grade Sb. However, the melt obtained with '59' grade In and A1 grade Sb sometimes contains scum and hence can disturb the



Table 1—Experimental Data for  $\mu$  and  $n$  for Typical Cases

Sample No.	Weight of initial charge (indium & antimony) (g)	Excess % amount of Sb	Total time of volatilization (min)	Number of zone passes	Loss of Sb (volatilization + zone refining + crystal growth)(%)	Values at LAT of	
						$\mu$ $10^5 \text{ cm}^2/\text{V-sec}$	$n$ $10^{14}/\text{cc}$
1	43.3160	7.8	30	Nil	7.4	$\sim 1.3$	$\sim 10$
2	52.0935	8.1	30	1	8.6	$\sim 2.4$	$\sim 2$
3	54.3100	8.5	85	2	8.5	$\sim 2.7$	$\sim 1.6$
4	38.1550	8.1	60	1	8.6	$\sim 1.5$	$\sim 3$

Samples 1-3 are of '69' grade and sample 4 of '59' grade.

crystal growth. But the melt with '69' grade material is clean.

It has been observed that deficient/surplus amount of Sb within 0.6% of stoichiometric amount does not affect the electrical properties of InSb crystals. This is in confirmation of an earlier report<sup>14</sup>.

#### Acknowledgement

The authors are grateful to the Director, Solid State Physics Laboratory, Delhi for his kind permission to publish this paper. Thanks are also due to Shri K.C. Chhabra and Dr A.V.R. Warriar for their keen interest during the progress of the work.

#### References

- Goodwin D W, *J Sci Instrum (USA)*, **34** (1957) 367.
- King R E J & Bartlett B E, *Philips Tech Rev (Netherlands)*, **22** (1960-61) 217.
- Thom D, Kock T L, Langan J D & Parrish W J, *IEEE Trans Electron Devices (USA)*, **27** (1980) 160.
- Wei C, Wang K L, Taft E A, Swab J M, *et al.*, *IEEE Trans Electron Devices (USA)*, **27** (1980) 170.
- Mandal R P, *Solid State Technol (USA)*, **25** (1982) 94.
- Harmann T C, *J Electrochem Soc (USA)*, **103** (1956) 28.
- Vinogradova K I, Galavanov V V, Nasledov D N & Soloveva L I, *Sov Phys Solid-State (USA)*, **1** (1959) 364.
- Hulme K F & Mullin J B, *Solid-State Electron (GB)*, **5** (1962) 211.
- Parker S G, Wilson O W & Barbee B H, *J Electrochem Soc (USA)*, **112** (1965) 80.
- Ohno I, Waski N I & Yoneyama T, *Jpn J Appl Phys (Japan)*, **18** (1979) 285.
- Murray A R, Baldrey J A, Mullin J B & Jones O, *J Mater Sci (GB)*, **1** (1966) 14.
- Liang S C, *Compound semiconductors*, Vol I, edited by R K Willardson and H L Goering (Reinhold, New York), 1962.
- Van der Pauw L J, *Philips Res Rep (Netherlands)*, **13** (1958) 1.
- Cunnell F A & Saker E W, in *Progress in semiconductors*, Vol 2, edited by Alan F Gibson *et al* (Heywood and Co, London), 1957.



# CNDO/2 and INDO SCF Calculations on Polar Fluorobenzenes

S D SHARMA

Spectroscopy Division, Bhabha Atomic Research Centre, Trombay, Bombay

and

S DORAISWAMY\*

Chemical Physics Group, Tata Institute of Fundamental Research, Bombay 400 005

Received 12 January 1983; revised received 13 June 1983

The modifications in the charge distribution at various sites in the benzene ring caused by the progressive substitution of hydrogens by fluorines at different positions are discussed. To a good approximation, the charge densities in monofluorobenzene can generate the electronic distribution pattern in the higher members of the series. The dipole moments of fluorobenzenes are analyzed in terms of their components and it has been found that the  $\pi$ -component opposes the  $\sigma$ -component in all the cases.

## 1 Introduction

The variety of experimental results accrued from the study of the interaction between the different substituents and the benzene ring have provided a good foundation for understanding many of the qualitative and quantitative aspects of physical organic chemistry<sup>1</sup>. One of the obvious fields wherein the manifestations of intramolecular interaction can be seen is that of molecular physical properties. One such important property is the electric dipole moment, which is closely correlated with the charge distribution in the molecule. Its prediction has been one of the aims of theoretical chemistry. While the attempts to predict the dipole moment by the use of empirically selected bond and group moments have reasonably been successful in saturated compounds, it is far from satisfactory in the case of conjugated compounds. The failure to get satisfactory values has been attributed to the  $\pi$ -electron delocalization<sup>2</sup>. Many theoretical investigations on simple conjugated systems have taken into account only the  $\pi$ -electrons or considered the effects of  $\sigma$ -electrons in a very empirical fashion<sup>3</sup>.

A general self-consistent method in which electron repulsions are explicitly included in the Hamiltonian to take into account all the valence electrons has been most satisfactory in calculating many molecular parameters. In this molecular orbital approach, the dipole moment can be defined by the relation

$$\mu = -e \int \sum_i r_i [\psi(1, 2, 3 \dots n)]^2 \times dv_1 dv_2 dv_3 \dots dv_n + e \sum_A Z_A R_A \dots (1)$$

where  $e$  is the electronic charge,  $r_i$  is the radius vector of the  $i$ th electron,  $Z_A$  and  $R_A$  are the corresponding quantities for the  $A$ th nucleus.

Hence for a given structure or conformation, if the wavefunction and the geometry of the molecule is known, it is possible to calculate the theoretical value of its dipole moment. While this method is certainly superior to the vectorial method, the accuracy of predicted value of the dipole moment is constrained by the degree of approximation of the wavefunction to the true wavefunction of the molecule. Unfortunately it is not only impossible to find a good approximation to the true wavefunction but also the computational time involved is prohibitively large and hence the need to resort to semiempirical methods. In these methods many drastic assumptions have to be made and many interactions (which call for the evaluation of many difficult integrals) have to be neglected in order to reduce the computational time. To enable calculations on large systems to be made in a reasonable time, two or these semiempirical methods have been quite successful. One of these methods proposed by Pople and Segal<sup>4</sup> assumes complete neglect of differential overlap (CNDO) and the other by Pople, Beveridge and Dobosh<sup>5</sup> employs only intermediate neglect of differential overlap (INDO).

Both these methods have been employed in the present work to calculate the charge densities and the dipole moments of all the polar fluorobenzenes. The dipole moments for these molecules have been obtained in the gaseous phase from microwave spectroscopic measurements and hence the comparison with the calculated results is quite illustrative. The all valence electron molecular orbital calculations on some of the fluorobenzenes have earlier been done by Davies<sup>6</sup> and Bloor and Breen<sup>7</sup> by CNDO/2 method. An account<sup>8</sup> on the comparison of experimental and calculated dipole moments of a number of fluorobenzenes by both CNDO/2 and



INDO methods indicates that both these methods systematically overestimate the dipole moments. The object of this paper is to analyze in detail the changes in charge densities at various atomic positions in the benzene ring when fluorines are substituted at different positions.

## 2 Theoretical Calculations

A complete description of all valence electron method and the different levels of approximations are discussed by Pople and Beveridge<sup>9</sup>. Briefly, a molecular orbital  $\psi_i$  can be written as a linear combination of atomic orbitals  $\varphi_\mu$  as

$$\psi_i = \sum_{\mu} C_{\mu i} \varphi_{\mu} \quad \dots (2)$$

where  $C_{\mu i}$  are numerical coefficients which may be real or complex numbers of either sign. Using the criterion of lower calculated total energy, the optimum values of the coefficients  $C_{\mu i}$  lead to a set of self-consistent field molecular orbitals and the Roothan equations

$$\sum (F_{\mu\nu} - \epsilon_i S_{\mu\nu}) C_{\nu i} = 0$$

where  $F_{\mu\nu}$  is the Hartree-Fock Hamiltonian and  $S_{\mu\nu}$  is the overlap integral  $\int \varphi_{\mu}(1) \varphi_{\nu}(1) d\tau_1$ .

In both the CNDO/2 and INDO methods, a number of approximations are made which involve the neglect of many differential and overlap integrals and reduce computational time. Here the elements of Fock matrix  $F_{\mu\nu}$ , when only  $s, p, \dots$  basis set is used, are given by

$$F_{\mu\mu}^{\alpha} = U_{\mu\mu} + \sum_{\lambda} [P_{\lambda\lambda}(\mu\mu/\lambda\lambda) - P_{\lambda\lambda}^{\alpha}(\mu\nu/\mu\nu)] \\ + \sum_{B \neq A} [P_{BB} - Z_B] \gamma_{AB}$$

$$\text{and } F_{\mu\nu} = [2P_{\mu\nu} - P_{\mu\nu}^{\alpha}](\mu\nu/\mu\nu) - P_{\mu\nu}^{\alpha}(\mu\mu/\nu\nu) \mu \quad \text{on atom A} \quad \dots (3)$$

where  $U_{\mu\mu}$  are the monoatomic integrals which depend upon the ionization potentials and electron affinity,  $P_{\lambda\lambda}$  is the density matrix,  $\gamma_{AB}$  is the electron repulsion integral and  $(\mu\lambda/\mu\lambda)$  etc. are the one-centre interaction integrals. Similar expressions hold good for the  $\beta$ -electron. The expressions for the closed-shell matrix elements follow by putting  $P_{\mu\nu}^{\alpha} = P_{\mu\nu}^{\beta} = \frac{1}{2} P_{\mu\nu}$ . The one-centre integrals are given semiempirical values and have been tabulated for the elements up to fluorine<sup>9</sup>. The above expressions become simpler for CNDO/2 approximation where one-centre exchange integrals are also omitted.

In both of the above semiempirical methods the dipole moment in Debyes is deduced from the equation which consists of the sum of two contributions<sup>10</sup>.

$$\mu = 2.5416 \sum_{\lambda} (Z_{\lambda} - P_{\lambda\lambda}) \mathbf{R}_{\lambda} + \mu_{\text{hyb}} \quad \dots (4)$$

where  $Z_{\lambda}$  is the core charge,  $P_{\lambda\lambda} = \sum_{\alpha} (P_{\lambda\lambda}^{\alpha} + P_{\lambda\lambda}^{\beta})$  is the summation of electron populations of all atomic

orbitals centred on a given atom A, the diagonal elements  $P_{\nu\nu}^{\alpha}$  and  $P_{\nu\nu}^{\beta}$  being the  $\alpha$ - and  $\beta$ -electron populations of atomic orbital  $\varphi_{\nu}$ ,  $\mathbf{R}_{\lambda}$  is the position vector of nucleus A. So the first contribution is from the net charge located at the nuclear position. The contribution due to the second term  $\mu_{\text{hyb}}$  is essentially a hybridization term and measures the contribution due to the displacement of charge away from the centre of the nuclear position. This effect is proportional to the off-diagonal density matrix elements  $P_{2sA,2pA}$  between  $2s$  and  $2p$  atomic orbitals centred on atom A. One of the typical components is

$$(\mu_{\text{hyb}})_x = -14.674 \sum_{\lambda}^* \zeta_{\lambda}^{-1} P_{2sA,2p\lambda A} \quad \dots (5)$$

where the summation is restricted to atoms other than hydrogen,  $\zeta_{\lambda}$  is the orbital exponent of valence orbitals centred on atom A. At the CNDO level of calculation the overlap distribution of any two atomic orbitals is neglected in all electron repulsion integrals.

## 3 Experimental Details

Experimental determination of dipole moments in the present work has utilized the microwave spectroscopy method employing Stark effect, which perhaps gives the most reliable values of dipole moments. In this method, the measurement is made in the gaseous phase at low pressures where there is least interaction between neighbouring molecules. Since each molecular species gives its own characteristic spectrum, the measurement is not affected by any impurities. Further, it is possible to determine the values of the dipole moment components along the inertial axes of the molecule. In certain cases even the direction of the dipole moment can be ascertained which is of great advantage, since all the other methods of measurement provide the possibility of determining only the scalar magnitude.

The experimental values of dipole moments of fluorobenzenes reported here are determined by Stark effect measurements of their rotational spectra. In Stark effect, the energy levels of a polar molecule are displaced and sometimes split under the influence of an electric field. For an asymmetric top molecule, to which class these fluorobenzenes belong, the displacement  $\Delta\nu$  of a particular component  $M_j$  of a rotational transition under an applied electric field of strength  $E$  is given by<sup>11</sup>

$$\Delta\nu = \sum_{g=a,b,c} (A_g + B_g M_j^2) \mu_g^2 E^2 \quad \dots (6)$$

where  $A_g$  and  $B_g$  depend upon the rotational constants of the molecule and the transition,  $\mu_g$  is the component of the dipole moment along a particular axis  $g$ . In the Stark-modulated microwave spectrometer, a square wave voltage of low frequency (say 100 kHz) is applied to an electrode which is held parallel to the broad walls



of an absorption cell by means of some insulators<sup>12</sup>. The Stark cell is calibrated (i.e. the spacing between the electrode and broad walls of the waveguide is determined) by using certain molecules like OCS, HCN, or CH<sub>3</sub>F, whose dipole moments have been determined with high precision using parallel plate cells. The displacements of suitable components for various convenient transitions are measured for different field settings. Computer programs are available for calculating  $A_g$  and  $B_g$ . Hence it is a simple matter to calculate the components of the dipole moment from the observed displacements at particular field strengths once the assignment of the transitions has been made. The accuracy of determination of the dipole moments is dependent upon the uniformity of the applied electric field. Except at the edges of the electrode, the field can be assumed to be uniform. The error in the determination of the dipole moment usually does not exceed 1% of the measured value, but in the present case of fluorobenzenes, one standard deviation for some of them is up to 4%. This is because the spectrum for these heavy asymmetric molecules is extremely dense and it becomes difficult to track down the Stark-shifted transitions for fairly large field strengths.

#### 4 Computation

In the theoretical calculations, the geometry of the molecules is one of the input data. The initial calculations on dipole moments of all the fluorobenzenes were performed using the 'standard geometry' given by Pople and Beveridge<sup>9</sup>. These calculations were carried out both by CNDO/2 and INDO methods on DEC 10 computer at the Tata Institute of Fundamental Research, Bombay, employing QCPE 140 program<sup>13</sup>. The results indicated that the overestimation of calculated dipole moments is nearly 10 to 20% compared to the experimental value. This combined with the fact that the ring structure no more remains a regular hexagon, when hydrogen is replaced by fluorine, made us to decide that the dipole moments of fluorobenzenes should also be computed from the geometries which reproduce the moments of inertia obtained from microwave studies, rather than standard geometries. These so called  $r_0$  geometries have been obtained from the microwave studies of as many isotopes as available<sup>14</sup> and the computations repeated in order to obtain an insight into the redistribution of charge at various sites.

#### 5 Charge Densities and Dipole Moments

Considerable work—both theoretical and experimental—on the dipole moments of mono-substituted benzenes has been reported in litera-

ture<sup>3,6,7,15-18</sup>. In view of the fact that more reliable dipole moments of a number of fluorobenzenes, from microwave spectroscopic studies have become available recently, it was thought to be of great interest to see whether molecular orbital calculations predict values in agreement with the experimental results, and, if so, to investigate whether the calculations support or perhaps provide a deeper insight into the concepts of interactions of fluorine substituents with the benzene ring. To the best of our knowledge, the theoretical work on the substituent interaction in substituted benzenes is using *ab initio* molecular orbital theory with STO 3G basis set<sup>19</sup>.

Calculations have been carried out on fluorobenzene, 1,2-difluorobenzene, 1,3-difluorobenzene, 1,2,3-trifluorobenzene, 1,2,4-trifluorobenzene, 1,2,3,4-tetrafluorobenzene, 1,2,3,5-tetrafluorobenzene and 1,2,3,4,5-pentafluorobenzene and the changes taking place in the charge distribution on progressive replacement of hydrogens by fluorines have been discussed in general terms. Table 1 shows the pattern of charge distribution in various fluorobenzenes for  $r_s$  and  $r_0$  geometries by both CNDO/2 and INDO methods. The term  $r_s$  refers to the standard geometry used by Pople<sup>9</sup> while  $r_0$  refers to the structure which reproduces the observed rotational constants of the various fluorobenzenes. The redistribution of electronic charges at various sites with the successive addition of fluorines is quite instructive. The salient features in various fluorobenzenes for the  $r_0$  geometry by the CNDO/2 are discussed below. The overall features for the  $r_s$  geometry are essentially not much different.

**Fluorobenzene (C<sub>6</sub>H<sub>5</sub>F)**—In order to understand the redistribution of electronic charges at various sites in the benzene ring with the gradual addition of fluorines at different positions, it is essential to follow the charge pattern in monofluorobenzene. It is apparent from Table 1, that there is a  $\pi$ -electron transfer from the fluorine to the ring. The *ortho* carbons C<sub>2/6</sub> have cornered nearly twice as much  $\pi$ -charge as the *para* carbon C<sub>4</sub>. The substitution of fluorine has resulted in a noticeable depletion of  $\pi$ -charge density at the substituted carbon site C<sub>1</sub> and *meta* carbons C<sub>3/5</sub>, the former suffering more depletion. As far as electrons are concerned, 80% of the  $\sigma$ -charge attracted by the fluorine has been contributed by the substituted carbon C<sub>1</sub> and a reasonable portion from the hydrogen pair H<sub>2/6</sub> attached to *ortho* carbons C<sub>2/6</sub>. Evidence of long-range inductive effects can be seen in the deposition of a  $\sigma$ -charge at the *para* position, which is about half the size of and opposite in sign to the  $\pi$ -electron density. In terms of the total charge, there is a significant negative charge at the fluorine followed by



Table 1—Electronic Charge Distribution in Fluorine Substituted Benzenes

[Negative  $\Delta q$  values correspond to an increase in electronic charge.]

Atom	CNDO/2				INDO			
	$r_s$		$r_0$		$r_s$		$r_0$	
	$\Delta q^\pi$	$\Delta q^{total}$	$\Delta q^\pi$	$\Delta q^{total}$	$\Delta q^\pi$	$\Delta q^{total}$	$\Delta q^\pi$	$\Delta q^{total}$
Fluorobenzene								
C <sub>1</sub>	+0.0314	+0.2292	+0.0293	+0.2297	+0.0309	+0.2858	+0.0395	+0.2853
C <sub>2,6</sub>	-0.0478	-0.0504	-0.0434	-0.0492	-0.0487	-0.0475	-0.0448	-0.0452
C <sub>3,5</sub>	+0.0215	+0.0261	+0.0220	+0.0286	+0.0201	+0.0494	+0.0208	+0.0516
C <sub>4</sub>	-0.0258	-0.0130	-0.0280	-0.0142	-0.0245	+0.0008	-0.0267	-0.0002
F <sub>1</sub>	+0.0470	-0.2043	+0.0415	-0.2175	+0.0509	-0.2456	+0.0452	-0.2602
H <sub>2,6</sub>	—	+0.0181	—	+0.0227	—	+0.0039	—	+0.0087
H <sub>3,5</sub>	—	+0.0004	—	-0.0017	—	-0.0178	—	-0.0201
H <sub>4</sub>	—	-0.0005	—	+0.0012	—	-0.0171	—	-0.0152
1, 2-Difluorobenzene								
C <sub>1,2</sub>	-0.0139	+0.1817	-0.0124	+0.1843	-0.0153	+0.2259	-0.0134	+0.2286
C <sub>3,6</sub>	-0.0266	-0.0315	-0.0224	-0.0293	-0.0291	-0.0243	-0.0251	-0.0213
C <sub>4,5</sub>	-0.0041	+0.0075	-0.0048	+0.0086	-0.0042	+0.0270	-0.0048	+0.0281
F <sub>1,2</sub>	+0.0446	-0.1880	+0.0396	-0.1955	+0.0486	-0.2276	+0.0433	-0.2361
H <sub>3,6</sub>	—	+0.0249	—	+0.0273	—	+0.0107	—	+0.0132
H <sub>4,5</sub>	—	+0.0055	—	+0.0045	—	-0.0116	—	-0.0126
1,3-Difluorobenzene								
C <sub>1,3</sub>	+0.0521	+0.2511	+0.0498	+0.2517	+0.0503	+0.3131	+0.0488	+0.3121
C <sub>2</sub>	-0.0969	-0.1077	-0.0876	-0.1054	-0.0991	-0.1201	-0.0906	-0.1153
C <sub>4,6</sub>	-0.0739	-0.0693	-0.0714	-0.0687	-0.0736	-0.0702	-0.0716	-0.0685
C <sub>5</sub>	+0.0427	+0.0467	+0.0438	+0.0510	+0.0398	+0.0755	+0.0414	+0.0794
F <sub>1,3</sub>	+0.0490	-0.1986	+0.0435	-0.2125	+0.0530	-0.2399	+0.0474	-0.2552
H <sub>2</sub>	—	+0.0420	—	+0.0517	—	+0.0315	—	+0.0418
H <sub>4,6</sub>	—	+0.0229	—	+0.0293	—	+0.0097	—	+0.0165
H <sub>5</sub>	—	+0.0065	—	+0.0031	—	-0.0122	—	-0.0158
1,2,3-Trifluorobenzene								
C <sub>1,3</sub>	+0.0069	+0.2021	+0.0072	+0.2035	+0.0040	+0.2506	+0.0053	+0.2524
C <sub>2</sub>	-0.0615	+0.1318	-0.0536	+0.1366	-0.0640	+0.1629	-0.0567	+0.1682
C <sub>4,6</sub>	-0.0526	-0.0505	-0.0462	-0.0454	-0.0538	-0.0471	-0.0482	-0.0413
C <sub>5</sub>	+0.0178	+0.0284	+0.0139	+0.0291	+0.0163	+0.0539	+0.0134	+0.0546
F <sub>1,3</sub>	+0.0420	-0.1817	+0.0404	-0.1905	+0.0507	-0.2209	+0.0443	-0.2308
F <sub>2</sub>	+0.0465	-0.1714	+0.0369	-0.1767	+0.0459	-0.2091	+0.0405	-0.2152
H <sub>4,6</sub>	—	+0.0298	—	+0.0321	—	+0.0166	—	+0.0190
H <sub>5</sub>	—	+0.0118	—	+0.0115	—	-0.0059	—	-0.0063
1,2,4-Trifluorobenzene								
C <sub>1</sub>	-0.0396	+0.1640	-0.0389	+0.1656	-0.0396	+0.2048	-0.0389	+0.2064
C <sub>2</sub>	+0.0072	+0.2032	+0.0076	+0.2048	+0.0044	+0.2526	+0.0055	+0.2540
C <sub>3</sub>	-0.0758	-0.0890	-0.0651	-0.0823	-0.0794	-0.0972	-0.0695	-0.0883
C <sub>4</sub>	+0.0284	+0.2352	+0.0237	+0.2347	+0.0279	+0.2942	+0.0240	+0.2925
C <sub>5</sub>	-0.0522	-0.0483	-0.0485	-0.0459	-0.0533	-0.0436	-0.0499	-0.0404
C <sub>6</sub>	-0.0049	-0.0107	-0.0011	-0.0068	-0.0089	-0.0020	-0.0038	-0.0067
F <sub>1</sub>	+0.0429	+0.1851	+0.0380	+0.1917	+0.0468	+0.2242	+0.0416	+0.2317
F <sub>2</sub>	+0.0466	-0.1822	+0.0416	-0.1897	+0.0508	-0.2218	+0.0455	-0.2302
H <sub>4</sub>	—	+0.0487	—	+0.0545	—	+0.0382	—	+0.0443
F <sub>3</sub>	+0.0474	-0.1956	+0.0417	-0.2075	+0.0514	-0.2362	+0.0455	-0.2479
H <sub>5</sub>	—	+0.0289	—	+0.0325	—	+0.0151	—	+0.0189
H <sub>6</sub>	—	+0.0309	—	+0.0318	—	+0.0163	—	+0.0172
1,2,3,4-Tetrafluorobenzene								
C <sub>1,4</sub>	-0.0180	+0.1850	-0.0164	+0.1871	-0.0195	+0.2302	-0.0175	+0.2325
C <sub>2,1</sub>	-0.0402	+0.1522	-0.0349	+0.1568	-0.0442	+0.1876	-0.0387	+0.1929
C <sub>3,5</sub>	-0.0306	-0.0295	-0.0263	-0.0243	-0.0333	-0.0205	-0.0289	-0.0143
F <sub>1,4</sub>	+0.0449	-0.1789	+0.0391	-0.1842	+0.0490	-0.2173	+0.0429	-0.2259
F <sub>2,3</sub>	+0.0440	-0.1650	+0.0384	-0.1702	+0.0481	-0.2022	+0.0421	-0.2083
H <sub>1,4</sub>	—	+0.0360	—	+0.0368	—	+0.0222	—	+0.0231

(Contd)



Table 1—Electronic Charge Distribution in Fluorine Substituted Benzenes—Contd.

[Negative  $\Delta q$  values correspond to an increase in electronic charge.]

Atom	CNDO/2				INDO			
	$r_s$		$r_0$		$r_s$		$r_0$	
	$\Delta q^\pi$	$\Delta q^{\text{total}}$	$\Delta q^\pi$	$\Delta q^{\text{total}}$	$\Delta q^\pi$	$\Delta q^{\text{total}}$	$\Delta q^\pi$	$\Delta q^{\text{total}}$
1,2,3,5-Tetrafluorobenzene								
C <sub>1/3</sub>	+0.0278	+0.2237	+0.0255	+0.2239	+0.0235	+0.2775	+0.0231	+0.2783
C <sub>2</sub>	-0.0877	+0.1135	-0.0799	+0.1192	-0.0890	+0.1410	-0.0805	+0.1469
C <sub>4/6</sub>	-0.1021	-0.1077	-0.0887	-0.0980	-0.1045	-0.1199	-0.0929	-0.1080
C <sub>5</sub>	+0.0496	+0.2576	+0.0418	+0.2563	+0.0478	+0.3222	+0.0420	+0.3206
F <sub>1/3</sub>	+0.0485	-0.1757	+0.0421	-0.1843	+0.0528	-0.2149	+0.0461	-0.2245
F <sub>2</sub>	+0.0403	-0.1686	+0.0354	-0.1731	+0.0441	-0.2058	+0.0389	-0.2111
H <sub>4/6</sub>	—	+0.0533	—	+0.0572	—	+0.0437	—	+0.0478
F <sub>5</sub>	+0.0493	-0.1896	+0.0430	-0.2000	+0.0535	-0.2303	+0.0471	-0.2419
1,2,3,4,5-pentafluorobenzene								
C <sub>1/3</sub>	+0.0038	+0.2075	+0.0027	+0.2086	+0.0009	+0.2584	+0.0012	+0.2603
C <sub>2/4</sub>	-0.0661	+0.1342	-0.0574	+0.1405	-0.0689	+0.1661	-0.0608	+0.1727
C <sub>3</sub>	-0.0191	+0.1723	-0.0177	+0.1748	-0.0248	+0.2119	-0.0220	+0.2155
C <sub>6</sub>	-0.0804	-0.0886	-0.0681	-0.0779	-0.0843	-0.0963	-0.0733	-0.0846
F <sub>1/3</sub>	+0.0469	-0.1726	+0.0407	-0.1795	+0.0512	-0.2113	+0.0447	-0.2192
F <sub>2/4</sub>	+0.0422	-0.1620	+0.0371	-0.1669	+0.0463	-0.1989	+0.0408	-0.2047
F <sub>5</sub>	+0.0459	-0.1583	+0.0398	-0.1634	+0.0502	-0.1951	+0.0438	-0.2010
H <sub>6</sub>	—	+0.0604	—	+0.0612	—	+0.0508	—	+0.0519

the *ortho* carbons C<sub>2/6</sub>. Consequent to this redistribution the HC bonds get polarized.

**1, 2-Difluorobenzene**—When one more fluorine is added to monofluorobenzene in the *ortho* position, it can be seen that the major accumulation (nearly 55%) of  $\pi$ -electronic charge donated by the fluorines is in the carbons C<sub>3/6</sub> adjacent to the substituted carbons. The other pairs of carbons C<sub>1/2</sub> and C<sub>4/5</sub> partition the remaining  $\pi$ -charge in the approximate ratio of 3:1. The analysis of  $\sigma$ -charge indicates that the main supplier to the fluorines are the substituted carbons while adjacent hydrogen pair H<sub>3/6</sub> provide about 10% thereby causing polarization of those HC-bonds. In fact, the whole charge distribution in the molecule can reasonably be reproduced if both the fluorines are thought of as forcing their individual charge pattern in the ring independently, analogous to monofluorobenzene. Because of the competition between the fluorines, it may be noticed that there is a net reduction of  $\sigma$ -charge by about 10% at the fluorine sites compared to monofluorobenzene.

**1, 3-Difluorobenzene**—Since the *ortho* and *para* positions are the principal beneficiaries of  $\pi$ -charge in monofluorobenzene, it is easy to understand that in this molecule the concentration of  $\pi$ -charges is at C<sub>2</sub> and C<sub>4/6</sub> sites, if the charge effects due to the two fluorines are considered to act independently. There is also a considerable drainage of  $\pi$ -charge at C<sub>1</sub>, C<sub>3</sub> and C<sub>5</sub> positions. The bonded carbons are the principal

source of  $\sigma$ -charges for the fluorines, which are supplemented further by the hydrogens attached to C<sub>2</sub>, C<sub>4</sub> and C<sub>6</sub> atoms. There seems to be a cooperativeness between fluorines as is evident by the slight increase in  $\sigma$ -charge in both of them compared to monofluorobenzene.

**1, 2, 3-Trifluorobenzene**—The charge distribution in this molecule can be understood on the basis of the discussion of the 1, 2- and 1, 3-difluorobenzenes. The  $\pi$ -electrons donated by the fluorines get deposited essentially at C<sub>2</sub>, C<sub>4/6</sub> atoms, with C<sub>2</sub> taking the major share by virtue of its being *ortho* to the other two carbons carrying fluorines. As in the above cases, the  $\sigma$ -charge drainage by fluorines is from the carbons to which they are appended, the two peripheral fluorines having about 10% more charge than the central fluorine. The crowding of fluorines seems to increase the competition as can be seen in the reduction of  $\sigma$ -charge density on them compared to any of the above three molecules.

**1, 2, 4-Trifluorobenzene**—In this molecule, the partitioning of  $\pi$ -charge from the fluorines has taken place among the C<sub>3</sub>, C<sub>5</sub> and C<sub>1</sub> carbons in decreasing order of magnitude and there is a reduction of  $\pi$ -charge at the C<sub>4</sub> site. Again the principal donors of  $\sigma$ -charge to fluorines have been C<sub>4</sub>, C<sub>2</sub> and C<sub>1</sub> atoms in decreasing order, together with a reasonable contribution from H<sub>3/5</sub> and H<sub>6</sub> atoms. Consequently all the HC-bonds are polarized. The slight decongestion obviously



seems to benefit the fluorines, as evidenced by a slight increase in their  $\sigma$ -charge densities compared to 1, 2, 3-trifluorobenzene.

**1, 2, 3, 4-Tetrafluorobenzene**—In this molecule, all the carbon atoms of the ring have benefited by the  $\pi$ -donation of fluorines in the order  $C_{2/3} > C_{5/6} > C_{1/4}$ . Likewise the  $\sigma$ -charge grabbed by fluorines have essentially originated from the carbon atoms to which they are appended together with a small contribution from the two hydrogens, thereby causing the polarization of the HC-bonds. The increase in the crowding of fluorines has a direct effect in the progressive decrease of  $\sigma$ -charge densities, with the outer pair of fluorines  $F_{1/4}$  having nearly 10% more charge than the inner pair  $F_{2/3}$ .

**1, 2, 3, 5-Tetrafluorobenzene**—The carbon atoms  $C_2$  and  $C_{4/6}$  form the  $\pi$ -sinks in this molecule, draining charge mainly from fluorines. A depletion of  $\pi$ -charge can also be noticed in the carbon atoms  $C_{1/3}$  and  $C_5$ , the last carbon atom suffering a loss equivalent to that of a fluorine. The  $\sigma$ -charge on the fluorines is mainly derived from the carbons to which they are attached and also to a small extent from the two hydrogens. The fluorines in the crowded region have less charge density than the fluorine  $F_5$ .

**1, 2, 3, 4, 5-Pentafluorobenzene**—The  $\pi$ -contribution to the ring by the fluorines and the concentration of  $\sigma$ -charge densities on them are in the order  $F_{1/5} > F_{2/4} > F_3$ . The effect of maximum density of the fluorines has resulted in an all round reduction of  $\sigma$ -charge densities compared to all other molecules.

Since all the substituents have been fluorines, it would be interesting to compare the amount of total  $\sigma$ -charge withdrawn from and total  $\pi$ -charge donated to the ring as more and more fluorines replace hydrogens. It may be seen that the  $\sigma$ -charge withdrawal and  $\pi$ -charge donation generally increase with the number of fluorines. Whenever fluorines are juxtaposed, the charge exchange has a reasonable linear relationship to the number of fluorines. However, when the substitution does not take place successively but in an alternate position, the  $\sigma$ -charge withdrawal or  $\pi$  donation is marginally more than for the corresponding juxtaposed fluorine molecule—for example, compare the pairs 1, 2 and 1, 3 difluorobenzenes, 1, 2, 3 and 1, 2, 4 trifluorobenzenes and 1, 2, 3, 4 and 1, 2, 3, 5 tetrafluorobenzenes (see Table 2). It is equally instructive to analyze the charge barter between the fluorines and the ring in terms of the average share of the  $\sigma$ - and  $\pi$ -charges of the fluorines as a function of the number and position of fluorines. It may be seen that the average withdrawal of  $\sigma$ -charge per fluorine decreases as more and more fluorines are juxtaposed in the order  $C_6H_5F > 1, 2-C_6H_4F_2 > 1, 2, 3-C_6H_3F_3 > 1, 2, 3, 4-C_6H_2F_4 > C_6F_5H$ . But in molecules 1, 3-difluorobenzene, 1, 2, 4-trifluorobenzene and 1, 2, 3, 5-tetrafluorobenzene, in which there is an intervening hydrogen between fluorines, the average  $\sigma$ -charge withdrawal becomes more compared to their juxtaposed counterpart. In the case of the average  $\pi$ -charge donation per fluorine, the trend is more or less the same as in the case of  $\sigma$ -charge.

Table 2—Comparison of the  $\sigma$  and  $\pi$ -Charge Exchange between the Fluorines and the Benzenes Ring in Polar Fluorobenzenes

Molecule	<i>Ab initio</i> <sup>a</sup>				CNDO/2 <sup>b</sup>				INDO <sup>c</sup>			
	Total†		Per fluorine*		Total†		Per fluorine*		Total†		Per fluorine*	
	$q_\sigma$	$q_\pi$	$q_\sigma$	$q_\pi$	$q_\sigma$	$q_\pi$	$q_\sigma$	$q_\pi$	$q_\sigma$	$q_\pi$	$q_\sigma$	$q_\pi$
Monofluorobenzene	-0.215	+0.080	-0.215	+0.080	-0.259	+0.042	-0.259	+0.042	-0.305	+0.045	-0.305	+0.045
1,2-Difluorobenzene	-0.408	+0.150	-0.204	+0.075	-0.470	+0.079	-0.235	+0.039	-0.559	+0.089	-0.279	+0.044
1,3-Difluorobenzene	-0.420	+0.160	-0.210	+0.080	-0.512	+0.087	-0.256	+0.043	-0.605	+0.095	-0.302	+0.047
1,2,3-Trifluorobenzene	-0.598	+0.226	-0.199	+0.075	-0.675	+0.118	-0.225	+0.039	-0.806	+0.129	-0.269	+0.043
1,2,4-Trifluorobenzene	-0.612	+0.229	-0.204	+0.076	-0.710	+0.121	-0.237	+0.040	-0.842	+0.133	-0.281	+0.044
1,2,3,4-Tetrafluorobenzene	-0.618	+0.298	-0.155	+0.075	-0.863	+0.155	-0.216	+0.039	-1.038	+0.172	-0.259	+0.043
1,2,3,5-Tetrafluorobenzene	-0.627	+0.309	-0.157	+0.077	-0.866	+0.163	-0.216	+0.041	-1.080	+0.178	-0.270	+0.044
Pentafluorobenzene	-0.960	+0.373	-0.192	+0.075	-1.052	+0.195	-0.210	+0.039	-1.264	+0.215	-0.253	+0.043

<sup>a</sup> Ref. 19, p. 52. The signs of charges are reverse of that of Ref. 19.

<sup>b</sup> & This work calculated for  $r_0$  geometries.

† The total  $\sigma$ - and  $\pi$ -charges donated to the ring by the fluorines.

\* The average  $\sigma$ - and  $\pi$ -charges per fluorine donated to the ring by the fluorines.



At this point it may also be relevant to compare these results with that of the recent *ab initio* calculation (Table 2). While caution has to be exercised in attaching significance to the absolute values of the charges obtained by various theoretical methods, relative changes are generally more meaningful and useful. As far as the  $\sigma$ -charge withdrawal is concerned, after an initial perceptible increase up to 1, 2, 3-trifluorobenzene, there is some sort of levelling off which steeply rises for pentafluorobenzene. However, the behaviour in  $\pi$ -charge distribution is analogous to the semiempirical calculations outlined earlier. Consequently a dissimilar behaviour is exhibited for the average  $\sigma$ -charge withdrawal per fluorine while the behaviour of average  $\pi$ -charge donation per fluorine has a close similarity to the earlier results. It is rather surprising as to why in the *ab initio* calculations the average  $\sigma$ -charge withdrawal per fluorine falls off by nearly 25% electron units for 1, 2, 3, 4- and 1, 2, 3, 5-tetrafluorobenzenes from its average value of 0.20 electron units while the average  $\pi$ -charge donation remains at about 0.08 electron units for all molecules.

The charge distributions listed in Table 1 for various fluorobenzenes have been calculated individually through the computer program. It is of interest to note that the charge distribution in monofluorobenzene alone is enough to reproduce the charge distribution of the higher members of the series to a good approximation. In other words, the resultant charge densities of the required fluorobenzene are obtainable by just superposition of monofluorobenzene as many times as there are number of fluorines in the molecule after suitable rotations so that the net picture of superposition would result in the desired molecule<sup>8</sup>.

Table 1 also lists the charge densities calculated by the INDO approximation for both the  $r_s$  and  $r_0$  structures. The overall picture of the charge distribution follows the above description except that there is about 20% excess charge density at the fluorine sites.

Although the exact interpretation of the dipole moments of these fluorobenzenes is difficult, the changes taking place in the various components of the dipole moment can still be discussed when hydrogen is replaced by fluorine which is capable of conjugation with the benzene ring. Table 3 lists the total as well as the  $\mu_\sigma$ ,  $\mu_\pi$  and  $\mu_{sp}$  components of the dipole moment by both CNDO/2 and INDO methods for the  $r_0$  geometry obtained from Eqs (4) and (5).  $\mu_\pi$  has been calculated from the expression

$$\mu_\pi(z) = 4.8 \sum_i e_i z_i \quad \text{Debyes} \quad \dots (7)$$

where  $e_i$  is the excess or deficit charge given in the bond order matrix on the  $P_z$  orbital of the  $i$ th atom. The  $\mu_\sigma$  is then obtained by subtracting  $\mu_\pi$  algebraically from Eq. (4).

It may be noted that the major contribution to the total dipole moment in all the fluorobenzenes is from the dipole moment given rise to by  $\sigma$ -electrons alone. Next in order of importance is the  $\pi$  dipole moment, which is essentially caused by two inseparable contributions, namely the  $\pi$ -induction effect and true mesomeric effect. This moment opposes the  $\sigma$ -moment in all the fluorobenzenes. The  $\pi$ -moment contribution reduces from about 27% of its total value in fluorobenzene to about 22.5% of its total value in pentafluorobenzene. The third component, i.e. the dipole moment due to  $\mu_{hyb}$ , is between 13 to 22% and is in the same direction as  $\mu_\sigma$ . Its contribution appears slightly increased when fluorines are crowded together. The major difference for INDO compared to CNDO/2 calculations appears to be an overall reduction of about 20% in the estimated value of  $\mu_{hyb}$ . As reported elsewhere<sup>8</sup> both the CNDO/2 and INDO calculations overestimate the dipole moments of all the fluorobenzenes, which becomes more pronounced for the members of series carrying more and more fluorines as can be seen from Table 3.

Table 3—Total Dipole Moment (in D) and Their Components for Fluorobenzenes by CNDO/2 and INDO methods  
[The observed dipole moments are taken from microwave spectroscopic data<sup>20-25</sup>.]

Molecule	Obs.	CNDO/2				INDO			
		$\mu_\sigma \uparrow$	$\mu_\pi \downarrow$	$\mu_{sp} \uparrow$	$\mu_{total}$	$\mu_\sigma \uparrow$	$\mu_\pi \downarrow$	$\mu_{sp} \uparrow$	$\mu_{total}$
Fluorobenzene	1.66 ± 0.03	1.9603	-0.4808	0.2967	1.7762	2.1706	-0.5202	0.2280	1.8784
1,2-Difluorobenzene	2.59 ± 0.02	3.3494	-0.813	0.5705	3.1069	3.7137	-0.8855	0.4500	3.2782
1,3-Difluorobenzene	1.51 ± 0.02	1.9714	-0.4858	0.3076	1.7932	2.1803	-0.5272	0.2338	1.8869
1,2,3-Trifluorobenzene	—	3.9176	-0.9252	0.6231	3.6154	4.3467	-1.0076	0.4884	3.8225
1,2,4-Trifluorobenzene	1.39 ± 0.03	1.9428	-0.4769	0.3241	1.7900	2.1497	-0.5174	0.2536	1.8859
1,2,3,4-Tetrafluorobenzene	2.42 ± 0.05	3.3304	-0.7777	0.5601	3.1128	3.6896	-0.8484	0.4398	3.2810
1,2,3,5-Tetrafluorobenzene	1.46 ± 0.06	1.9573	-0.4275	0.3249	1.8547	2.1801	-0.4664	0.2651	1.9788
1,2,3,4,5-Pentafluorobenzene	1.44 ± 0.03	1.8906	-0.4102	0.3446	1.825	2.1052	-0.4520	0.2781	1.9314



## 6 Conclusion

We have made a detailed analysis of the charge redistribution in fluorobenzenes with the help of CNDO/INDO methods and have concluded (as is well accepted) that fluorine is a  $\sigma$ -acceptor and a  $\pi$ -donor. When more fluorines are added, this fact considerably changes the pattern of charge distribution throughout the molecule. There appears to be an additivity in the charge distribution patterns of computed substitution effect. We have also shown that there is a systematic overestimation of dipole moment with the progressive addition of fluorines and concluded that perhaps it is the conjugative effects which have not been estimated properly. Our hope that the use of  $r_0$  geometries may give better values for the dipole moments of fluorobenzenes with CNDO/2 or INDO calculations has been belied. But the trend towards systematic overestimation of dipole moments on progressive fluorination may perhaps be useful in parametrizing some of the integrals to reproduce the dipole moments of conjugated fluoro-compounds with better accuracy.

## References

- 1 Ingold C K, *Structure and mechanism in organic chemistry* (Cornell University Press, Ithaca, New York) 1953.
- 2 LeFevre R J W, *Dipole moments* (Methuen, London), 3rd Edn, 1953, Chap IV.
- 3 (a) Streitwiser A, *Molecular orbital theory for organic chemists* (John Wiley, New York), 1961.  
(b) Salem L, *The molecular orbital theory of conjugated systems* (W A Benjamin, New York), 1966.
- 4 Pople J A & Segal G A, *J Chem Phys (USA)*, **44** (1966) 3289.
- 5 Pople J A, Beveridge D L & Dobosh P A, *J Chem Phys (USA)*, **47** (1967) 2026.
- 6 Davies D W, *Mol Phys (GB)*, **13** (1967) 456.
- 7 Bloor J E & Breen D L, *J Phys Chem (USA)*, **72** (1968) 716.
- 8 Doraiswamy S & Sharma S D, *J Mol Struct Theochem (Netherlands)*, **94** (1983) 63.
- 9 Pople J A & Beveridge D L, *Approximate molecular orbital theory* (McGraw Hill, New York), 1970, 111.
- 10 Ref 9, p 87.
- 11 Golden S & Wilson Jr E B, *J Chem Phys (USA)*, **16** (1948) 669.
- 12 Townes C H & Schawlow A L, *Microwave spectroscopy* (McGraw Hill, New York), 1955, 419.
- 13 Dobosh P A, *Quantum Chemical Programme Exchange*, 142 (Indiana University, Bloomington, Indiana, USA).
- 14 Doraiswamy S & Sharma S D, *J Mol Struct (Netherlands)*, 1983, in press.
- 15 Minkin V I, Osipov O A & Zhdanov Y A, *Dipole moments in organic chemistry* (Plenum Press, New York), 1970.
- 16 Brown R D & Collier B A W, *Theor Chim Acta (Germany)*, **1** (1967) 259.
- 17 Hehre W J, Radom L & Pople J A, *J Am Chem Soc (USA)*, **94** (1972) 1496.
- 18 Brownlee R T & Taft R W, *J Am Chem Soc (USA)*, **92** (1970) 7007.
- 19 Press A & Radom L, *Progress in physical organic chemistry*, Vol 13, edited by R W Taft (John Wiley, New York), 1981, 1-63.
- 20 De Kowalewski D G, Kokeritz P & Selen H J, *J Chem Phys (USA)*, **31** (1959) 1438.
- 21 Nygaard L, Hansen E R, Hansen R L, et al, *Spectrochim Acta Vol A (GB)*, **22** (1967) 2813.
- 22 Doraiswamy S & Sharma S D, *J Phys Soc Jpn (Japan)*, **44** (1978) 598.
- 23 Hartmann T & Botskor I, *J Mol Struct (Netherlands)*, **22** (1974) 337.
- 24 Sharma S D & Doraiswamy S, *Can J Phys (Canada)*, **55** (1977) 1211.
- 25 Doraiswamy S & Sharma S D, *Pramana (India)*, **2** (1974) 219.



# Dielectric Studies & Structure of -NCO Group in some Isocyanates

P BRAHMA & S K ROY\*

Optics Department, Indian Association for the Cultivation of Science, Jadavpur, Calcutta 32

Received 13 August 1982

Dielectric absorption measurements in *meta* and *para* tolylisocyanates and *para* chlorophenylisocyanate in benzene solution have been made at 30, 45 and 60°C at different microwave frequencies. The results have been analyzed for molecular and group relaxation processes. Their relative weight factors and heats of activation have been determined. From consideration of the experimentally obtained dipole moments and the weight factors, it is concluded that the group -NCO in each case is inclined to the phenyl ring and the amount of inclination has been determined in each case.

## 1 Introduction

From studies of dielectric relaxation in the case of phenylisocyanate, phenylisothiocyanate and sulphinylaniline<sup>1</sup> it was observed that molecular and intramolecular relaxation mechanisms are present in each case and the groups -NCS and -NCO were concluded to be inclined and not collinear with  $C_1$ - $C_4$  axis of the ring. The amount of spatial inclination of the group in each molecule was determined. The object of the present work is to extend similar studies in the case of *meta* and *para* tolylisocyanates and *p*-chlorophenylisocyanate with a view to finding out the spatial arrangement of -NCO group in each case. The results of such an investigation have been presented and discussed in this paper.

## 2 Experimental Details

Samples of *meta* and *para* tolylisocyanates and *para* chlorophenylisocyanate of 99% purity were obtained from M/s Ega Chemie, Germany. These were dried and distilled under reduced pressure before use. Analar benzene as solvent was also dried and distilled before use.

The apparatus and method of procedure to determine the complex dielectric permittivity at different microwave frequencies were described earlier<sup>2</sup>. Static dielectric constants  $\epsilon_0$  were determined at 3 MHz; the viscosity  $\eta$  and density  $d$  were determined by Ostwald viscometer and a pycnometer respectively. The temperatures were maintained constant within  $\pm 1^\circ\text{C}$  by means of a thermostat.

## 3 Results

The experimental values of  $\epsilon'$  and  $\epsilon''$  at different microwave frequencies and at different temperatures are presented in Table 1. The values of static dielectric constant  $\epsilon_0$ , density  $d$ , viscosity  $\eta$ , refractive index  $n_D$ , high frequency dielectric constant  $\epsilon_\infty$ , distribution parameter  $\alpha$  are presented in Table 2.

Complex plane plots (Fig. 1) of the dielectric permittivity  $\epsilon'$  and dielectric loss  $\epsilon''$  showed appreciable distribution at all temperatures. So the dielectric data were analyzed in terms of two relaxation processes using Bergmann's equation<sup>3</sup> which were solved by the method of least square described earlier<sup>4</sup>. The calculations for the determinations of  $\tau_1$ ,  $\tau_2$  and  $C_1$  were carried out on the computer B6700. The calculated values of  $\epsilon'$  and  $\epsilon''$  are included in Table 1 for comparison with the observed values. The heats of activation for molecular orientation ( $\Delta H_{\tau_1}$ ) and for intramolecular rotation ( $\Delta H_{\tau_2}$ ) were determined from the slope of the plots of  $\log T\tau_1$  vs  $1/T$  and  $\log T\tau_2$  vs  $1/T$  respectively. The heat of activation for viscous flow was determined from the plots of  $\log \eta$  versus  $1/T$ . The dipole moment was calculated from the relation<sup>5</sup>

$$\mu^2 = \frac{9kT(\epsilon_0 - \epsilon_\infty)(2\epsilon_0 + \epsilon_\infty)}{4\pi N \epsilon_0(\epsilon_\infty + 2)^2}$$

The values of  $\tau_1$ ,  $\tau_2$ ,  $C_1$ ,  $\Delta H_{\tau_1}$ ,  $\Delta H_{\tau_2}$ ,  $\Delta H_\eta$  and dipole moment  $\mu$  are given in Table 2.

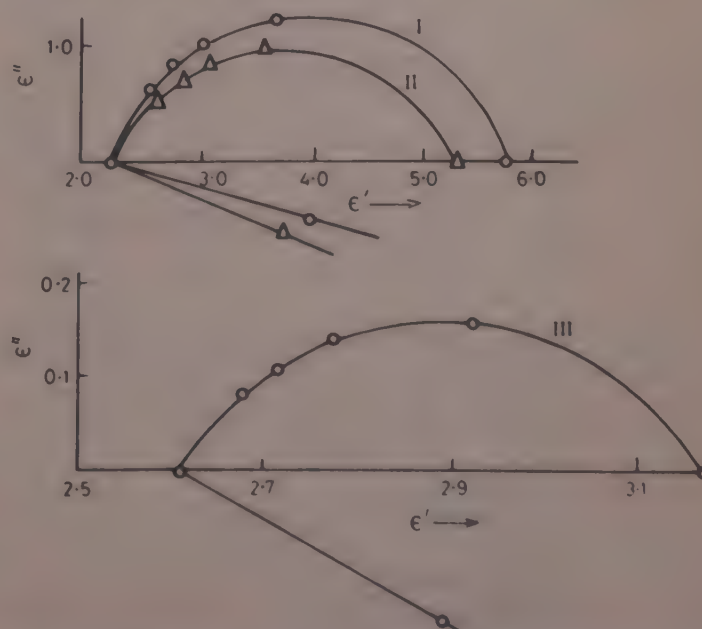


Fig. 1—Cole-Cole arc plots for I, *p*-tolylisocyanate; II, *m*-tolylisocyanate; and III, 4-chlorophenylisocyanate



Table 1—Observed & Calculated Values of  $\epsilon'$  &  $\epsilon''$  and  $\epsilon_0$  in Benzene Solution (Conc. in mole fraction)  
(0.390) *para*-Tolylisocyanate

$T, ^\circ\text{C}$	$f=8.6\text{ GHz}$				$f=18.08\text{ GHz}$				3 MHz
	$\epsilon'_{\text{obs}}$	$\epsilon'_{\text{calc}}$	$\epsilon''_{\text{obs}}$	$\epsilon''_{\text{calc}}$	$\epsilon'_{\text{obs}}$	$\epsilon'_{\text{calc}}$	$\epsilon''_{\text{obs}}$	$\epsilon''_{\text{calc}}$	
30	3.27	3.16	1.10	1.18	2.72	2.75	0.80	0.76	5.70
45	3.34	3.26	1.14	1.20	2.77	2.79	0.83	0.79	5.50
60	3.38	3.35	1.18	1.22	2.82	2.81	0.86	0.82	5.30

(0.392) *meta*-Tolylisocyanate

30	3.25	3.15	1.05	1.08	2.72	2.75	0.71	0.72	5.20
45	3.32	3.27	1.10	1.12	2.80	2.79	0.76	0.77	5.00
60	3.38	3.38	1.14	1.12	2.85	2.81	0.78	0.80	4.82

(Pure liquid) 4-Chlorophenylisocyanate

30	2.88	2.81	0.16	0.18	2.74	2.74	0.12	0.12	3.18
45	2.87	2.80	0.16	0.18	2.73	2.73	0.13	0.13	3.12
60	2.86	2.80	0.17	0.18	2.72	2.71	0.13	0.13	3.10

$f=24.09\text{ GHz}$

$f=36.01\text{ GHz}$

(0.390) *para*-Tolylisocyanate

30	2.63	2.66	0.60	0.64	2.50	2.55	0.48	0.51	5.70
45	2.67	2.69	0.63	0.66	2.52	2.57	0.51	0.53	5.50
60	2.70	2.70	0.66	0.68	2.55	2.59	0.52	0.54	5.30

(0.392) *meta*-Tolylisocyanate

30	2.62	2.65	0.62	0.61	2.50	2.54	0.46	0.48	5.20
45	2.67	2.68	0.66	0.65	2.52	2.56	0.48	0.50	5.00
60	2.71	2.70	0.66	0.66	2.52	2.55	0.50	0.51	4.82

(Pure liquid) 4-Chlorophenylisocyanate

30	2.70	2.73	0.10	0.11	2.66	2.70	0.09	0.10	3.18
45	2.69	2.71	0.10	0.10	2.66	2.69	0.08	0.09	3.12
60	2.68	2.70	0.11	0.11	2.64	2.68	0.08	0.08	3.10

Table 2—Values of Density, Viscosity,  $n_D^2$ ,  $\epsilon_x$ ,  $\tau_1$ ,  $\tau_2$ ,  $\alpha$ ,  $C_1$ ,  $H_\eta$ ,  $H_{\tau_1}$ ,  $H_{\tau_2}$  &  $\mu$

$T$ C	$d$ g/cc	$\eta$ cP	$n_D^2$	$\epsilon_x$	$\tau_1 \times 10^{12}$ s	$\tau_2 \times 10^{12}$ s	$\alpha$	$C_1$	$\mu_D$
<i>p</i> -Tolylisocyanate									
30	0.956	0.515	2.28	2.30	41.8	4.0	0.15	0.90	2.50
45	0.942	0.430	2.26	2.29	36.0	3.50	0.14	0.88	2.52
60	0.927	0.380	2.25	2.30	30.2	2.92	0.13	0.87	2.54
<i>m</i> -Tolylisocyanate									
30	0.962	0.72	2.28	2.29	36.0	3.86	0.18	0.87	2.30
45	0.948	0.60	2.26	2.31	28.8	3.41	0.17	0.88	2.33
60	0.934	0.51	2.24	2.32	23.2	3.00	0.17	0.90	2.35
4-Chlorophenylisocyanate									
30	1.263	1.48	2.43	2.61	40.0	2.67	0.34	0.78	0.80
45	1.245	1.10	2.40	2.61	34.0	1.90	0.29	0.81	0.82
60	1.230	0.73	2.38	2.61	27.0	1.40	0.24	0.85	0.85
Compound					$H_\eta$ (kcal mol <sup>-1</sup> )	$H_{\tau_1}$ (kcal mol <sup>-1</sup> )	$H_{\tau_2}$ (kcal mol <sup>-1</sup> )	$\mu_D$ (liter- mole <sup>-1</sup> )	
<i>p</i> -Tolylisocyanate					2.05	1.77	1.58		
<i>m</i> -Tolylisocyanate					2.10	1.73	1.11		
4-Chlorophenylisocyanate					3.62	2.00	3.2	0.84	



#### 4 Discussion

It can be seen from Table 2 that the dielectric data in the three isocyanates have been analyzed in terms of two relaxation processes, the larger relaxation times  $\tau_1$  being due to molecular reorientation and the shorter one  $\tau_2$  due to the rotation of  $-NCO$  group. This indicates that the  $-NCO$  group is not collinear with the  $C_1-C_4$  axis of the ring but inclined to it. Such inclination of the groups  $-NCS$  and  $-NCO$  in phenylisothiocyanate and phenylisocyanate was reported earlier<sup>1</sup>.

The molecular relaxation time  $\tau_1$  in *p*-chlorophenylisocyanate and *p*-tolylisocyanate is about the same ( $\approx 41$  psec) and is a little larger than the molecular relaxation time of *m*-tolylisocyanate ( $\approx 36$  psec). These are consistent with the size of the molecules. The  $-NCO$  group relaxation time in *p*-chlorophenylisocyanate (2.7 psec) is shorter than that in *meta* and *para* tolylisocyanates ( $\approx 4$  psec). This may be due to the smaller inclination ( $\approx 12^\circ$ ) of  $-NCO$  group in *p*-chlorophenylisocyanate than that in tolylisocyanates ( $\approx 27^\circ$ ) as shown in Section 4.3.

##### 4.1 Weight Factors

The value of the weight factor  $C_1$  for molecular orientation lying in the range (0.8-0.9) in the three cases shows that the molecular reorientation is the major relaxation process in each of them.

##### 4.2 Heats of Activation

The heat of activation ( $\Delta H\tau_1$ ) for molecular relaxation is larger than that due to group rotation ( $\Delta H\tau_2$ ) in each molecule. The heat of activation due to viscous flow  $\Delta H_\eta$  is larger than the values of  $\Delta H_\tau$  in each case as is generally observed in polar liquids.

##### 4.3 Dipole Moment and Spatial Arrangement of the $-NCO$ Group

The experimental values of the dipole moments  $\mu$  of the three molecules as given in Table 2, agree with the literature values<sup>6</sup>.

*p*-Chlorophenylisocyanate—If the group  $-NCO$  were double bonded ( $-N=C=O$ ) and collinear with the  $C_1-C_4$  axis of the phenyl ring, then taking the bond moments<sup>7</sup>,  $\mu_{C\equiv N}=3.1D$ ,  $\mu_{C-Cl}=1.5D$ ,  $\mu_{C-N}=0.45D$ ,  $\mu_{C=N}=1.4D$ ,  $\mu_{C=O}=2.4D$  and  $\mu_{C-O}=0.7D$ , the dipole moment of the molecule would be  $\mu = -1.58 + 0.45 - 1.4 + 2.4 = -0.13D$  which differs from the experimental value of dipole moment  $0.8D$  of the molecule. Again, if the group is  $N^+ \equiv C-O^-$  due to mesomeric structure and is still collinear with  $C_1-C_4$  axis of the phenyl ring, the dipole moment of the molecule will be  $\mu = -1.58 + 0.45 - 3.1 + 0.7 = -3.53D$

which also differs from the experimental value of  $0.8D$ . So it is concluded that the  $-NCO$  group is inclined to the  $C_1-C_4$  axis by an angle  $\Phi$ . This is also supported by the fact that the shorter relaxation time

$\tau_2$  was assigned to the rotation of  $-NCO$  group about the  $C-N$  bond attached to the ring.

Now if the group  $-NCO$  is inclined to the  $C-N$  bond, the resultant moment  $\mu$  of the molecule will make an angle  $\theta$  with the  $C-N$  axis as shown in Fig. 2a.

Then the moment component responsible for molecular orientation is  $\mu \cos \theta$  and for group rotation is  $\mu \sin \theta$ . If  $C_1$  and  $C_2$  are weight factors for molecular orientation and group rotation respectively then  $C_1 = (\mu \cos \theta)^2 / \mu^2 = 0.78$ , then  $\theta = 28^\circ$ , and the moment component responsible for molecular orientation is  $\mu \cos \theta = 0.8 \times \cos 28^\circ = 0.706$

The moment component responsible for group rotation is  $\mu \sin \theta$  or  $C_2 = (\mu \sin \theta)^2 / \mu^2 = (\mu_1 \sin \Phi)^2 / \mu^2 = 0.22$ , or  $\mu_1 \sin \Phi = \sqrt{0.22} \times 0.8 = 0.375$  where  $\mu_1$  is the moment of  $-NCO$  group and  $\Phi$  is an angle made by it with the  $C-N$  axis. The moment component responsible for group rotation is  $\mu_1 \sin \Phi = 0.375$  and  $\mu \cos \theta = \mu_1 \cos \Phi + 0.45 - 1.58$  or  $\mu_1 \cos \Phi = \mu \cos \theta + 1.13 = 1.836D$  from which  $\mu_1 = 1.87$  and  $\Phi = 11.5^\circ$ . Assuming the group as  $N^+ \equiv C-O^-$ ,  $\mu_{N\equiv C-O} = -3.1 + 0.7 = -2.4D$ .

The value of  $\mu_1 = 2.4D$  fits better with the calculated value of  $\mu_1 = 1.87D$  from the weight factors  $C_1$  and  $C_2$  obtained from relaxation studies. It is, therefore, concluded that the structure of the group is  $N^+ \equiv C-O^-$  which is also suggested by Hibben<sup>8</sup> and it makes an angle of about  $12^\circ$  with the  $C-N$  axis attached to the phenyl ring. It should be noted here that the structure of the  $-NCO$  group in phenylisocyanate as reported earlier<sup>1</sup> is  $-N\equiv C-O$  and it makes an angle  $\Phi = 36^\circ$  with the  $C-N$  bond attached to the phenyl ring.

*p* and *m*-Tolylisocyanate—Similar calculations in *p*-tolylisocyanate (Fig. 2b) show that the moment of the molecule makes an angle  $\theta = 18.4^\circ$  with the  $C-N$  axis and  $N^+ \equiv C-O^-$  group makes an angle of  $\Phi = 27^\circ$  with the  $C-N$  bond and in the case of *m*-tolylisocyanate (Fig. 2c), the moment of the molecule makes an angle  $\theta = 21^\circ$  with the  $C-N$  bond and the group makes an angle  $\Phi = 29^\circ$  with the  $C_1-C_4$  axis.

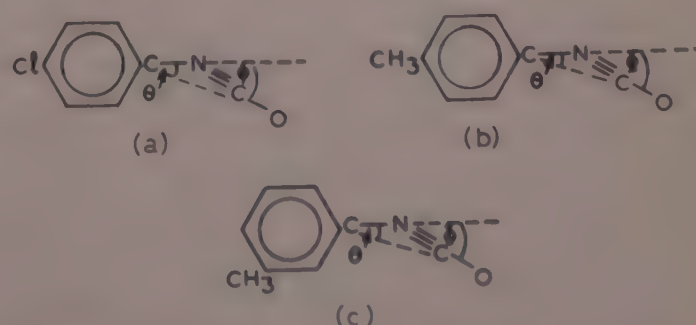


Fig. 2—Configurational diagrams of: (a), *p*-chlorophenylisocyanate; (b), *p*-tolylisocyanate; and (c), *m*-tolylisocyanate



### Acknowledgement

The authors express their sincere thanks to Dr S B Roy for guidance and Prof. G S Kastha for his interest.

### References

- 1 Roy S K, *Adv Mol Relaxation & Interaction Process, (Netherlands)*, **12** (1978) 229.
- 2 Roy S K, Sengupta K, Ghatak A & Das A, *J Chem Phys(USA)* **65** (1976) 3595.
- 3 Bergmann K, Roberti D & Smyth P, *J Phys Chem(USA)*, **64**(1960) 665.
- 4 Roy S K, Sengupta K & Roy S B, *Bull Chem Soc Jpn (Japan)*, **49** (1976) 663.
- 5 Tay S P & Crossley, *Can J Chem (Canada)*, **50** (1972) 2031.
- 6 *Landolt-Born Tables*, Vol I, Part 3, 478.
- 7 Smith J W, *Electric dipole moments (Butterworths, London)* 1955, 94.
- 8 Hibben J H, *The Raman effect and its application* (Reinhold, New York) 1939, 1282.



## Attenuation and Scattering Coefficients of $\gamma$ -Rays through Compressed Powdered Clay

A H EL-KAMEL, M H SAIED & A L EL-ATTAR\*†

Physics Department, Faculty of Science, Assiut University, Kena, Egypt

Received 8 April 1982; accepted 25 July 1983

The attenuation and scattering coefficients of  $\gamma$ -rays in compressed powdered clay were studied. The effects of particle size (diam.,  $d$ ) and radiation energy ( $I$ ) were investigated. Flux distribution inside the absorber was studied by the method of isoflux curves. The results showed an inverse proportionality between  $d$  and  $\mu$  and between  $\partial\mu/\partial I$  and  $I$ . The side scattering coefficient ( $\Phi$ ) is directly proportional to both  $d$  and  $I$ .

### 1 Introduction

One of the main goals in radiation protection is the attenuation of the emitted radiation to safety levels. Therefore, the propagation of radiation fluxes in shielding materials is an essential requirement for design purposes. Selection of materials is obviously an important part of shield technology and needs careful study. In general, the protective materials used for biological (and radiation) shielding (in the case of  $\gamma$ -radiation) must have the following properties<sup>1,2</sup>:

(i) Maximum possible density to ensure maximum attenuation of  $\gamma$ -radiation; (ii) constant density and homogeneity of the shielding material; (iii) satisfactory resistance of the material to radiation effects; (iv) low residual radioactivity, i.e. minimum amount of long-living radioisotopes which might accumulate in the shield.

The purpose of this paper is to describe the series of experiments undertaken by us to investigate some transmission properties of  $\gamma$ -radiation through compressed powdered clay. The most important quantity characterizing the penetration and diffusion of  $\gamma$ -radiation in extended matter is the attenuation coefficient ( $\mu$ ) which depends on the photon energy ( $E$ ) and atomic number ( $Z$ ) of the medium<sup>3</sup>. So we are interested first to evaluate  $\mu$  as well as the flux distribution and the side scattering of radiation for different  $\gamma$ -energies and different grain diameters of the material under investigation, i.e. compressed powdered clay.

### 2 Experimental Details

Compressed samples of powdered clay in the form of circular discs of 5 cm in diameter were used in this

investigation. The powder was prepared by grinding the clay, sieving it through a standard set of sieves: 0.315, 0.250, 0.160, 0.125, 0.091 and 0.070 mm, then pressed under 10 ton/cm<sup>2</sup> to thicknesses in the range 0.98-1.78 cm. Three sources of  $\gamma$ -radiation have been used: <sup>60</sup>Co, <sup>137</sup>Cs and <sup>133</sup>Ba. Every source is housed in a lead container. Radiation is confined to a narrow beam by a lead collimator having a small hole.

Besides the measurements to determine  $\mu$ , two other measurements were performed:

(i) Side scattering—In this case the detector is fixed at a certain distance from the sample's edge (2 cm) and directed perpendicular to the direction of the incident beam. Different measurements are taken along the extension of the sample.

(ii) Flux distribution inside the sample—Assuming that the incident radiation is propagated along the  $Z$ -axis, the disc-shaped samples are kept in the ( $X$ - $Y$ ) plane. Measurements are taken in planes parallel to the sample plane at  $X=0, \pm 1, 2$  cm to study the flux distribution inside the absorber.

### 3 Results and Discussion

#### 3.1 Evaluation of the Linear Attenuation Coefficient $\mu$

Although the term absorption coefficient had been used in literature in reference to the total photon interaction cross-section in macroscopic units, we follow here the recent nomenclature of the ICRU report<sup>4</sup> using the term 'attenuation coefficient' for absorption coefficient. Since the linear attenuation coefficient is more convenient for engineering applications<sup>3</sup>, it is used by us rather than the mass attenuation coefficient.

Linear attenuation coefficients ( $\mu$ s) of the compressed powdered clay for the 3 radioactive sources <sup>60</sup>Co, <sup>137</sup>Cs and <sup>133</sup>Ba were calculated from the relation:

$$I(I) = I_0 \exp(-\mu I) \quad \dots (1)$$

\*† Physics Department, Faculty of Science, Assiut University, Assiut, Egypt



Fig. 1 shows the relation between grain diameter ( $d$ ) and  $\mu$  and the half-value layer ( $t_{1/2}$ )—as evaluated from the experimental attenuation curves. Fig. 1 shows that as  $d$  increases,  $\mu$  decreases linearly for any source of radiation. It has been shown that  $\mu$  varies with  $d$  according to the following empirical formula:

$$\mu = ad + K \text{ for } 0.07 \leq d \leq 0.315 \quad \dots (2)$$

where  $a$  is the slope-rate of change of  $\mu$  with  $d$ . The values of  $a$  for the 3 sources  $^{60}\text{Co}$ ,  $^{137}\text{Cs}$  and  $^{133}\text{Ba}$  are 0.125, 0.182 and 0.299 respectively. From the values given above it is easy to see that as the energy of radiation source decreases,  $a$  increases. Fig. 1 also shows that the calculated value of  $t_{1/2}$  is directly proportional to  $d$ . It is also evident from Fig. 1 that  $\mu$  is inversely proportional to the incident energy which is in accordance with the results of another experiment<sup>5</sup> where the source of radiation was soft X-rays (15 to 25 keV).

The changes of  $\mu$  with  $d$  can be explained by the following two considerations:

(i) Every photon is eliminated individually from the beam in a single event. As the powder gets more fine, the boundary surfaces increase giving rise to multiple scattering. This increases the path of the incident radiation inside the absorber; hence the probability that a photon to be removed from the beam increases<sup>5</sup>.

(ii) The compressed powdered absorber can be considered as a material containing small random voids between the grains. The effect of voids on radiation penetration through the absorber was

studied by Smith<sup>6</sup>. He derived an effective attenuation coefficient  $\mu_e$  as:

$$\mu_e = \frac{(1-v)}{1 + 0.55(s/\mu)v^2} \quad \dots (3)$$

where  $\mu$  is the actual attenuation coefficient;  $v$  the fraction of the volume occupied by voids; and  $s$  the average distance between voids.

From Eq. (3) it is clear that  $\mu_e$  decreases as  $v$  increases. As the grain size gets smaller, the volume of voids decreases leading to an increase in the attenuation coefficient.

### 3.2 Flux Distribution and Isoflux Curves

To calculate the thickness and geometrical shape of shields required to attenuate  $\gamma$ -radiation to a certain value, the isoflux curves are constructed from radiation flux distribution. Fig. 2 represents such curves for 2 values of  $d$  [ $0.250 < d \leq 0.315$ ;  $0.160 < d \leq 0.250$ ] in case of  $^{137}\text{Cs}$  source. Fig. 2 shows that for a point and monodirectional source of  $\gamma$ -rays, the shield thickness required to attenuate the flux to a certain value along the beam direction is larger than the thickness needed along the perpendicular direction for the flux range of interest. Similar results were already reported for thermal neutron flux distribution<sup>7</sup>.

The distance from the point of incidence to the point of detection at  $X = \pm 1, 2$  cm can be calculated from the simple relation:  $t_{\text{calc}} = (X^2 + t^2)^{1/2}$  where  $t$  is the thickness of the sample. The intensity ( $I$ ) of transmitted radiation corresponding to these distances along beam direction is estimated from the attenuation curves. Comparing the calculated values ( $I_{\text{calc}}$ ) with the actual measured values ( $I_{\text{exptl}}$ ) at  $X = \pm 1, 2$  cm, it was found that  $I_{\text{exptl}}$  is always less than  $I_{\text{calc}}$ . The ratio ( $I_{\text{exptl}}/I_{\text{calc}}$ ) versus ( $t_{\text{calc}}$ ) is plotted in Fig. 3. It was found that this ratio neither depends on the grain diameter nor on the thickness of the absorber. It depends only on the position of the detector relative to the direction of incidence and on the energy of radiation.

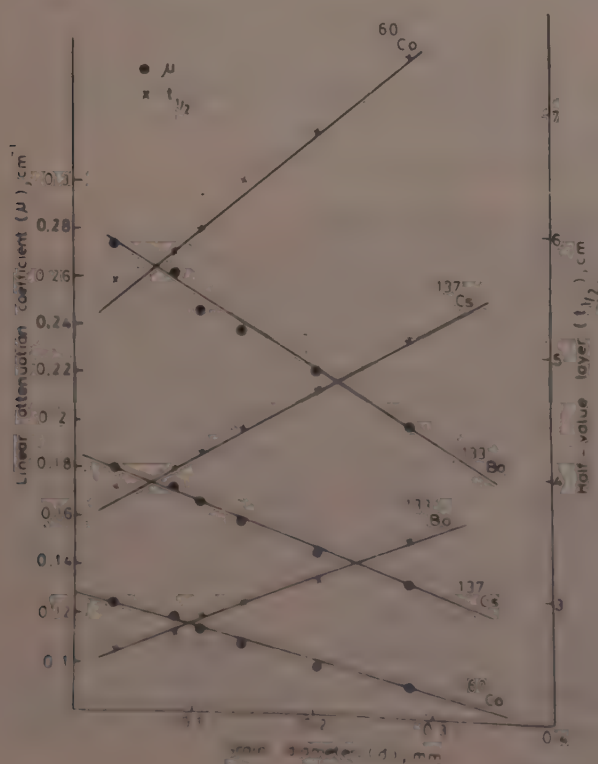


Fig. 1 The variations of half-value layer and linear attenuation coefficient with the grain diameter

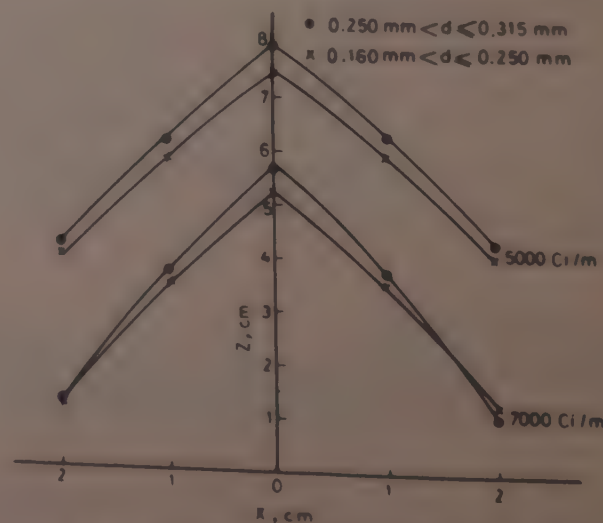


Fig. 2 Isoflux curves of  $^{137}\text{Cs}$   $\gamma$ -rays in clay



### 3.3 Side Scattering

Side scattering is defined as the ratio between the scattered radiation around the absorber ( $I_s$ ) and the

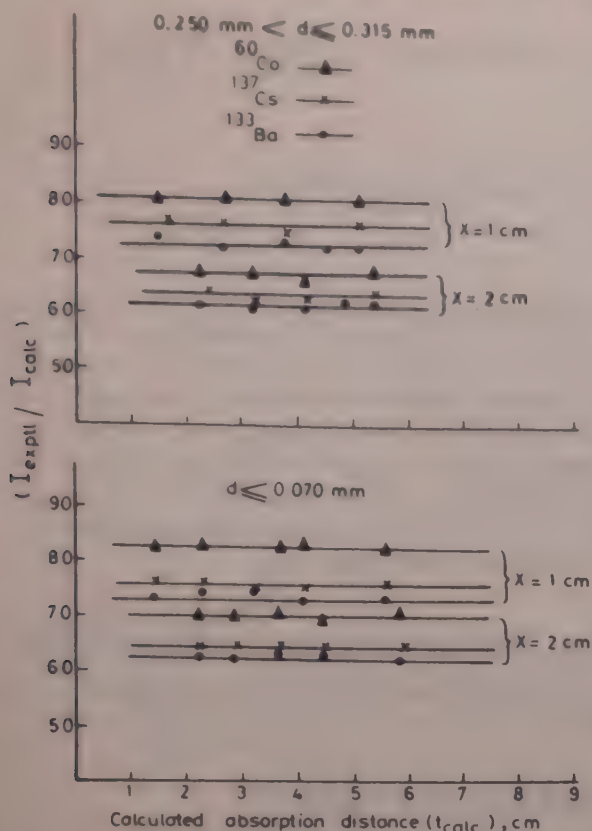


Fig. 3—Relation between  $I_{\text{exptl}}/I_{\text{calc}}$  and the calculated absorption distance  $t_{\text{calc}}$  for  $X = 1$  and  $2$  cm

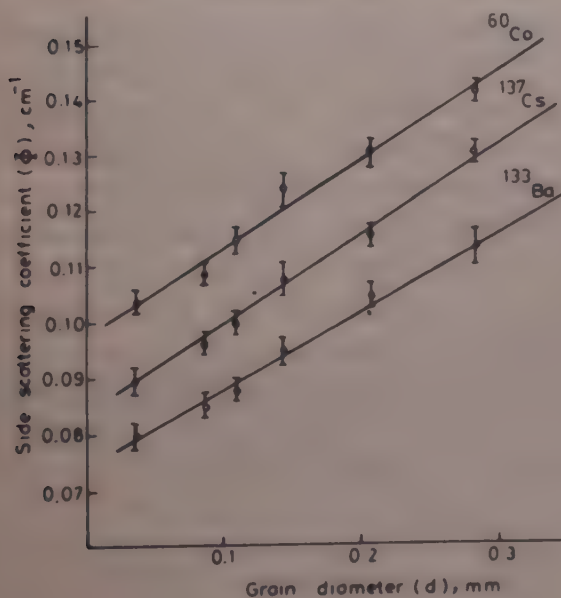


Fig. 4—Relation between the side scattering coefficient and the grain diameter

initial intensity  $I_0$ . The side scattering ( $I_s/I_0$ ) was found to decrease exponentially as the thickness of the sample is increased—a result which led to the following proposed formula:

$$I_s = I_0 \exp(-\Phi t) \quad \dots (4)$$

where  $\Phi$  represents the side scattering coefficient.

This constant was found to depend on the energy of the incident radiation as well as on the grain diameter ( $d$ ) of the powder. Eq. (4) was verified experimentally and the values of  $\Phi$  were calculated. Fig. 4 shows the relation between  $d$  and  $\Phi$ . From Fig. 4 it is clear that  $\Phi$  increases linearly with  $d$ . For the same grain diameter, and in the energy range of interest,  $\Phi$  increases with the energy of radiation.

### 4 Conclusions

(1) The attenuation coefficient ( $\mu$ ) is inversely proportional to the grain diameter and the rate of change of  $\mu$  is inversely proportional to radiation energy.

(2) The side scattering coefficient is directly proportional to both the grain diameter and the radiation energy.

(3) Isoflux curves showed that the flux distribution inside the sample is similar to that of the thermal neutron flux distribution.

### References

- 1 Komarovskii A N, *Design of nuclear plants*, translated from Russian (Atomizdat, Moscow) 1965; USAEC Report AEC-tr-6722, 1965.
- 2 Schaeffer N M, *Reactor shielding for nuclear engineers* (US Atomic Energy Commission, Washington) 1978, 455.
- 3 Hubbell J H, *Photon cross-sections, attenuation coefficients, and energy absorption coefficients from 10 keV to 100 GeV*; NSRDS (National Standard Reference Data System)-NBS (National Bureau of Standards)-29 US 1969.
- 4 Hubbel J H, McMaster W H, Kerr Del Grande N, *et al.*, *International tables for X-ray crystallography* (Kynoch Press, Birmingham, England) 1974, Vol 4, p 47.
- 5 Gameel Y H, Belal A & El-Kamel A H, *Indian J Pure & Appl Phys*, 16 (1978) 62.
- 6 Smith N M (Jr), *The absorption and scattering of radiation in random aggregates of pebbles*; USAEC Report CNL-21 (Oak Ridge National Laboratory, Tennessee, USA), March 1948.
- 7 Ibrahim M A, *The effect of cylindrical air filled duct on the distribution of thermal neutron flux in Egyptian concrete* M Sc, thesis, Mansoura University, Egypt, 1979.



# Multiple Scattering of Gamma Rays in Semi-infinite Water

J SWARUP\*, L H PESHORI & K K UPPAL

Health Physics Division, Bhabha Atomic Research Centre, Bombay 400085

Received 3 September 1982

Transmitted spectra of  $^{241}\text{Am}$ ,  $^{57}\text{Co}$ ,  $^{203}\text{Hg}$ ,  $^{137}\text{Cs}$  and  $^{60}\text{Co}$  point sources, through several mean-free-path thicknesses of water are measured with a thin (38 mm  $\times$  1 mm) CsI (TI) detector. Due to multiple scattering of gamma rays in water, the spectra show a peak at 60 keV energy which is independent of primary source energy. The source appears to be surrounded by a halo of these low energy photons. The intensity of the halo at a distance  $d$  from the source can be expressed by the equation,  $I = I_0 e^{-\mu d}$ , where  $I_0$  is the intensity of multiple-scattered photons at the location of the point source, and  $\mu$  is the multiple-scatter coefficient for this medium. The values of  $I_0$  and  $\mu$  decrease with increase in primary energy. The peak energy, 60 keV, is a characteristic energy and is transmitted preferentially through this medium. The ratio of values of  $I_0$  for the source immersed under and that for the source floating on water surface is approximately 2. This shows that the shape of the halo is spherical or hemispherical, depending on whether the source is immersed under or floating on the water surface.

## 1 Introduction

The energy of a gamma photon while passing through matter is dissipated mainly by three well-known processes, namely, Compton scattering, photo-electric effect and pair production. The electrons and positrons of these processes slow down by emitting bremsstrahlung radiation, or by ionization of the atoms of the medium which emit low energy photons. The positron annihilates itself into a pair of 511 keV photons. These secondary photons are further scattered or photo-absorbed to give still lower energy photons. These processes continue in the medium successively till the energy of the primary photon is divided into several photons of thermal energy.

The Compton cross-section of a medium decreases slowly with increase in energy, while the photo-electric cross-section which is comparatively higher initially, decreases sharply with increase in energy. At an energy where these two cross-sections balance each other, there is a pile-up of photons in the medium due to multiple-scattering, giving rise to a peak in the low energy part of the spectrum. This peak has been called as multiple-scatter peak<sup>1</sup> of the medium.

The multiple-scatter peak has been reported by many workers<sup>2-9</sup> who have studied gamma ray scattering in different infinite and semi-infinite media. Brust<sup>2</sup> has shown that for media of different atomic numbers, the multiple-scatter peak is at different energies in the soft part of the spectrum, and Minato<sup>3</sup> has concluded that, as a first approximation, its energy varies directly with the atomic number of the medium. Bishop<sup>10</sup> has reviewed the energy and angle spectra of gamma-ray penetrations through different media.

The purpose of this paper is to present a study of the transmitted pulse-height spectra for different thicknesses of water, measured for different primary

energies. The independence of multiple-scatter energy from the primary energy is demonstrated, confirming theoretical and experimental studies.

## 2 Experimental Arrangement

The experimental system consists of a drum of polythene (90 cm high, 58 cm diameter and 0.6 cm wall thickness) kept on a 2.5 cm thick plywood stand with a circular hole of 7.5 cm diameter in its centre, below which a detector assembly is placed at a distance of 6.1 cm (Fig. 1). The detector assembly consists of a CsI (TI) crystal (38 mm diameter and 1 mm height) optically coupled to a RCA-4523 photomultiplier, which is housed in a 3-mm thick brass casing having a mylar window of 2 mg/cm<sup>2</sup> thickness and 38 mm diameter. The axis of the drum is placed co-linear with the extended axis of the crystal. The detector assembly is surrounded by Pb-bricks to shield it from the scattered radiation from ground and nearby objects of a large counting room. The spectra are recorded with a Nuclear Data 512-Channel analyzer.

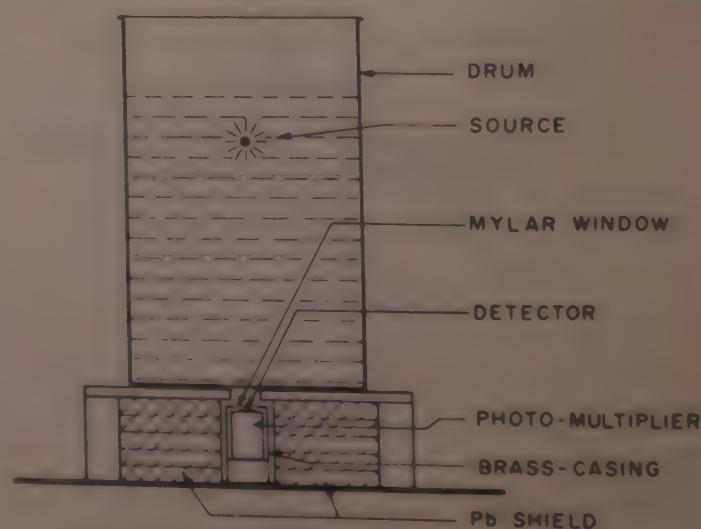


Fig. 1—Experimental arrangement



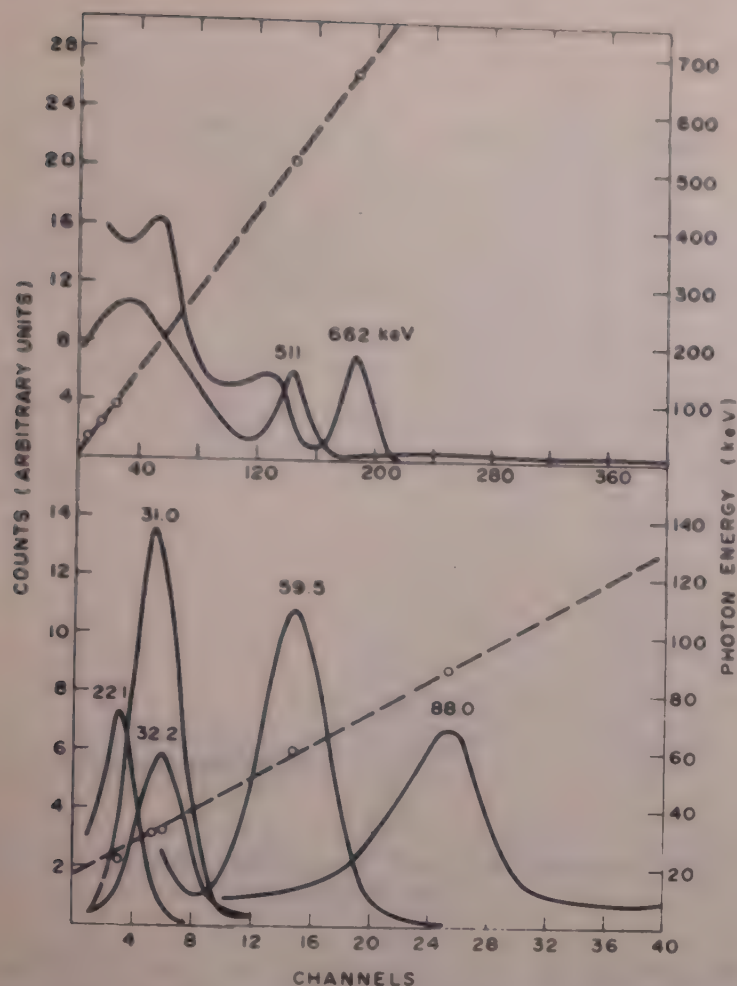


Fig. 2—Detector response for small point-sources kept 1.7 cm above the detector

The response of the detector to various low energy photons obtained by using point sources of known energy is shown in Fig. 2. It can be seen that the channel number varies linearly with energy. A thin detector was selected for these measurements because it has a low background and high sensitivity for low energy photons. Its only limitation is its poor resolution.

### 3 Measurements of Transmitted Spectra

The transmitted spectra were recorded with five different sources of energies and strengths as shown in Table 1. The strengths known to an accuracy of  $\pm 10\%$  were calculated from the data reported by Erdtmann and Soyka<sup>11</sup>. Point sources of these energies were kept at the axis of the drum.

Four sets of observations were recorded.

(i) In the first set, the sources were placed in a thin plastic cup glued on a thermocole float (2.5 cm thick) and the level of the water in the drum was changed from 10 cm to 90 cm in steps of 10 cm. The sources were, therefore, always 2.5 cm above water level. The spectra are shown in Figs 3 and 4.

(ii) In the second set, the drum was completely filled with water up to 90 cm. The spectra were recorded with sources placed in a water-tight plastic capsule and immersed in water from 10 cm to 80 cm deep in steps of

Table 1—Strengths of Sources

Source	Energy (keV)	Strength	
		mCi	$10^7$ photons/sec
$^{241}\text{Am}$	59.5	9.5	12.3
$^{57}\text{Co}$	122.1	4.7	15.0
	136.4		
$^{203}\text{Hg}$	279.2	61.8	186.3
$^{137}\text{Cs}$	661.6	6.0	17.5
$^{60}\text{Co}$	1250	2.5	16.8

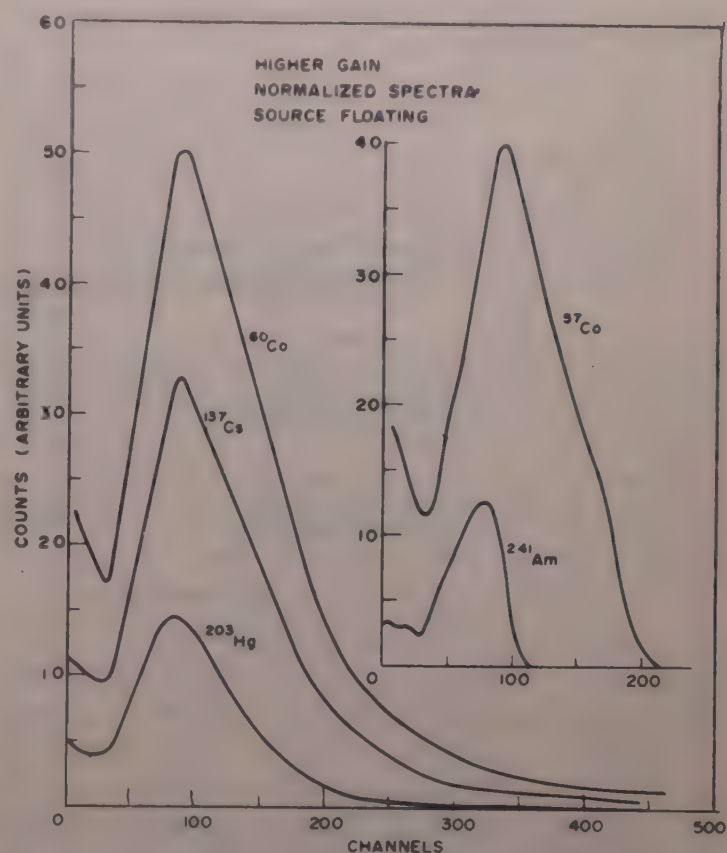


Fig. 3—Normalized transmitted spectra of floating sources (higher gain)

10 cm, with the help of a stone sink. These spectra are shown in Figs 5 and 6.

(iii) In the third set, the sources were kept in air at a fixed distance from the detector and transmitted spectra were recorded for different thicknesses of water in between.

(iv) In the last set, to determine the effect of back-scattering due to different thicknesses of water on the transmitted spectra, the drum was filled up to 50 cm with water. The sources were kept at a fixed position in the drum 40 cm above the bottom. The spectra were recorded with water level increasing in steps of 10 cm.

These spectra show changes in the count-rate with the thickness of water above the source within statistical limits of measurements. It is, therefore, concluded that the thickness of this medium beyond 10 cm behind the source does not affect the transmitted spectra for all the energies considered here.



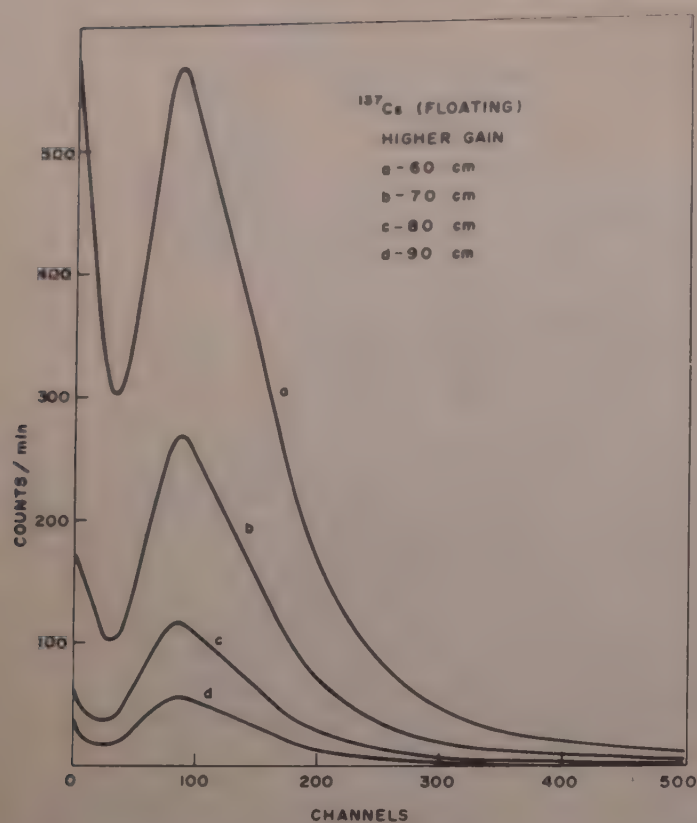


Fig. 4—Transmitted spectra of  $^{137}\text{Cs}$  source for different thicknesses of water (higher gain)

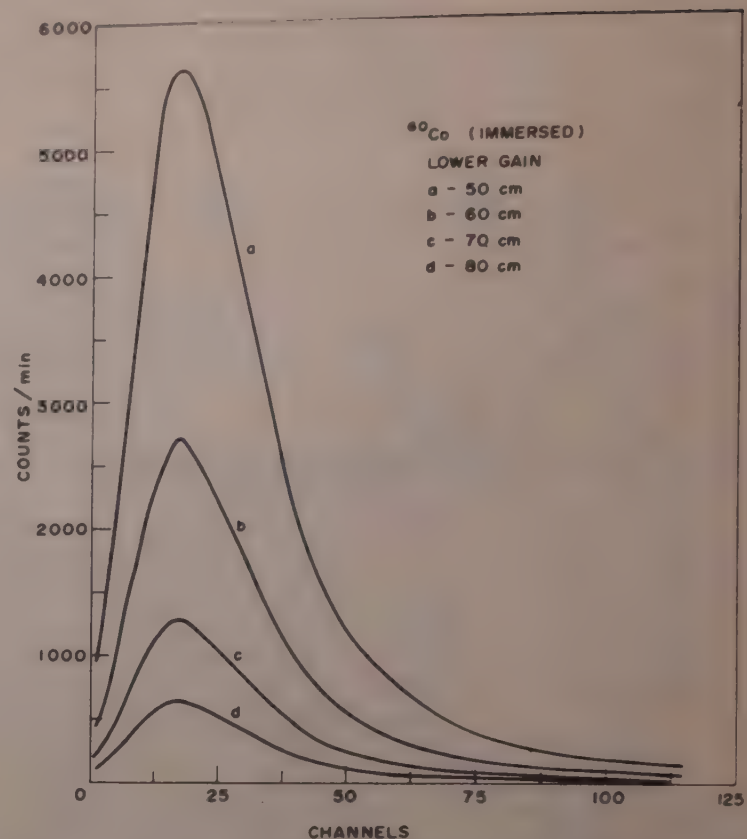


Fig. 6—Transmitted spectra of  $^{60}\text{Co}$  source for different thicknesses of water (lower gain)

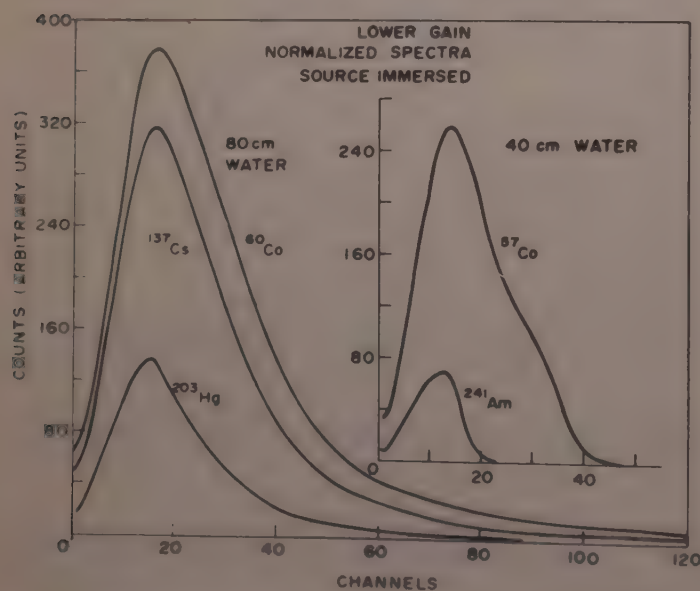


Fig. 5—Normalized transmitted spectra of immersed sources (lower gain)

#### 4 Results and Discussion

**Transmitted spectra**—In all the transmitted spectra shown in Figs 3-6, and the spectra not shown here, a broad peak at 60 keV is observed for all the thicknesses of water in all the experimental settings. Kazanskii<sup>9</sup> has also reported the peak at 60 keV in water. The full width at half maximum (fwhm) of this peak is more than that of 60 keV ( $^{241}\text{Am}$ ) peak measured under identical conditions. This shows that it is not a single energy peak but a band of continuous energies with maximum intensity at 60 keV.

To ascertain that the peak is not an electronics artifact, it is shifted to a higher channel by increasing

the gain of the system by about five times. It is seen from Figs 3 and 4 that the counts in the first few channels first reduce to a valley and then rise to form a peak at 60 keV. It is concluded that the peak is a property of the scattering medium through which the primary gamma-rays pass to the detector, irrespective of their energies and the medium transmits these photons preferentially. This peak is present in these spectra due to multiple scattering in water. Moreover, Minato<sup>12</sup> has shown with his Monte Carlo calculations in different media that the shape of low-energy, multiple-scatter peak in reflection and transmission spectra are quite similar to each other and it does not depend on the primary energy or thickness of the medium. The multiple-scatter energy is thus a characteristic constant of the medium.

As the primary energy of a photon is divided into several small energy photons in multiple scattering, it is expected that for the thickness of water more than about two corresponding mean free path (mfp) lengths, the higher the primary energy the more the number of 60 keV photons produced. In two mfp lengths of the medium, sufficient number of scatterings can take place to divide the primary energy. In Figs 3 and 5, the spectra of sources normalized to  $10^7$  photons/sec are shown for thicknesses of medium more than two mfp lengths. It is observed that for the same thickness of water, the peak intensity is more, the higher the primary energy of the incident photon. This confirms that higher primary energy produces more number of 60 keV photons for the same thickness of water. It is



also observed that fwhm for the peak increases with energy of the incident photon.

**Multiple-scatter coefficient**—A plot of logarithm of integrated counts for channels corresponding to energies from 40 to 80 keV (60 keV peak) versus thickness of water is a straight line as shown in Fig. 7. The Compton contribution of detector due to transmitted primary photons in this region was ignored because it was only 1-3% of these counts. A similar relationship has been reported elsewhere<sup>13</sup> for infinite air medium where the peak was at 72 keV energy.

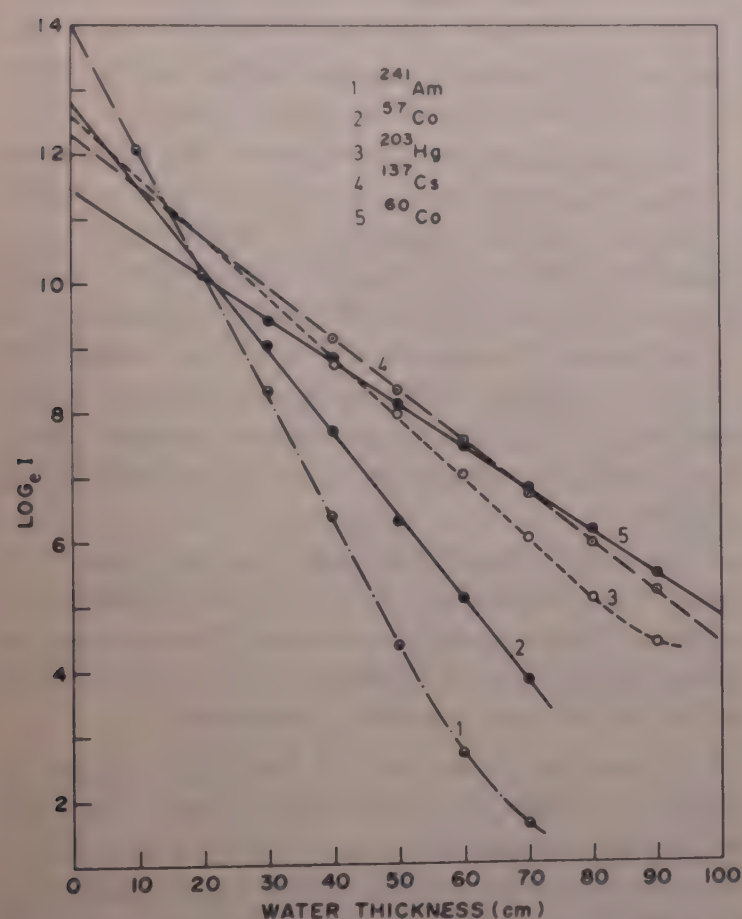


Fig. 7—Variation of logarithm of multiple-scatter peak (60  $\pm$  20 keV) counts with thickness of water

For all the sources and in both the experimental settings, source floating on and immersed in water, similar straight lines are obtained. This shows that the intensity ( $I$ ) of multiple-scatter photons is given by  $I = I_0 e^{-\mu d}$  where  $\mu$ , the slope, is called the multiple-scatter coefficient<sup>1</sup>, and  $d$ (cm) is the thickness of the medium. The values of the slopes (at 95% confidence level) for 60 keV peak as well as for different parts of scattered spectra for both the settings obtained by least squares method are given in Table 2. These are identical with the measurements with higher gain of the system. It is also observed that  $\mu$  values decrease with increase in incident energy. Thus,  $\mu$  is a characteristic constant of the medium which depends on incident energy, like linear attenuation coefficient.

The multiple-scatter coefficient is compared with linear attenuation coefficient of the medium in Fig. 8. The latter values at various energies are read out from a large smooth graph plotted from the data reported by Hubell<sup>14</sup>.

It can also be seen from Fig. 7 that the straight line changes its slope for higher thicknesses of water for the low energy sources like  $^{241}\text{Am}$  and  $^{203}\text{Hg}$ . This shows that the decrease in intensity of 60 keV photons is exponential only up to about 10 mfp. For thickness of the medium beyond 10 mfp, it seems that the multiple-scatter coefficient changes.

In the experimental setting (iii) where the source-detector distance is kept fixed and the thickness of water in between is varied, the exponential relationship mentioned above is not obtained although the intensity of 60 keV peak decreases with increase in thickness of water. This is due to the fact that the number of primary photons entering the scattering medium changes with source-detector geometry and the number of multiple-scatter photons depends on this number. In the first two settings, this number remains constant. Thus, the intensity of multiple-

Table 2—Exponential Coefficients ( $\mu$ ) and  $\ln I_0$  Values for Floating and Immersed Sources

Source	60 keV		Below 40 keV		Above 80 keV		Total scattered spectrum	
	$\ln I_0$	$\mu(\text{cm}^{-1})$	$\ln I_0$	$\mu(\text{cm}^{-1})$	$\ln I_0$	$\mu(\text{cm}^{-1})$	$\ln I_0$	$\mu(\text{cm}^{-1})$
Floating sources								
$^{241}\text{Am}$	$14.02 \pm 0.14$	$0.1918 \pm 0.0042$	—	—	—	—	$14.27 \pm 0.15$	$0.1964 \pm 0.0046$
$^{57}\text{Co}$	$12.78 \pm 0.17$	$0.1279 \pm 0.0036$	$10.90 \pm 0.11$	$0.1225 \pm 0.0033$	—	—	$13.65 \pm 0.19$	$0.1349 \pm 0.0039$
$^{203}\text{Hg}$	$12.71 \pm 0.05$	$0.0954 \pm 0.0007$	$11.50 \pm 0.02$	$0.0981 \pm 0.0004$	$13.53 \pm 0.13$	$0.1126 \pm 0.0023$	$13.73 \pm 0.06$	$0.1003 \pm 0.0009$
$^{137}\text{Cs}$	$12.28 \pm 0.05$	$0.0786 \pm 0.0008$	$10.90 \pm 0.05$	$0.0795 \pm 0.0008$	$12.82 \pm 0.08$	$0.0857 \pm 0.0012$	$13.34 \pm 0.07$	$0.0820 \pm 0.0011$
$^{60}\text{Co}$	$11.43 \pm 0.04$	$0.0660 \pm 0.0007$	$10.14 \pm 0.03$	$0.0680 \pm 0.0005$	$12.10 \pm 0.05$	$0.0710 \pm 0.0008$	$12.61 \pm 0.06$	$0.0691 \pm 0.0010$
Immersed sources								
$^{241}\text{Am}$	$14.43 \pm 0.10$	$0.1956 \pm 0.0024$	—	—	—	—	$14.57 \pm 0.13$	$0.1967 \pm 0.0030$
$^{57}\text{Co}$	$13.47 \pm 0.13$	$0.1373 \pm 0.0025$	$11.60 \pm 0.06$	$0.1342 \pm 0.0012$	—	—	$14.29 \pm 0.13$	$0.1427 \pm 0.0024$
$^{203}\text{Hg}$	$13.50 \pm 0.01$	$0.1052 \pm 0.0002$	$12.24 \pm 0.08$	$0.1082 \pm 0.0012$	$14.20 \pm 0.11$	$0.1182 \pm 0.0017$	$14.49 \pm 0.05$	$0.1092 \pm 0.0007$
$^{137}\text{Cs}$	$12.97 \pm 0.05$	$0.0876 \pm 0.0009$	$11.56 \pm 0.10$	$0.0892 \pm 0.0016$	$13.51 \pm 0.06$	$0.0925 \pm 0.0010$	$14.05 \pm 0.10$	$0.0903 \pm 0.0016$
$^{60}\text{Co}$	$12.07 \pm 0.11$	$0.0741 \pm 0.0017$	$10.71 \pm 0.11$	$0.0760 \pm 0.0017$	$12.56 \pm 0.14$	$0.0762 \pm 0.0023$	$13.13 \pm 0.19$	$0.0749 \pm 0.0031$



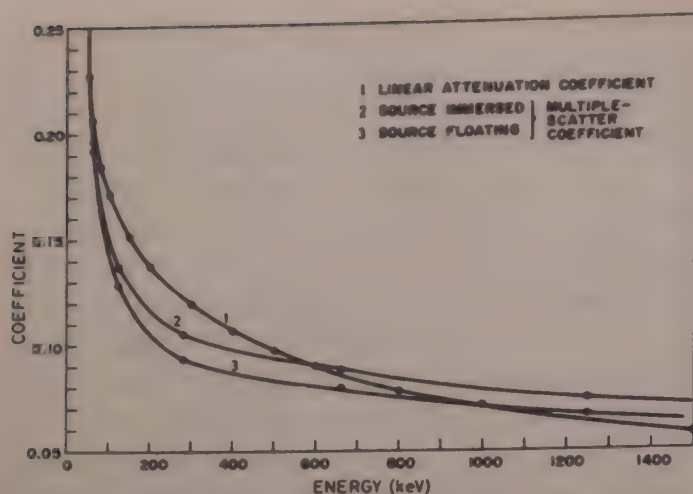


Fig. 8—Variation of multiple-scatter and linear attenuation coefficients of water with photon energy

scatter photons follows a simple exponential relationship in the first two settings.

*Halo around the source*—These are maximum number of primary photons available at the location of the source and they undergo maximum number of scatterings in the nearby medium. The intensity of multiple-scatter photons is maximum ( $I_0$ ) at the source as mentioned above, and it decreases exponentially with increase in distance from the source in the medium. This shows that the source, when placed in an infinite or semi-infinite scattering medium, is surrounded by a halo<sup>1</sup> of multiple-scatter photons exponentially decreasing in intensity as distance from the source increases, with the source itself as the centre of the halo.

It is also clear that the shape of the halo should be hemispherical if the source is placed at the surface of the scattering medium and spherical if the source is immersed in the medium. The intensity of multiple-scatter photons at the centre of the halo, i.e. at the source ( $I_0$ ) in the former case should be half that of the latter.

The values of logarithms of  $I_0$  for different sources normalized to  $10^7$  photons/sec are shown in Table 2 for sources floating on and immersed in water. It is shown in Table 3 that the ratio of  $I_0$  (immersed) and  $I_0$  (floating) is approximately 2 for different parts of the scattered spectrum, namely, 60 keV peak, below 40 keV, above 80 keV, and total spectrum. However, values much lower than 2 are obtained for  $^{241}\text{Am}$ .

Table 3—Ratio of  $I_0$  (Immersed) and  $I_0$  (Floating)

Source	60 keV peak	Below 40 keV	Above 80 keV	Total spectrum
$^{241}\text{Am}$	1.51	—	—	1.35
$^{60}\text{Co}$	1.99	2.02	—	1.91
$^{203}\text{Hg}$	2.19	2.68	1.95	2.19
$^{137}\text{Cs}$	2.01	1.92	2.00	2.03
$^{60}\text{Co}$	1.90	1.77	1.58	1.68

The source,  $^{241}\text{Am}$  (supplied by International Chemical and Nuclear Corporation, California, USA) has been contained in a small thin monel capsule with an opening on one side. It has partially obstructed the formation of spherical halo in the direction other than the opening when immersed in water, as the metal of the container attenuated the primary photons. The ratio is, therefore, less than 2.

The  $^{203}\text{Hg}$  source emits X-rays of energy between 70 and 85 keV which also undergo multiple scattering in water to show a peak at 60 keV. Its  $I_0$ -values are, therefore, somewhat higher. The  $^{60}\text{Co}$  source being of higher energy may possibly require larger dimensions of scatterer to show the same behaviour as other sources. The ratios of  $I_0$  values for this source below 40 keV and above 80 keV are lower than 2.

It may also be mentioned that it is very difficult to determine the value of  $I_0$  to an accuracy better than 15% because in the equation  $I = I_0 e^{-\mu d}$ , it is  $\ln I_0$  which is, in fact, least square fitted, and a small indeterminacy in  $\ln I_0$  raises the indeterminacy in  $I_0$  to a large extent. In addition, all the sources when kept floating, have been 2.5 cm above the surface of water, thus emitting 8% less photons into the medium than if they would have been just on the surface in  $2\pi$  geometry.

Considering these limitations, the ratios given in Table 3 are reasonably close to 2 and confirm the presence of hemispherical or spherical halo around the source depending on the location of the source—on the surface or inside the scattering medium.

It is observed from Table 2 that the  $\mu$ -values for immersed sources are consistently higher than those for floating sources. This shows that the intensity of photons of multiple-scatter energy reduces comparatively faster for immersed sources. While this intensity at the location of the sources is two times, at 40 cm distance it is only about 1.4 times that for floating sources. If the sources are immersed 10 cm and more under water surface, any measurable difference in the transmitted spectra at 40 cm distance is not expected. Thus, in the experimental setting (iv) above, it is found that the medium beyond 10 cm thickness behind the source does not affect the transmitted spectra at 40 cm distance.

The value of  $I_0$  decreases with increase in the energy of the source, but it does not seem to follow a pattern capable of being expressed by a simple function of energy. This, however, may also be due to the fact that the primary sources may not be exactly isotropic.

## 5 Conclusions

In the process of division of energy of a primary gamma photon into many photons of lower energy in a



medium, a pile-up of photons is observed at multiple scatter-energy, a characteristic constant of a scattering medium. The pile-up increases with the energy of primary photon. The medium transmits preferentially the photons of multiple-scatter energy.

A point source of energy higher than the multiple-scatter energy of a medium, when placed in the semi-infinite or infinite medium, is surrounded by a spherical halo of multiple-scatter photons extending far inside the medium, with the source itself as the centre of the halo. The intensity of the halo decreases exponentially with increase in distance in the medium. The coefficient of the exponential fall decreases with increase in primary source energy.

The intensity of primary gamma-rays falls according to the inverse square law. This law is implicit in the exponential relation discussed above. Thus, at larger distances in the medium, the multiple-scatter gamma-rays, particularly from a point source, become more important than the primary radiation. This work gives a simple formula for estimation of multiple-scatter gamma-rays.

The multiple-scatter peak may not be the only energy at which the pile-up of photons takes place in the whole process of thermalization of gamma energy. There may be other low energy pile-ups in soft- X-ray or ultraviolet region which could not be studied in this experiment.

### Acknowledgement

The authors are grateful to Shri S Somasundaram, Head, Radiation Hazards Control Section, for his keen interest in this work and for his many valuable suggestions. The help given by Shri M C Abani in calculations is gratefully acknowledged.

### References

- 1 Swarup J, *Nucl Instrum & Methods (Netherlands)*, **172** (1980) 559.
- 2 Brust R, *Kernenergie (Germany)*, **15** (1972) 193.
- 3 Minato S, *Nucl Sci & Eng (USA)*, **51** (1973) 32.
- 4 Shimizu A, *Nucl Sci & Eng (USA)*, **32** (1968) 184.
- 5 Scofield N E, *Nucl Sci & Eng (USA)*, **47** (1972) 1.
- 6 Alberg M, Beck H, O'Brien K & McLaughlin J E, *Nucl Sci & Eng (USA)*, **30** (1967) 65.
- 7 Theus R B, Beach L A & Faust W R, *J Appl Phys (USA)*, **26** (1955) 294.
- 8 Batrakov G F, Belyaev B N & Vinogradov A S, *At Energy (USSR)*, **33** (1972) 785; English translation in *Sov At Energy (USA)*, **33** (1972) 899.
- 9 Kazanskii Yu A, *At Energy (USSR)*, **8** (1960) 454; English translation in *Sov At Energy (USA)*, **8** (1961) 364.
- 10 Bishop G B, *Prog Nucl Energy (GB)*, **3** (1979) 67.
- 11 Erdtmann G & Soyka W, *Die  $\gamma$ -Linien der Radionuklide*; Rep: Jül 1003-AC (Nuclear Research Centre, Jülich, West Germany), 1973.
- 12 Minato S, Reports of the Government Industrial Research Institute, Nagoya (Japan), **21** (1972) 176 (in Japanese).
- 13 Swarup J & Ganguly A K, *Indian J Pure & Appl Phys*, **13** (1975) 595.
- 14 Hubbell J H, *Photon cross-sections, attenuation coefficients, and energy absorption coefficients from 10 keV to 100 GeV* (National Bureau of Standards, Washington, USA), Rep. NSRDS-NBS, **29** (1969) 64.



## Singlet-Singlet Absorption Spectra of 1-Amino- and 2-Methoxynaphthalenes

O P SHARMA†, H S BHATTI, N V UNNIKRISHNAN NAIR & R D SINGH\*

Physics Department, Maharshi Dayanand University, Rohtak 124 001

Received 28 June 1982; revised received 1 February 1983

The near ultraviolet absorption spectra of 1-amino- and 2-methoxynaphthalenes have been photographed and analyzed. The appearance of weak electronic and strong vibronic bands in the case of 1-aminonaphthalene has been interpreted in terms of totally symmetric vibronic interaction, a rare example in the literature. The spectrum of 1-aminonaphthalene shows the analogues of both  $a_g$ - and  $b_{3g}$ -type vibrations of naphthalene, the latter appearing more prominently than the former. On the other hand, the spectrum of 2-methoxynaphthalene shows two distinct systems of bands and the analogues of  $a_g$ -type vibrations appear prominently in both the systems.

### 1 Introduction

Earlier investigators<sup>1,2</sup> have reported the rotational contours of the pure electronic bands of 3200 Å system of 2-fluoro-, 2-hydroxy- and 2-aminonaphthalenes along with their 1-isomers. They have assigned strong electronic bands in all the cases except for 1-aminonaphthalene, where a weak band has been taken as the (0, 0) band. No explanation has, however, been given by these investigators for the abnormal behaviour of 1-aminonaphthalene vis-a-vis other sister molecules. Hence, we have taken up the study of singlet-singlet absorption spectrum of 1-aminonaphthalene along with that of 2-methoxynaphthalene in greater detail than available in the literature. The study strengthens the viewpoint that the spectra of some 1-substituted naphthalenes provide the most appropriate examples of totally symmetric vibronic interaction<sup>3</sup>.

### 2 Experimental Details

To photograph the various regions of the absorption spectra arising in the different cases with proper intensity and illumination, different cells were tried. The cell, which was found to be most versatile, was closed at the two ends by a pair of quartz to pyrex graded seals and a bulb of about 2 cc in volume attached in the middle. In both the cases, after filling the substance in the bulb and putting it into an ice bath, the absorption column was evacuated by a rotary pump for about half an hour and sealed off. The temperature of this sealed tube was varied from room temperature to 125°C with the help of a home-made cylindrical furnace.

The spectra were photographed on Russian ESP-30

medium quartz spectrograph, using Ilford N-40 and Kodak B-10 photographic plates. The wave number of the bands given in the Tables 1&2 are the band head positions for sharp and discrete bands and the intensity maxima in case of broad and diffuse bands\*.

### 3 Results

With the above mentioned absorption column of 140 cm in length, it was found that different regions of the absorption spectra were developed at different temperatures. In the case of 2-methoxynaphthalene, the bands in the region 2500-2825 Å start developing at

Table 1—Analysis of the Absorption Spectrum of 1-Aminonaphthalene (System I)

Wave-number (cm <sup>-1</sup> )	Relative intensity	Separation from the (0-0) band (cm <sup>-1</sup> )	Assignment
29588	2	-458	0-458
29911	1	-135	0-135
29987	1	-59	0-59
30046	4	0	0-0
30269	2	223	0-223
30313	2	267	0+289-23
30335	4	289	0+289
30416	5	370	0+370
30453	3	407	0+407
30510	6	464	0+464
30534	8	488	0+504-23
30557	10	511	0+511
30776	6	730	0+730
30887	4	841	0+841
31243	2	1197	0+511+686
31442	1	1396	0+1396
31889	1	1843	0+511+1332

† Present address: Department of Physics, Government College, Faridabad (Haryana).

\* The accuracy of measurements varies between  $\pm 3$  cm<sup>-1</sup> for sharp and discrete bands and  $\pm 10$  cm<sup>-1</sup> for broad and diffuse bands.



Table 2—Analysis of the Absorption Spectrum of 2-Methoxynaphthalene

Wave-number ( $\text{cm}^{-1}$ )	Relative intensity	Separation from the (0,0) band ( $\text{cm}^{-1}$ )	Assignment
System I			
30398	2	-621	0-621
30938	1	-81	0-81
30991	1	-28	0-28
31019	10	0	0-0
31460	3	441	0+441
31733	3	714	0+714
31995	1	976	0+976
32413	8	1394	0+1394
32440	1	1421	0+2 × 714
32880	2	1861	0+2 × 714+441
33141	3	2122	0+1394+714
33483	1	2364	0+1394+976
33603	0	2584	0+3 × 714+441
33842	2	2823	0+1394+2 × 714
35191	1	4172	0+3 × 1394
System II			
36192	10	0	0,0
36591	8	399	0+399
37573	5	1381	0+1381
37958	3	1766	0+1381+399
38965	1	2773	0+2 × 1381
39356	0	3164	0+2 × 1381+399

about 40°C and the best condition is achieved when the temperature of the cell becomes  $\sim 48^\circ\text{C}$ . On the other hand, the bands in the region 2850-3300 Å are best developed at 100°C.

The situation in the case of 1-aminonaphthalene is, however, found to be altogether different. In this case, a much wider region of absorption starting from 2450 Å to 3450 Å (Fig. 1) is found with the banded structure only on the longer wavelength side. This banded structure slowly merges into a continuous absorption towards the shorter wavelength side of the spectrum. At the lowest temperature of the cell, i.e. at about 30°C, a continuous absorption appears only in the region below 2300 Å. When the temperature of this 140 cm cell is slowly increased, absorption starts developing in the region 2450-3100 Å which does not possess any structure. Banded structure starts developing in a narrow region, viz. 3100-3450 Å, at about 55°C, and the best structure develops at  $\sim 68^\circ\text{C}$ . No further structure is found to be developing even when the temperature of the cell is raised up to 125°C.

#### 4 Study of Plates

The absorption spectra of 1-amino- and 2-methoxynaphthalenes are shown in Figs 1 & 2 respectively. The longest wavelength side of the absorption spectrum, in both the cases, consists of a number of well defined and sharp bands degraded towards red (Figs 1&2). These

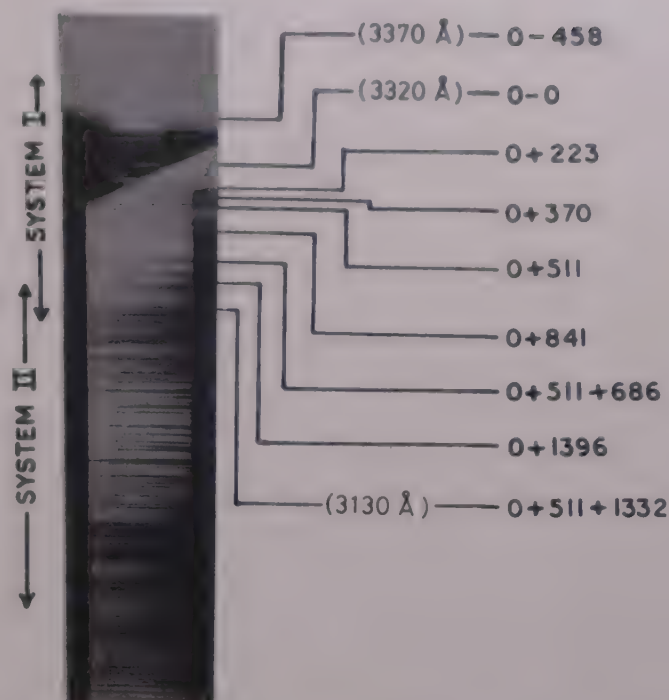


Fig. 1—Absorption spectrum of 1-aminonaphthalene

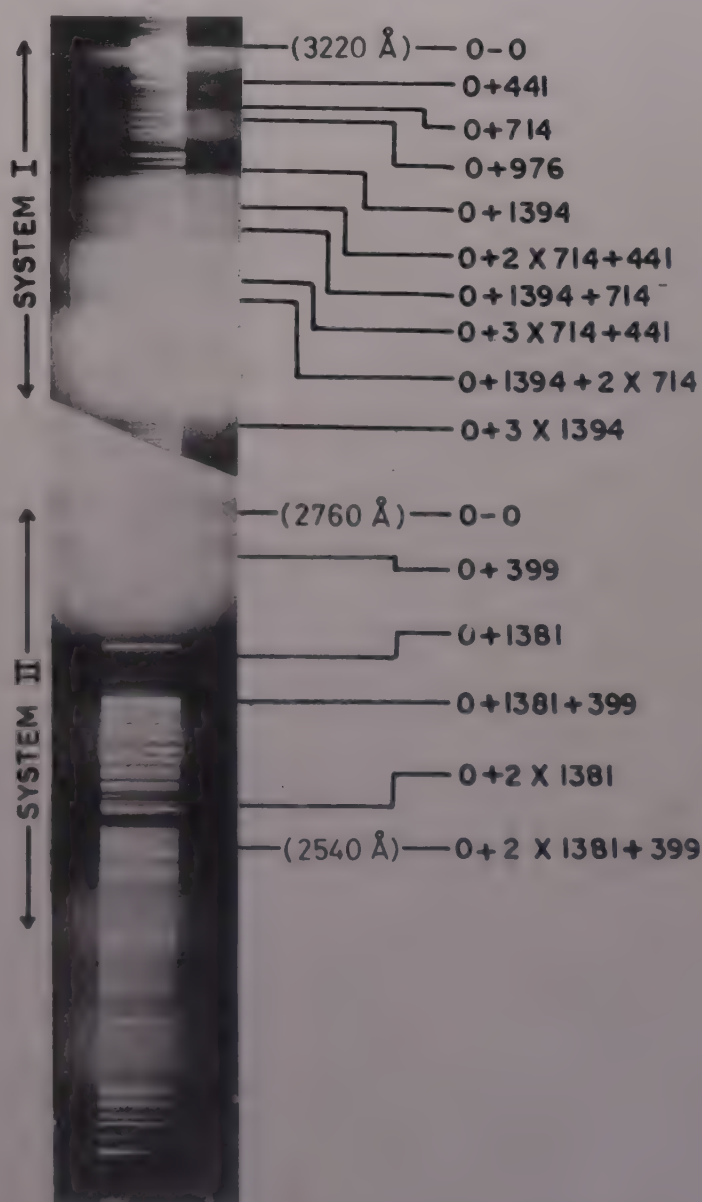


Fig. 2—Absorption spectrum of 2-methoxynaphthalene



bands become diffuse and broad towards the shorter wavelength side of the spectrum. In the case of 2-methoxynaphthalene, the structure of the bands and their development at different temperatures show very clearly that this molecule gives two discrete absorption regions: one in the region 2850-3300 Å (system I) and other in the region 2500-2850 Å (system II). There is also a third region of almost continuous absorption extending from 2300 Å to shorter wavelength side.

On the other hand, the situation in the case of 1-aminonaphthalene seems to be altogether different. In this case, on the basis of analogy drawn from the spectrum of 2-methoxynaphthalene, one can very well say that the two systems (I and II) are merged together due to the large bathochromic shift of the absorption system II (Fig. 1).

## 5 Analysis and Discussion

Both the molecules under investigation may be taken as belonging to the  $C_s$  point group with the molecular plane as the only element of symmetry, if the substituents  $NH_2$  and  $OCH_3$  are taken to be point masses lying in the plane of the ring<sup>4</sup>. A correspondence of the regions of absorption and the similarities in the gross structure of the bands show that the system I of these molecules should correspond to the longest wavelength (2900-3300 Å) ultraviolet system of naphthalene, which is assigned to  $^1B_{2u} - ^1A_g$  transition. On the reduction of symmetry from  $D_{2h}$  to  $C_s$ , both the upper and lower states of naphthalene are reduced to totally symmetric  $A'$ -type<sup>4</sup>. Hence the system I of these molecules should be attributed to an allowed electronic transition of the type  $^1A' - ^1A'$ .

A similar correspondence of the regions of absorption and gross structure of the bands shows that system II should correspond to the shorter wavelength (2500-2900 Å) ultraviolet system of naphthalene, which is assigned to  $^1B_{1u} - ^1A_g$  transition. Both these electronic states are also reduced to totally symmetric  $A'$ -type. Thus the system II, similar to the system I, is also assigned to allowed electronic transition of the type  $^1A' - ^1A'$ .

### 5.1 Aminonaphthalene

In case of an allowed electronic transition, the most intense band or one of the strongest bands on the longer wavelength side of the system should be taken as the (0, 0) band. However, in the case of 1-aminonaphthalene the system II does not give any banded structure and in system I a weak band at  $30046\text{ cm}^{-1}$  has been assigned as the (0, 0) band. In the latter case, if the most intense band at  $30557\text{ cm}^{-1}$  is taken as the pure electronic band, the ground state intervals of 511 and  $969\text{ cm}^{-1}$  associated with the prominent bands at 30046 and  $29588\text{ cm}^{-1}$  are not

supported by the infrared spectrum. In the present case, when the weak band is taken as the (0, 0) band, the ground state interval of  $470\text{ cm}^{-1}$  can very well be correlated to the infrared frequency of  $475\text{ cm}^{-1}$ .

### 5.2 Mode of Interaction

Since the symmetry of 1-aminonaphthalene is different from that of naphthalene, the type of vibronic interaction responsible for the intensification of bands in case of naphthalene may not be expected in this case. The present study indicates, as mentioned earlier, that the system II of 1-aminonaphthalene is shifted very much towards the longer wavelength side of the spectrum, leading to the merger of the two systems. This indicates that two excited electronic states of naphthalene come closer together due to the substitution of  $NH_2$  group at the 1-position of the ring. Since both of these states are totally symmetric  $A'$ -type, an interaction of the two systems is possible<sup>5,6</sup> due to a totally symmetric vibration of the lower electronic state. Similar type of interaction has been proposed earlier<sup>3</sup> by our group in case of 1-chloro-, 1-bromo- and 1-iodonaphthalenes. In fact, the spectra of 1-substituted (1-chloro, 1-iodo, etc.) naphthalenes seem to be the best examples of totally symmetric vibronic interaction. Investigations in case of 3500 Å system of azulene<sup>7</sup> and phenanthrene<sup>8</sup> have indicated the occurrence of totally symmetric vibronic interactions. These systems, however, do not fulfil all the requirements of such interactions. "The overtone of the perturbing frequency is not observed in the spectrum of phenanthrene though the theory demands it<sup>8</sup>". The spectra of 1-halonaphthalenes<sup>9</sup>, on the other hand, show the evidence of the perturbing frequency also forming the Franck-Condon progressions. In 1-aminonaphthalene, the harmonics of the perturbing vibration could not, however, be traced due to the diffuseness of bands associated with the overlapping of the two systems.

Another interesting feature of the absorption spectrum of 1-aminonaphthalene seems to be the large bathochromic shift of the absorption system I. The observed shift of the (0, 0) band in this case is  $1974\text{ cm}^{-1}$ , which is much larger than the corresponding shifts reported in the spectra of other 1-substituted naphthalenes. For the sake of comparison some of these shifts are given below:

	Ref.	(0, 0) band (system I)	Shift ( $\text{cm}^{-1}$ )
1-Hydroxynaphthalene	4	31453	567
1-Methoxynaphthalene	10	31349	671
1-Fluoronaphthalene	9	31871	149
1-Chloronaphthalene	9	31576	444
1-Bromonaphthalene	9	31568	452
1-Iodonaphthalene	9	31485	535



In the first instance, the present result seems to be contradicting the earlier ones, indicating that the 1-substitution produces smaller bathochromic shift in system I than in system II. But the overlapping of the two systems produced, even under this condition, gives the clear indication of the fact that the shift in the system II is even larger.

The excited state frequency  $511\text{ cm}^{-1}$  appearing with the most intense band is attributed to the perturbing mode in the first excited state. According to the assignment made in case of 1-halonaphthalene<sup>3</sup> this should be assigned to the skeletal distortion mode corresponding to  $506\text{ cm}^{-1}$  ( $b_{3g}$ -type) fundamental of naphthalene. Surprisingly, earlier investigators<sup>1,2</sup> have ignored this most prominent band while correlating the spectrum of 1-aminonaphthalene with that of aniline.

The prominent excited state frequency of  $289\text{ cm}^{-1}$  is attributed to the 1-1 sequence of the inversion vibration. Corresponding frequency in the case of aniline has been reported<sup>10</sup> to be appearing at  $293\text{ cm}^{-1}$ . In the present case, the combinations of the inversion vibrations ( $I_1^1$ ) with the ring mode could not, however, be established due to the diffuseness of the bands.

Other prominent bands appearing in absorption system I of 1-aminonaphthalene have been understood in terms of the excited state frequencies of 223, 289, 370, 407, 464, 511, 730, 1197,  $1396\text{ cm}^{-1}$  and the ground state frequencies of 135 and  $458\text{ cm}^{-1}$ . The assignments are given in Table 1.

### 5.3 2-Methoxynaphthalene

Contrary to the case of 1-aminonaphthalene, 2-methoxynaphthalene shows two distinct systems with banded structure. The (0, 0) bands have been assigned at  $31019$  and  $36192\text{ cm}^{-1}$  in systems I and II respectively. Both of these bands appear first in their respective systems, when the temperature of the cell is slowly increased, and develop into the strongest band of the system in each case (Fig. 2).

The above assignment shows that the bathochromic shifts are  $1001$  and  $-282\text{ cm}^{-1}$  for systems I and II respectively. The large bathochromic shift observed in the case of system I is in conformity with the similar shifts reported in the case of other 2-derivatives of naphthalene. This also indicates that the longest wavelength ultraviolet system of naphthalene is polarized along the long in-plane axis of the molecule. This makes the effect of 2-substitution prominent because it affects the dipole moment parallel to the long in-plane axis. Other prominent bands of system I have been analyzed in terms of the excited state fundamentals  $441$ ,  $714$ ,  $976$ ,  $1394\text{ cm}^{-1}$  and the ground state fundamental  $621\text{ cm}^{-1}$ .

The absorption system II, on the other hand, has been analyzed in terms of only two excited state fundamentals, viz.  $399$  and  $1381\text{ cm}^{-1}$ . Though the bands in system II are very broad and diffuse, the prominence of the excited state fundamental  $1381\text{ cm}^{-1}$  can be marked even in the first instance. It forms very good Franck-Condon progression and combination with the excited state frequency  $399\text{ cm}^{-1}$ . An interesting feature associated with this fundamental is that its intensity increases with the rise of temperature, a fact which could not be understood.

Similar to the case of system II, in system I also the excited state frequency  $1394\text{ cm}^{-1}$  appears very prominently, and forms progression as well as combinations with almost all the excited state fundamentals. On the basis of the comparison drawn from the emission and absorption spectra of 1- and 2-fluoro-, 2-methyl- and 2-hydroxynaphthalenes reported earlier<sup>9,11-13</sup>, the  $1394\text{ cm}^{-1}$  excited state frequency of 2-methoxynaphthalene is correlated\* with the infrared frequency  $1385\text{ cm}^{-1}$ . The slight increase in the magnitude of this fundamental is in conformity with the behaviour of its analogues in other 2-derivatives. This may be interpreted as the tightening up of the molecule while vibrating in this mode in the excited state. The excited state frequencies reported in absorption for systems I and II of other 2-derivatives, along with their probable ground state analogues obtained from the emission spectra, are summarized below:

Compound	Ref.	Frequency, $\text{cm}^{-1}$		Emission
		System I	System II	
1-Fluoronaphthalene	14	1434	1375	1385
2-Fluoronaphthalene	13	1427	1378	1384
2-Chloronaphthalene	12	1428	1393	—
2-Bromonaphthalene	9	1431	1400	—
2-Naphthol	4	1380	1371	1400
2-Methylnaphthalene	11	1430	1412	1387

In the case of 2-fluoronaphthalene<sup>13</sup>, where good emission spectrum could be recorded, unambiguous assignment of this fundamental would not be possible because the ring breathing mode has exactly half the magnitude of the above fundamental.

In the present case, the excited state frequency  $714\text{ cm}^{-1}$  is assigned to the ring breathing mode. Similar excited state frequencies have been reported in absorption system I of other 2-derivatives of naphthalene. The unambiguous assignment of the  $1394\text{ cm}^{-1}$  frequency in the present case has been possible because  $2 \times 715\text{ cm}^{-1}$  differs very much from  $1394\text{ cm}^{-1}$ .

\*Unpublished data.



The analysis of the bands observed in systems I and II are given in Table 2.

### Conclusion

The present study indicates that the system II of monosubstituted naphthalenes, though consisting of broad and diffuse bands, plays the vital role in the intensity distribution of bands in the absorption system I. The two excited states involved come closer together in case of 1-substituted naphthalenes showing larger bathochromic shift for system I than for system II. This is the prime requirement for totally symmetric vibronic interaction as envisaged theoretically<sup>6</sup>.

### Acknowledgement

The authors are thankful to Prof. N Nath, Head of the Physics Department, Kurukshetra University, Kurukshetra, for providing adequate facilities and showing keen interest in the work. One of the authors (HSB) is also thankful to the University Grants

Commission, New Delhi for financial assistance during the course of this work.

### References

- 1 Hollas J M & Thakur S N, *Mol Phys (GB)*, **25** (1973) 1315.
- 2 Hollas J M & Thakur S N, *Mol Phys (GB)*, **27** (1974) 1001.
- 3 Shambu N Singh & Singh R D, *J Mol Spectrosc (USA)*, **65** (1977) 20.
- 4 Singh R D & Singh R S, *Indian J Pure & Appl Phys*, **3** (1965) 418.
- 5 Herzberg G, *Molecular spectra and molecular structure*, Vol III (Van Nostrand-Reinhold Co, New York), 1966, 140.
- 6 Albrecht A C, *J Chem Phys (USA)*, **33** (1960) 156.
- 7 Hunt G R & Ross I G, *J Mol Spectrosc (USA)*, **9** (1960) 50.
- 8 Craig D P & Gordon R D, *Proc Roy Soc London A (GB)*, **288** (1965) 69.
- 9 Shambu N Singh, *Spectral studies of monohalo-naphthalenes*, Ph D thesis, Kurukshetra University, Kurukshetra, 1977.
- 10 Brand J C D, William D R & Cook T J, *J Mol Spectrosc (USA)*, **20** (1966) 359.
- 11 Singh R D & Singh R S, *Indian J Pure & Appl Phys*, **4** (1966) 89.
- 12 Singh S N, Sharma O P & Singh R D, *Spectrosc Lett (USA)*, **8** (1975) 7.
- 13 Singh R D, *Indian J Pure & Appl Phys*, **13** (1975) 48.
- 14 Majjit D & Banerjee S B, *Spectrochim Acta Vol A (GB)*, **30** (1974) 277.



## Fermi Levels in MIS(n) Solar Cells

K SEN\*

D B S College, Dehradun

&

P S MATHUR

D A V College, Dehradun

Received 22 May 1982

Understanding the performance of a metal-insulator-semiconductor (MIS) solar cell requires the knowledge of the position of Fermi level for majority carriers ( $E_{fn}$ ), minority carriers ( $E_{fp}$ ) and interface states ( $E_{fi}$ ). This note reports the study of  $E_{fn}$ ,  $E_{fp}$ , and  $E_{fi}$  at the insulator-semiconductor (I-S) interface, under different biasing conditions as a function of insulator thickness ( $d$ ).

In MIS(n) solar cells, the majority carrier Fermi level is generally assumed to be flat<sup>1-5</sup> under all biasing conditions. Under illumination, the minority carrier Fermi level is shown to have a negative slope close to I-S interface. Recently, Sen *et al.*<sup>6</sup> (by assuming  $\Delta E_{fn} \neq 0$ ), and shortly later Klompke and Landsberg<sup>7</sup> have shown by detailed mathematical analysis that  $E_{fn}$  has a peak near the I-S interface. Neilson<sup>4</sup> considered that under illumination the interface state Fermi level is positioned somewhere between metal Fermi level ( $E_{fm}$ ) and the minority carrier Fermi level.

Under thermal equilibrium all the Fermi level in the MIS solar cell are positioned at the same energy level, i.e.  $E_{fi} = E_{fm} = E_{fn}$ . In case of MIS(n) solar cell with  $d < 10\text{\AA}$ , under dark (D) biasing the interface state Fermi level lies somewhere between  $E_{fn}$  and  $E_{fp}$ . For large insulator thickness ( $d$ ), due to reduced tunneling probability  $T_n = \exp(-\chi^{*1/2}d)$  and increased electron concentration [ $n(0) > p(0)$ ] at the interface, the number of electrons captured at the interface is increased; thereby  $E_{fi}$  moves toward the electron quasi-Fermi level ( $E_{fn}$ ). The above consideration leads to an empirical relation for  $E_{fiD}$ <sup>8,9</sup> as follows:

$$E_{fiD}(0) = [(E_{fn} - E_{fm})_{X=0}] [1 - \exp(-\chi^{*1/2}d)] \quad \dots (1)$$

In Eq. (1),  $X = 0$  refers to interface. In writing the above equation we have assumed that  $V = (E_{fn} - E_{fm})_{X=0}$ .  $\chi^*$  is the effective barrier height for electrons.

Under illumination, the condition at the interface changes to that of excess of holes due to accumulation of holes at the I-S notch effected by the reduced tunneling of the minority carriers. This excess concentration is negligible for  $d < 10\text{\AA}$ , but increases rapidly for further increase of  $d$ . Assuming  $p(0) > n(0)$  and  $\sigma_p > \sigma_n$  at all  $V$ , it might be said that the interface states are depleted of electrons due to excess of hole

Table 1—Calculated Values of  $(E_{fp} - E_{fm})$ ,  $(E_{fiD} - E_{fm})$  and  $(E_{fiL} - E_{fm})$  at the I-S Interface Under Different Biasing Conditions for Different  $d$  (in  $\text{\AA}$ ) Values

$d$	$(E_{fp} - E_{fm})^\dagger$	$(E_{fp} - E_{fm})^\ddagger$	$(E_{fiL} - E_{fm})^\dagger$	$(E_{fiD} - E_{fm})^\ddagger$	$(E_{fiL} - E_{fm})^\ddagger$
5	-0.041	-0.041	-0.032	0.318	0.285
10	-0.082	-0.082	-0.078	0.385	0.305
15	-0.123	-0.120	-0.122	0.396	0.277
20	-0.164	-0.149	-0.164	0.4	0.251
25	-0.205	-0.164	-0.205	0.4	0.236

$^\dagger$  For  $V = 0\text{ V}$  and  $^\ddagger$  for  $V = 0.4\text{ V}$ ;  $d$  in  $\text{\AA}$  and all  $E$ 's in eV ( $E_{fiD} - E_{fm})^\ddagger = 0$  for all  $d$  (5-25 $\text{\AA}$ )

flow towards the interface. Thus, depending upon  $\sigma_n$ ,  $\sigma_p$ ,  $n(0)$ ,  $p(0)$  and  $V$ , the interface state Fermi level approaches  $E_{fn}$  or  $E_{fp}$ .

The respective currents due to flow of electrons ( $J_{se}$ ) and holes ( $J_{sh}$ ) into the interface states are expressed by<sup>1</sup>

$$J_{se} = qN_{ss}\sigma_n v[(1 - f_s)n(0) - n_1 f_s] \quad \dots (2)$$

$$J_{sh} = qN_{ss}\sigma_p v[f_s p(0) - (1 - f_s)p_1] \quad \dots (3)$$

where  $f_s$  is the occupation function at the interface and  $\sigma_n$  and  $\sigma_p$  are respectively the capture cross-sections for electrons and holes.

The above discussion suggests that under short circuit condition ( $V = 0$ )  $E_{fiL}$  can be expressed by the following empirical relation:

$$E_{fiL}(0) \sim (E_{fp} - E_{fm})_{X=0} [1 - \exp(-\chi^{*1/2}d)] \quad \dots (4)$$

and under biasing

$$E_{fiL}(0) \sim (E_{fn} - E_{fp})_{X=0} [1 - \exp(-\chi^{*1/2}d)] \quad \dots (5)$$

The validity of these empirical relations is enhanced by the fact that they help in calculating diode quality factor which reasonably explains<sup>8,9</sup> the experimentally observed variations<sup>10</sup> under dark and illumination conditions.

The quasi-Fermi level  $E_{fp}$  is calculated considering the continuity equation for holes<sup>2,11</sup>,

$$A^* T^2 T_n \exp\left[-\frac{(E_{fp} - E_v)_{X=0}}{KT}\right] \simeq J_L - J_{od} \exp\left[\frac{(E_{fn} - E_{fp})_{X=0}}{KT}\right] - J_{or} \exp\left[\frac{(E_{fn} - E_{fp})_{X=0}}{KT}\right] \quad \dots (6)$$

In Eq. (6), the LHS denotes the hole current through the insulator. The first, second and third terms on the RHS of Eq. (6) are respectively the photo-generated



current, back diffusion current and the depletion region recombination current. Calculations are done with  $J_L = 36 \text{ mA/cm}^2$ ,  $J_{od} = 10^{-11} \text{ A/cm}^2$ ,  $J_{or} = 10^{-8} \text{ A/cm}^2$ ,  $\chi^* = 0.1 \text{ eV}$  and  $(E_{fm} - E_v)_{x=0} = 0.3 \text{ eV}$ . It is also assumed that under short circuit condition and  $d=0\text{\AA}$  the tunneling hole current [LHS of Eq. (6)] is  $J_L$ .

Table 1 gives the calculated values of  $E_{fp}$ ,  $E_{fid}$  and  $E_{fil}$  with respect to  $E_{fm}$  at I-S interface under different biasing conditions. It shows that: (a) under all biasing,  $E_{fp}$  moves toward valence band edge with increasing  $d$ , (b) at large  $d$ ,  $E_{fp}$  is positioned closer to  $E_{fm}$  for  $V \neq 0$  than under short circuit case, (c) interface state Fermi level under the dark condition is positioned in between  $E_{fn}$  and  $E_{fm}$ , (d) interface state Fermi level under short circuit condition lies below the metal Fermi level and

(e) the interface state Fermi level under illumination and  $V \neq 0$  lies above metal Fermi level.

# References

- 1 Card H C, *Solid State Electron (GB)*, **22** (1979) 817.
- 2 Olsen L C, *Proc 12th IEEE Photo Specialist Conf (USA)*, (1976) 854.
- 3 Card H C & Yang E S, *Appl Phys Lett (USA)*, **29** (1976) 51.
- 4 Neilson O M, *IEE Solid State & Electron Devices (GB)*, **3** (1979) 57.
- 5 Singh R, Green M A & Rajkanan K, *Sol Cells (GB)*, **3** (1981) 95.
- 6 Sen K, Jain B K & Srivastava V K, *Sol Cells (GB)*, **3** (1981) 1.
- 7 Klimpke C M H & Landsberg P T, *Solid State Electron (GB)*, **24** (1981) 401.
- 8 Sen K, *Phys Status Solidi (a) (Germany)*, **71** (1982) 641.
- 9 Sen K & Srivastava R S, *Sol Cells (GB)*, **7** (1983) 219.
- 10 Card H C, *Solid State Electron (GB)*, **20** (1977) 971.
- 11 Sen K & Srivastava R S, *Phys Status Solidi (a) (Germany)*, **69** (1982) 413.



## Magnetic Studies of the System $\text{ZnFe}_{1-x}\text{Mn}_x\text{CrO}_4$

P S JAIN & V S DARSHANE\*

Solid State Laboratory, Chemistry Department, Institute of Science  
Bombay 400032

Received 10 May 1982; revised received 14 February 1983

Magnetic susceptibility ( $\chi_M$ ) measurements at low temperature (78-296 K) were carried out for different compositions of the system  $\text{ZnFe}_{1-x}\text{Mn}_x\text{CrO}_4$ . The compounds showed antiferromagnetic behaviour. The Curie constant values varied between 3.94 and 4.85 and increased with increase in  $\text{Fe}^{3+}$  ion concentration at B-site. Paramagnetic Curie temperature varied between -20 K and -287 K, showing that B-B interaction decreases with increase in  $\text{Fe}^{3+}$  ion concentration in the lattice;  $\chi_M$  data indicated that all the cations ( $\text{Fe}^{3+}$ ,  $\text{Cr}^{3+}$  and  $\text{Mn}^{3+}$ ) are in high-spin states only.

Ferrites have interesting structural, electrical and magnetic properties which are suited for a variety of applications. These properties depend crucially upon the nature, the valence states and distribution of these metal ions over two sites in spinel ( $\text{AB}_2\text{O}_4$ ) lattice. In oxidic spinels if both A- and B-sites are occupied by magnetic ions, then stronger A-B interaction controls the magnetic behaviour of the materials and we cannot get much information regarding B-B interaction. However, if A-site is occupied by diamagnetic ion, then B-B interaction becomes quite predominant. Literature survey<sup>1-5</sup> revealed that considerable amount of work has been reported on magnetic properties containing two transition elements and very little work has been mentioned with three transition elements at B-site. We have already studied the structural, electrical, infrared and Mössbauer studies<sup>7</sup> of the system  $\text{ZnFe}_{1-x}\text{Mn}_x\text{CrO}_4$ . The present work was further taken up with a view to investigating the effect of cation-cation interaction on magnetic susceptibility parameters ( $C_M$ ,  $\theta_a$  values) containing three transition metal ions at B-site in the system mentioned above.

**Experimental details**—All the compounds of the system were prepared by the standard ceramic technique described earlier<sup>6</sup>. Magnetic susceptibility measurements at low temperatures (78-296 K) were carried out using Gouy method. A field strength of 7.6 kG was used throughout the investigation. The susceptibility was measured at various temperatures using liquid  $\text{N}_2$ . For temperature measurements copper-constantan thermocouple was used.

**Results and discussion**—Paramagnetic susceptibility of all the compounds was measured from 78 K to

296 K and the plot of  $1/\chi_M$  versus  $T$  is shown in Fig. 1;  $\chi_M$  is the molar magnetic susceptibility. All the compositions indicated linear nature of the plots, i.e. obeying the Curie-Weiss law, and showed antiferromagnetic behaviour. The values of  $C_M$  (Curie constant) and  $\theta_a$  (paramagnetic Curie temperature) were calculated from the slopes and intercepts of linear plots. The results of magnetic data are summarized in Table 1. The variation of  $\theta_a$ ,  $C_M$  (obs. and calc.) with the composition of the ferrite is given in Fig. 2. The  $\theta_a$  values of the system  $\text{ZnFe}_{1-x}\text{Mn}_x\text{CrO}_4$  varied between -20 K and -287 K and showed increasing trend with increase in concentration of  $\text{Fe}^{3+}$  ions at B-site.

There are mainly two types of exchange interactions: (I) the direct interaction caused by the direct electrostatic interaction and overlap of orbitals of magnetic electrons, and (II) the superexchange interactions via an intermediate non-magnetic ion. Goodenough<sup>8</sup> has mentioned that cation-cation interaction will be significant if the cations have  $3d^m$  ( $m < 5$ ) electronic configuration and the occupied octahedra share a common edge. Similarly, if  $m < 3$  the cation-cation interactions are very strong and even stronger than the superexchange interactions.  $\theta_a$  values are very characteristic of metal-metal interactions present in the lattice. The values of  $\theta_a$  reported for  $\text{ZnFe}_2\text{O}_4$  (+110 K and 0 K) by O'keeffe<sup>2</sup> and O'les<sup>4</sup> indicated very weak  $\text{Fe}^{3+}$ - $\text{Fe}^{3+}$  interaction, while in

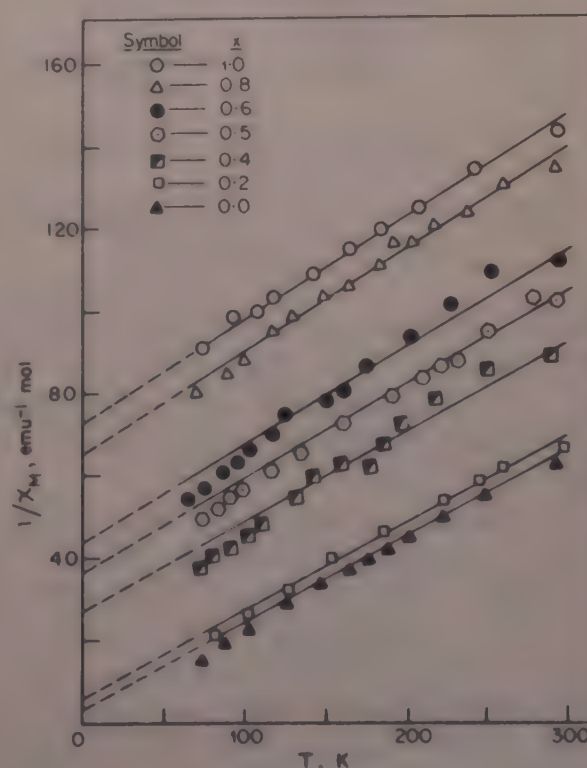


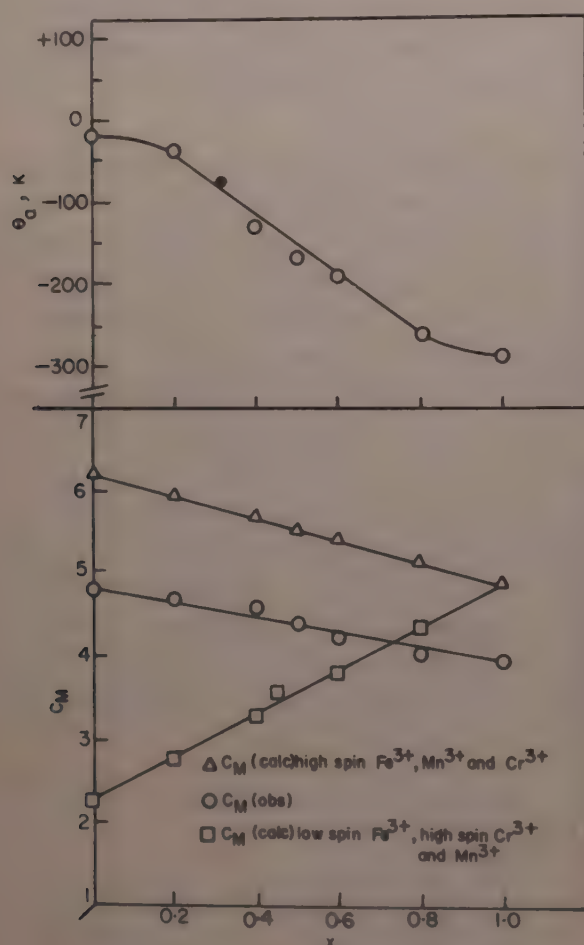
Fig. 1— $1/\chi_M$  versus  $T$



Table 1— $C_M$  (obs.),  $C_M$  (calc.),  $\mu_{\text{eff}}$  and  $\theta_a$  Values for the System  $\text{ZnFe}_{1-x}\text{Mn}_x\text{CrO}_4$ 

$x$	$C_M$ , emu mol <sup>-1</sup> deg <sup>-1</sup>			$\theta_a$ K	$\mu_{\text{eff}}$ Bohr Magneton
	Obs.	Calc.*	Calc.**		
0.0	4.85	6.25	2.25	-20	6.25
0.2	4.71	5.98	2.78	-30	6.16
0.4	4.58	5.70	3.30	-125	6.08
0.5	4.43	5.56	3.56	-167	5.98
0.6	4.23	5.43	3.83	-187	5.84
0.8	4.00	5.15	4.35	-260	5.68
1.0	3.94	4.88	4.88	-287	5.64

 \* Assuming  $\text{Fe}^{3+}$ ,  $\text{Mn}^{3+}$  and  $\text{Cr}^{3+}$  in high spin states

 \*\* Assuming  $\text{Fe}^{3+}$  in low spin and  $\text{Cr}^{3+}$ ,  $\text{Mn}^{3+}$  in high spin states

 Fig. 2—Variation of  $\theta_a$ ,  $C_M$  (obs. and calc.) with composition of the ferrite

the case of  $\text{ZnMn}_2\text{O}_4$  and  $\text{ZnCr}_2\text{O}_4$  in which high negative values of  $\theta_a$  were observed, various workers<sup>1,2,4,9</sup> suggested that very strong antiferromagnetic interactions are present between  $\text{Cr}^{3+}$ - $\text{Cr}^{3+}$  and  $\text{Mn}^{3+}$ - $\text{Mn}^{3+}$  ions.

In our present investigation, the possible interactions at B-site are as follows: (1)  $\text{Fe}^{3+}$ - $\text{Fe}^{3+}$ , (2)  $\text{Fe}^{3+}$ - $\text{Mn}^{3+}$ , (3)  $\text{Fe}^{3+}$ - $\text{Cr}^{3+}$ , (4)  $\text{Cr}^{3+}$ - $\text{Cr}^{3+}$ , (5)  $\text{Mn}^{3+}$ - $\text{Cr}^{3+}$ , and (6)  $\text{Mn}^{3+}$ - $\text{Mn}^{3+}$ . Out of these,  $\text{Fe}^{3+}$ - $\text{Fe}^{3+}$  and  $\text{Fe}^{3+}$ - $\text{Mn}^{3+}$  interactions are very weak<sup>1,3</sup> while  $\text{Fe}^{3+}$ - $\text{Cr}^{3+}$ ,  $\text{Cr}^{3+}$ - $\text{Cr}^{3+}$ ,  $\text{Mn}^{3+}$ - $\text{Mn}^{3+}$  and  $\text{Mn}^{3+}$ - $\text{Cr}^{3+}$  interactions are strong and antiferromagnetic<sup>1,4</sup>. Further it is observed (Table 1

and Fig. 2) that  $\theta_a$  values increase with increase in concentration of  $\text{Fe}^{3+}$  ions at B-site. This is attributed to the fact that as  $\text{Mn}^{3+}$  ion at B-site is gradually replaced by  $\text{Fe}^{3+}$  ion, the empty  $e_g(d_{x^2-y^2})$  orbital of  $\text{Mn}^{3+}$  ( $3d^4$ ) ion is gradually filled and it leads to less overlapping of  $e_g$  orbitals in X-y direction. Therefore, metal-metal interactions at B-site are reduced. Similar trend has been observed by Blasse<sup>1</sup> and O'les<sup>4</sup> in the systems  $\text{ZnFe}_{2-x}\text{Mn}_x\text{O}_4$  and  $\text{ZnFe}_{2-x}\text{Cr}_x\text{O}_4$  respectively.

We have also stated that interactions can also take place via intervening oxygen ion (superexchange). Since in the system investigated, the tetrahedral sites are occupied by  $\text{Zn}^{2+}$  ion,  $90^\circ$  B-O-B interactions become significant<sup>9,10</sup>. A-O-A superexchange interaction is ruled out in this system since both angle and interatomic distance remain unfavourable.

In the case of  $\text{ZnFeCrO}_4$  compound, three possible superexchange (M-O-M) models, viz.  $\text{Fe}^{3+}$ -O- $\text{Fe}^{3+}$ ,  $\text{Cr}^{3+}$ -O- $\text{Cr}^{3+}$  and  $\text{Fe}^{3+}$ -O- $\text{Cr}^{3+}$  are possible, while in  $\text{ZnMnCrO}_4$  there are  $\text{Mn}^{3+}$ -O- $\text{Mn}^{3+}$ ,  $\text{Cr}^{3+}$ -O- $\text{Cr}^{3+}$  and  $\text{Mn}^{3+}$ -O- $\text{Cr}^{3+}$  interactions. In order to explain the increase in  $\theta_a$  values with increasing  $\text{Fe}^{3+}$  ion concentration, we have not taken into consideration  $\text{Cr}^{3+}$ -O- $\text{Cr}^{3+}$  interaction since  $\text{Cr}^{3+}$  concentration at B-site is constant throughout the system. In  $\text{ZnMnCrO}_4$  compound, when two  $\text{Mn}^{3+}$  ions are present on either side of oxygen ion, the outer electronic cloud of the cations would approach closer due to the smaller distance between them as compared to other models. Therefore, more overlap of  $e_g$  orbitals and more antiferromagnetic interaction take place. Thus, in this case,  $\text{Mn}^{3+}$ -O- $\text{Mn}^{3+}$  superexchange is more predominant than  $\text{Mn}^{3+}$ -O- $\text{Cr}^{3+}$ . As the concentration of  $\text{Fe}^{3+}$  ion is increased, the overlapping of  $e_g$  orbitals would decrease since  $\text{Fe}^{3+}$  ion has less ionic radius than  $\text{Mn}^{3+}$  ion (Ref. 11) and hence less antiferromagnetic interaction will take place. This is also one of the reasons for our increase in the  $\theta_a$  value with increase in  $\text{Fe}^{3+}$  ion concentration at B-site.

It is observed from Table 1 and Fig. 1 that  $C_M$  values increase with increase in  $\text{Fe}^{3+}$  ion in the lattice, which is attributed to the increasing magnetic moment per ion. Low values of  $C_M$  obtained by us from paramagnetic susceptibility can arise as a consequence of A-B interactions which occur if a very small fraction of  $\text{Fe}^{3+}$  ions occupy A-site. During firing process, if some  $\text{ZnO}$  is lost (being more volatile), then the other possible cation like  $\text{Fe}^{3+}$  may go to A-site in very small quantity. This is due to the fact that  $\text{Fe}^{3+}$  ion has a tetrahedral site preference energy<sup>12</sup> which is next to  $\text{Zn}^{2+}$  ion in the lattice.  $\text{Fe}^{3+}$  ion at A-site will form clusters with twelve nearest B-site cations and this will lead to much stronger A-B interaction than B-B interaction. Therefore, in the system



$\text{ZnFe}_{1-x}\text{Mn}_x\text{CrO}_4$ , these cluster formations may be responsible for the lowering of  $C_M$  values. At low temperatures (below 90 K), there is a small deviation observed in the plots of  $1/\chi_M$  versus  $T$ , indicating ferrimagnetic behaviour for  $x \leq 0.6$ . Such a behaviour indicates that in the compounds studied, the formation of clusters may be taking place. Similar low values of  $C_M$  due to clusters have been observed by Geller *et al.*<sup>13</sup> and Lotgering<sup>3</sup> for garnets and  $\text{ZnFe}_2\text{O}_4$  compounds respectively.

All the above discussion on direct interactions and superexchange interactions results in decrease in  $\theta_a$  values with increasing  $\text{Fe}^{3+}$  ion concentration. Similarly, lower values of  $C_M$  are attributed to the cluster formation. It is observed from Fig. 2 that the decreasing trend of our  $C_M$  values agrees closely with those of  $C_M$  values calculated assuming  $\text{Fe}^{3+}$ ,  $\text{Cr}^{3+}$  and  $\text{Mn}^{3+}$  in high spin states only. However, a reverse trend (increase in  $C_M$  values) is observed when  $\text{Fe}^{3+}$  is taken in low spin and  $\text{Cr}^{3+}$ ,  $\text{Mn}^{3+}$  in high spin states (Fig. 2). The low spin state of  $\text{Mn}^{3+}$  ion is also ruled out since it acts as Jahn-Teller ion (Ref. 6). Our Mössbauer effect studies<sup>7</sup> also suggest that  $\text{Fe}^{3+}$  ion is present in high spin state only. The above discussion on magnetic properties suggests that the ionic configuration for the system investigated is  $\text{Zn}^{2+}[\text{Fe}_{1-x}^{3+}\text{Mn}_x^{3+}\text{Cr}^{3+}]\text{O}_4^{2-}$ .

One of the authors (PSJ) is thankful to the CSIR, New Delhi for the award of a Senior Research Fellowship, and the other (VSD) to the UGC, New Delhi for financial support.

## References

- 1 Blasse G, *Philips Res Rep (Netherlands)*, **20** (1965) 528.
- 2 O'keefe M, *J Phys & Chem Solids (GB)*, **21** (1961) 172.
- 3 Lotgering F K, *J Phys & Chem Solids (GB)*, **27** (1966) 139.
- 4 O'les A, *Phys Status-Solidi a (Germany)*, **3** (1970) 569.
- 5 Baltzer P K & Lopatin E, *Proceedings of the International Conference on Magnetism, held at Nottingham, Sept 1964* (The Institute of Physics & Physical Society, London), 1964, 564.
- 6 Jain P S & Darshane V S, *Indian J Chem A*, **19** (1980) 1050.
- 7 Darshane V S, Jain P S & Umadikar P H, *Indian J Chem A*, **20** (1981) 495.
- 8 Goodenough J B, *Magnetism and chemical bond* (John Wiley, New York), 1966.
- 9 McGuire T R, Howard L N & Smart J S, *Ceramic Age (USA)*, **60** (1952) 22.
- 10 Suseela, S & Sinha A P B, *Indian J Pure & Appl Phys.* **11** (1973) 116.
- 11 *Handbook of chemistry*, compiled and edited by N A Lange (McGraw-Hill, New York), 1967.
- 12 Miller A, *J Appl Phys (USA)*, **30** (Suppl) (1959), 245.
- 13 Geller S, Williams H J, Espinose G & Sherwood R C, *Bell Syst Tech J (USA)*, **43** (1964) 565.



## Structure of $\text{As}_2\text{S}_3$ Glass†

A K NANDI & B MUKHERJEE\*

Central Glass & Ceramic Research Institute, Jadavpur, Calcutta  
700 032

Received 20 January 1982; revised received 27 April 1983

The radial distribution function of  $\text{As}_2\text{S}_3$  glass has been determined from X-ray diffraction experiment. The first neighbour interatomic distances have been found increasing with the increase of randomness of the structure. When the structures according to covalent chain model and random covalent model are compared the loss of crystallinity character of the structure has been found to introduce randomness in the structure of the molecule.

Sulphur and arsenic, having electronic configurations  $3s^23p^4$  and  $4s^24p^3$  respectively, while combining to form an amorphous material, will assume either a layered or polymeric chain-like structure with cross linkage between adjacent chains. The energy of formation of electron pairs in the polymers depending on the amount of overlaps of orbitals can be correlated to the forbidden energy band gap<sup>1</sup>. The present study on  $\text{As}_2\text{S}_3$  glass has been undertaken to provide structural information for the substance to explain the electrical conductivity results.

A large number of research papers have been published on structural studies of amorphous semiconductors where the scattering has been recorded either by X-ray, neutron<sup>2</sup> or electron<sup>3</sup> diffraction techniques. The authors have employed the first technique to characterize the material and found a marked variation in the two samples, as evidenced from the X-ray diffraction patterns, although in principle the method of preparation, described elsewhere<sup>4</sup> remains the same.

**Theory**—In the absence of any regular lattice representation in the solid, the scattering of X-rays from the solid will appear as one or more diffuse bands. We assume a radial distribution function (rdf) responsible for such scattering. We define rdf such that  $4\pi r^2 \rho(r)$  is the most probable number of atoms within the volume of the sphere lying between  $r$  and  $r + dr$  from the centre of an atom. The function is represented as

$$4\pi r^2 \rho(r) = 4\pi r^2 \rho_0 + \frac{2r}{\pi} \int_0^\infty S(s) \sin rs \, ds \quad \dots (1)$$

where  $S(s) = (I_{\text{obs}} - \sum f^2) / \sum f^2$ ,  $\rho_0 = \text{atom } \text{\AA}^{-3}$

† This paper was presented at the 9th National Conference on Crystallography held at Sardar Patel University, Vallabh Vidyanagar, Feb. 1978.

**Experimental procedure**—Though the two samples (1 and 2) have the same chemical formulae and apparently look alike, when subjected to X-ray diffraction experiment, the characteristic patterns of one differ from that of the other. A very thin section of 0.2 mm thickness mixed with collodion is mounted on the tip of a glass rod. X-ray photographs of the samples are taken with a Debye-Scherrer camera of radius 5.73 cm placed in an environment evacuated to about  $10^{-2}$  mm of Hg, using  $\text{Cu-K}_\alpha$  (filtered) radiation with 48 hr exposure. The intensity pattern is recorded with Karl Zeiss microphotometer GIII and is computed with the help of a calibration strip<sup>5</sup>. An accurate position of angular distribution is determined with a reference fiducial knife mark. A separate experiment is performed with  $\text{Mo-K}_\alpha$  radiation with powder diffractometer and the intensity patterns thus obtained are brought to the same scale and thereby the termination error is minimized. Usual polarization correction is applied. The corrected intensities in an arbitrary unit are brought to the absolute scale (e.u.) by matching  $\sum f_m^2$  over an angular range  $0.9040 \leq \sin \theta/\lambda \leq 0.9770$ , using locally developed program<sup>6</sup>. Corrected intensity distribution curve in absolute scale for the sample 2 is given in Fig. 1.

The radial distribution function has been calculated from the corrected intensities (e.u) according to Eq. (1) using the program<sup>6</sup>. The damping factor used in these cases is  $0.001 \text{ \AA}^2$ . The rdf in one case (sample 2) is shown in Fig. 2. The rdf shows a small peak at  $r = 0.8 \text{ \AA}$ . The legitimate peak cannot occur at  $r$ 's smaller than the sum of the smallest pair of atomic radii involved. This peak is therefore assigned as spurious. There may also appear peaks on the negative side of  $\sum 4\pi r^2 \rho_0$  in rdf due to the inaccuracy in intensity measurements. The rdf maxima will fall in correct interatomic distances provided the intensity measurements are correct. However, in the present investigation much care has been taken to ensure

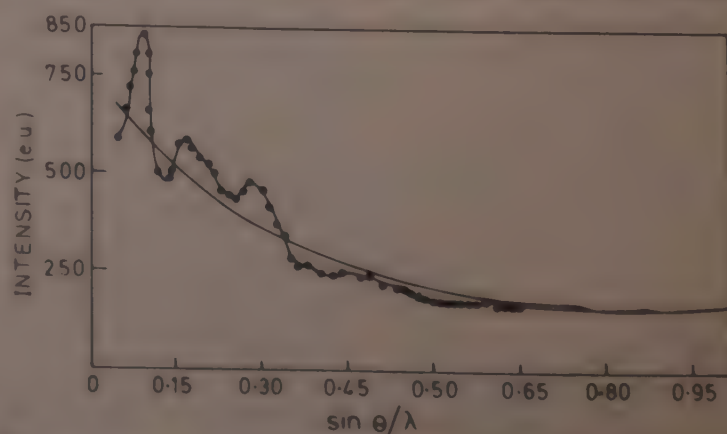


Fig. 1 Corrected intensity (e.u.) against  $\sin \theta/\lambda$  for the sample 2



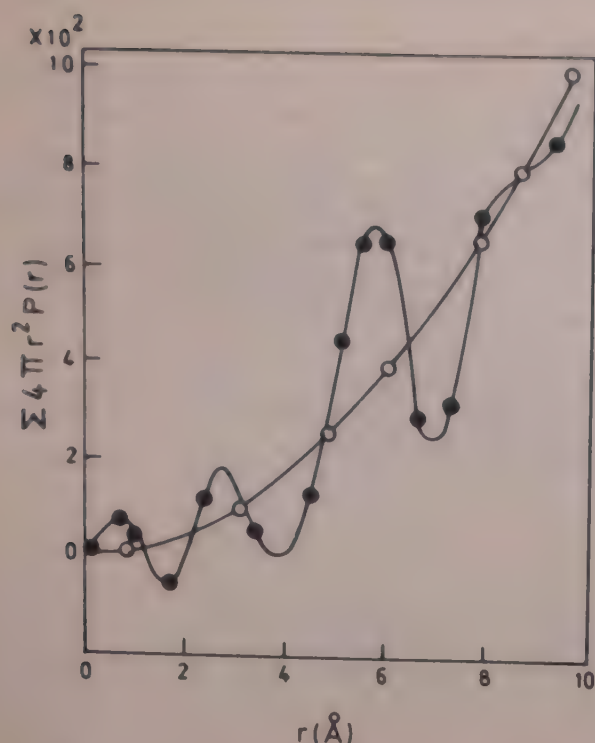


Fig. 2— $\sum 4\pi r^2 \rho(r)$  against  $r(\text{\AA})$  for sample 2

correct angular representation of the intensity distribution. The positions,  $r_i$  of the maxima of the peaks in the rdf are given in Table 1. The  $r_i$  value is slightly on the larger side of the As-S interatomic distance, this is more predominant in the case of sample 2. The area under the first peak in the rdf is a measure of the number of nearest neighbours about the atom, i.e. the coordination number. It follows that

$$\eta_A = (c_1 K_1 \eta_{11} + c_2 K_1^2 \eta_{12} + c_1 K_1 K_2 \eta_{12} + c_2 K_1 K_2 \eta_{21}) / (\sum c_i K_i)^2$$

where  $c_i$ s are the concentration of  $i$ th component. Values of the average coordination number ( $\eta_A$ ) are given in Table 1. In order to evaluate  $\eta_A$  from peak area, the value of the average atomic density of the substance must be known. The value of  $\rho_0$  has been taken as the reciprocal of the average crystalline atom volume  $V_0$  of As and S. Because of the uncertainties in  $\rho_0$  an error in the value of  $\eta_A$  is obvious. The error may extend up to 20%.

**Discussion**—We consider here chain-crossing model (CCM) in which sulphur chain structure is maintained. The three-fold coordination of As acts as chain-crossing points. On this model, As is not assumed to form bond with another As. It is assumed that

$$\eta_{As-As} = 0; \eta_{S-S} + \eta_{S-As} = 2; \eta_{As-S} = 3$$

where  $\eta_i$  is the number of neighbours, irrespective of their kind about an atom of type  $i$ . Obviously, the condition  $c_1 \eta_{12} = c_2 \eta_{21}$  also holds. With this assumption it follows from that

$$\eta_A(\text{CCM}) = \frac{K_s^2(2 - 5c_{As}) + 6c_{As}K_{As}K_s}{\sum c_i K_i^2}$$

Table 1—Positions of the Peaks in rdf and Values of  $\eta_A$

Sample No.	Interatomic distance ( $\text{\AA}$ )		$\eta_A$			$\rho_0(\text{atom}/\text{\AA}^3)$
	$r_1$	$r_2$	Obs.	CCM	RCM	
1	2.65	4.65	2.26	2.22	2.95	0.0416
2	2.75	5.80	2.49			

The value of  $\eta_A$  obtained is 2.22 which is found fairly in good agreement with  $\eta_{\text{obs}}$  of the experimental value for sample 1. In random covalent model (RCM) we assume that

$$\eta_{As} = 3 = \eta_{As-As} + \eta_{As-S}; \eta_S = 2 = \eta_{S-S} + \eta_{S-As}$$

The value of  $\eta_A$  calculated in this model using the expression

$$\eta_A^{\text{RCM}} = \frac{9c_{As}^2 K_{As}^2 + 4c_S K_S^2 + 12c_S c_{As} K_{As} K_S}{(3c_{As} + 2c_S)(\sum c_i K_i^2)}$$

is found not in agreement with that obtained experimentally.

In both the models we assume that all nearest neighbours in pairs such as S-S, As-As and As-S contribute to the first peak of rdf according to the condition laid above. From the above findings it can be concluded that due to the loss of crystallinity character which is apparent from X-ray pattern, the randomness in the structure is introduced. But in the present case, the experimentally determined coordination number ( $\eta_A$ ) in both the cases does not agree with that evaluated theoretically for RCM model. Since the deviation of the experimental value of  $\eta_A$  is comparatively much less than  $\eta_A(\text{CCM})$  the structure may be conceived as maintaining the chain-like structure of sulphur although the possibility of disruption at several points cannot be ruled out. Electrical conductivity measurements of both the samples, 1 and 2, were done<sup>7</sup> which, when fitted to Mott's model, show a marked difference in the activation energy for conduction in the two samples. The activation energy for conduction of the sample 1 (referred to as A in Ref. 7) agrees quite well with that reported earlier, whereas that in the case of sample 2 (referred to in Ref. 7 as B) does not fit well with the reported values. This clearly indicates that although both the samples have the same stoichiometric ratio, there exists inhomogeneity to a great extent in sample 2. The prediction that the present authors made from X-ray data corroborates the results<sup>7</sup> of the electrical conductivity measurements. The second peak may be due to partial association of S-chain giving rise to second neighbours. No attempt has been made for a quantitative estimation of the number



of second neighbours around the atoms as the nature of this association is not a priori clear.

The authors' thanks are due to the Director, Central Glass and Ceramic Research Institute for his kind permission to publish this paper. Thanks are due to Dr K P Srivastava of this Institute for providing the materials for the present study. The authors are indebted to Dr R K Sen of the Indian Association for the Cultivation of Science, Calcutta, for helpful discussion.

## References

- 1 Tarasov V V, *New problems in physics of glass: IPST Catalogue* 804, translated from Russian (Israel Program of Science Translations Ltd, Jerusalem), 1963, 179.
- 2 Cargill III G S, *Solid State Phys (USA)*, **30** (1975) 228.
- 3 Fawcett R W, Wagner C N J & Cargill III G S, *J Non-Crystalline Solids (Netherlands)*, **8-10** (1972) 369.
- 4 Glaze F W, Blackman D H, Osmalov J S et al., *J Res Natl Bur Stand (USA)*, **59** (1957) 83.
- 5 Robinson B W, *J Sci Instrum (GB)*, **10** (1933) 233.
- 6 Nandi A K, unpublished work.
- 7 Dutta M, Banerjee P N, Bhattacharya D L, et al., *Indian J Pure & Appl Phys*, **18** (1980) 568.



## Dependence of Mechanoluminescence on the Area of Newly Created Surfaces of Crystals

B P CHANDRA\*, T R CHANDRAKER &  
S V DESHPANDE

Department of Physics, Government Science College  
Raipur 492 002

Received 24 June 1982

A linear relation is found between the total mechanoluminescence intensity and the area of newly created surfaces of the crystals. It is shown that this finding may be of considerable importance in the theoretical and experimental investigation of mechanoluminescence.

Mechanoluminescence (ML), the luminescence produced during mechanical deformation of solids can be excited either by grinding, rubbing, cutting, cleaving, impact crushing or by compressing the solids. Many techniques have been devised for the studies of ML under controlled deformations. The ML can also be excited by thermal shock caused by drastic cooling or heating. On the basis of the mechanism of excitation, the ML may be classified into different types, for example, piezo-induced ML, cleavage-induced ML, dislocation-induced ML, tribo-induced ML, chemi-induced ML, adsorption-induced ML, and transition induced ML. During the theoretical and experimental investigation of ML, many workers have assumed that the ML is related to the area of newly created surfaces of the solids<sup>1-4</sup>. The present note gives a direct evidence that the ML intensity is directly related to the area of the newly created surfaces of crystals.

The crystals of sucrose, uranyl nitrate hexahydrate, triglycine sulphate and potassium dihydrogen phosphate were grown from slow evaporation of their aqueous solutions. The crystals of phenanthrene were grown from the melt using the Bridgman technique. The crystals were made to the required size by grinding and polishing. The size of all the crystals used for compression experiment was  $5 \times 5 \times 5 \text{ mm}^3$ . However, the crystals used in cutting experiment were of one mm thickness. For the ML measurements, the crystal was fractured instantaneously by compressing it between the two jaws of a screw gauge. In an independent experiment, the crystals were cut instantaneously by a sharp blade. The ML intensity was monitored by the technique described previously<sup>5</sup>. In the cutting experiment, area of newly created surfaces was calculated from the known dimension of the crystals.

However, in the compression experiment, the area of newly created surfaces, ( $S$ ) was determined from the relation:

$$S = \left[ N_1 \left( \frac{M_1}{d} \right)^{2/3} + N_2 \left( \frac{M_2}{d} \right)^{2/3} + N_3 \left( \frac{M_3}{d} \right)^{2/3} + N_4 \left( \frac{M_4}{d} \right)^{2/3} + \dots \right] - S_0 \quad \dots (1)$$

where  $d$  is density of the crystal and  $S_0$  is surface area of the crystal before the fracture. The crystallites formed after the fracture were divided into four groups.  $M_1$ ,  $M_2$ ,  $M_3$  and  $M_4$  denote the average mass of the crystallites of first, second, third, and fourth group respectively.  $N_1$ ,  $N_2$ ,  $N_3$ , and  $N_4$  denote the total number of crystallites of the first, second, third, and fourth group respectively. The area created due to the formation of some fine powder was neglected.

Fig. 1 shows that the total ML intensity, measured in terms of the deflection of the ballistic galvanometer is directly proportional to the area of newly created surfaces. Fig. 1 also indicates that the ML efficiency, that is, the ML intensity produced during the creation of unit area is different for the different crystals. The ML spectra of sucrose, triglycine sulphate and potassium dihydrogen phosphate crystals are similar to the spectra of the emission from the second positive group of molecular nitrogen<sup>1</sup>. The ML spectra of uranyl nitrate hexahydrate consist of the photoluminescence emission and the nitrogen emission<sup>1,6</sup>.

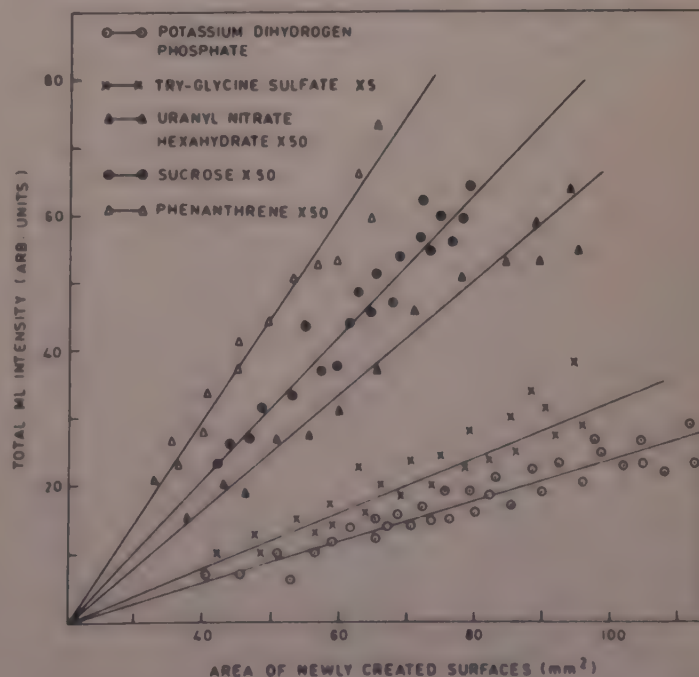


Fig. 1—Dependence of total ML intensity on the area of newly created surfaces of the crystals



The ML spectra of phenanthrene crystals are similar to their photoluminescence spectra<sup>7</sup>.

The linear dependence of ML intensity on the area of newly created surfaces suggests that the atoms or molecules present on the newly created surfaces only are responsible for the ML excitation because they are subjected to strong deformation during the movement of cracks in the crystals. The results of the present investigation may be of considerable importance in the further theoretical and experimental investigation of ML. If the output of the photomultiplier tube could be calibrated in terms of the number of photons, then the present investigation may help in determining the number of ruptured bonds required for the emission of a single photon.

The authors are thankful to the Principal, Dr P R Khandekar for providing the experimental facilities. Two of the authors (TRC and SVD) are thankful to the Vice-chancellor, Ravishankar University, Raipur, for financial assistance.

#### References

- 1 Chandra B P, *Phys Status Solidi (a) (Germany)*, **64** (1981) 395.
- 2 Meyer K, Obrikat D & Rossberg M, *Kristal Und Tech (Germany)*, **5** (1970) 5; **5** (1970) 181.
- 3 Zink J I, *Acc Chem Res (USA)*, **11** (1978) 289.
- 4 Walton A J, *Adv Phys (GB)*, **26** (1977) 1887.
- 5 Chandra B P & Elyas M, *Indian J Pure & Appl Phys*, **15** (1977) 744.
- 6 Zink J I, *Inorg Chem (USA)*, **14** (1976) 555.
- 7 Chandra B P, Elyas M & Deshmukh N G, *Indian J Pure & Appl Phys* **20** (1982) 210.



## Lattice Waves in bcc Transition Metals

K C GUPTA† & R P S RATHORE\*

Department of Physics, R B S College, Agra 282 002

Received 30 July 1982; revised received 17 December 1982

The nine-parameter shell model of B L Fielek [*J Phys FGB*], 10 (1980) 1665] for bcc transition metals was modified by us in an earlier study [*Indian J Pure & Appl Phys*, 20(1982), 851] by including a new, more consistent equilibrium condition based on a semistatistical approach. This modified model was found to predict the phonon dispersion curves for chromium quite successfully. The same modified model has been applied to analyze the lattice spectra of some other bcc transition metals, viz. V,  $\alpha$ -Fe, Nb, Mo, Ta and W to test its efficacy further. It is shown that the overall fit of the experimental curves in the case of  $\alpha$ -Fe, Mo, Ta and W is definitely improved and out of many characteristic anomalies present in Mo and Nb, some are successfully predicted. The source of the anomalies is also discussed.

A transition metal consists of cores,  $d$ -electrons and nearly-free conduction electrons. The  $d$ -electrons, which are neither rigidly bound to nucleus nor are nearly-free like conduction electrons, introduce peculiar changes and anomalies in the phonon dispersion curves of the transition metals. Fielek<sup>1</sup> has recently reported a nine parameter model for bcc transition metals taking into account all possible interactions among its various entities and predicted the phonon spectrum of Nb with many characteristic anomalies explained. This model, found to be deficient in considering the crystal equilibrium explicitly, was modified by us<sup>2</sup> by including a more consistent equilibrium condition based on a semistatistical

procedure due to Alonso and Santos<sup>3</sup>. Our modified model was found to predict the phonon dispersion curves for chromium successfully. The present note reports the results obtained by applying the modified model to compute the lattice waves in other bcc transition metals, viz. V and  $\alpha$ -Fe (3d-series), Nb and Mo (4d-series) and Ta and W (5d-series) for predicting the various observed anomalies.

The necessary elastic relations, dispersion relations and zone boundary frequency relations are taken as such and the phonon dispersion curves for the metals under study computed. The input data and computed force constants are listed in Table 1. Fig. 1 represents the theoretical dispersion curves obtained in the present study. The experimental points for V,  $\alpha$ -Fe, Nb, Mo, Ta and W due to Collela and Batterman<sup>4</sup>, Minkiewics *et al.*<sup>5</sup>, Powell *et al.*<sup>6</sup>, Woods<sup>7</sup>, and Larose and Brockhouse<sup>8</sup>, respectively are also shown alongside the corresponding curves, for comparison. It can be easily seen that invariably in all the cases, an impressive fit of the phonon dispersion curves is obtained. Not only all the important features of the curves in three major symmetry directions are revealed but some of the observed anomalies are also predicted. A comparison of the present study with other similar recent studies<sup>1,9-12</sup> indicate that (i) our results for W are better than those of Jani and Gohel<sup>12</sup> who have claimed their predictions as best obtained so far. The points of superiority of our predictions are (a) no errors present at zone boundaries of all the L-modes (b) L and T modes along [100] and [110] directions are better reproduced and L-mode along [110] also does not bear any maxima resembling the experimental curves; (ii) there is a definite improve-

† Department of Physics, C L Jain College, Firozabad 283 203

Table 1—Input Data and Computed Model Parameters for V,  $\alpha$ -Fe, Nb, Mo, Ta and W

Input data and computed model parameters	V	$\alpha$ -Fe	Nb	Mo	Ta	W
$C_{11}(10^{12}\text{dyn/cm}^2)$	2.280	2.3310	2.460	4.4077	2.609	5.3255
$C_{12}(10^{12}\text{dyn/cm}^2)$	1.188	1.3544	1.340	1.7243	1.574	2.0495
$C_{44}(10^{12}\text{dyn/cm}^2)$	0.426	1.1783	0.2870	1.2165	0.818	1.6273
$\alpha(10^{-8}\text{cm})$	3.08	2.86	3.3008	3.14	3.3	3.16
$m(10^{-24}\text{g})$	84.5637	92.7060	154.2240	159.2604	300.377	305.191
$\nu_{L(100)}(10^{12}\text{Hz})$	—	—	6.49	5.52	5.03	5.5
$\nu_{L(110)}(10^{12}\text{Hz})$	—	—	—	8.14	—	6.8
$\nu_{T_1(110)}(10^{12}\text{Hz})$	4.6	4.55	—	—	2.63	—
$\nu_{T_2(110)}(10^{12}\text{Hz})$	5.5	6.49	3.93	—	—	—
$\alpha_1(10^4\text{dyn/cm}^2)$	-0.1034	-0.1192	-0.08970	-0.09945	-0.0998	-0.09820
$\beta_1(10^4\text{dyn/cm})$	5.0107	8.2643	8.62814	24.5169	8.9076	-7.7165
$S_1(10^4\text{dyn/cm})$	-2.7325	-2.9710	-6.93805	-18.4888	-4.6789	15.7719
$S_2(10^4\text{dyn/cm})$	1.8824	1.6349	2.02784	4.41185	1.8874	5.3725
$K(10^4\text{dyn/cm})$	-21.4036	-28.0221	-40.84708	913.5665	-49.1102	1209.8725
$A(10^4\text{dyn/cm})$	0.9667	0.0134	1.55848	0.59833	1.0678	0.45487



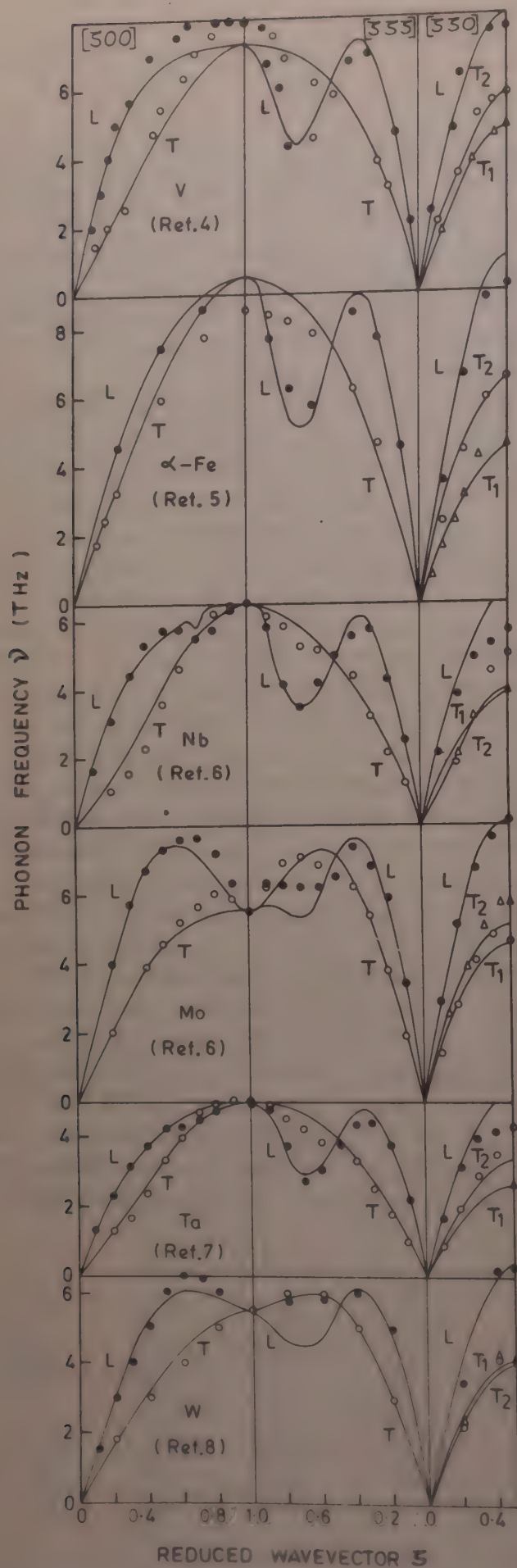


Fig. 1 Dispersion curves for V,  $\alpha$ -Fe, Nb, Mo, Ta and W along the three major symmetric directions. Continuous lines represent the theoretical curves obtained in the present study, and  $\circ$  represent experimental points [Refs. 4-8].

ment in r.m.s. fit in case of  $\alpha$ -Fe, Mo and Ta; and (iii) The results for V and Nb are found to be approximately of the same order.

The anomalies covered by our model in the case of Mo is the unusual small dip along [111] direction in L-mode at  $\xi=0.7$ , not reported by previous workers<sup>9,13</sup>. In the case of Nb, the crossing of two T-branches in [110] direction along with the softening of  $T_2$  branch around  $\xi=0.3$ , and softening of T-branch around  $\xi=0.3$  along [100] direction are clearly predicted. We also obtained a small dip in L-mode at  $\xi=0.7$  along [100] direction but it is not so pronounced so as to get crossing of L and T branches. This may be attributed to the fact that our volume interaction scheme due to Das *et al.*<sup>14</sup> does not include the Umklapp processes. It can also be mentioned here that Fielek also could obtain this crossing only after recourse to an extensive fitting process.

The causes of the anomalies present in the dispersion curves specially in the case of Mo and Nb have been pointed out by many group of workers. According to Chui<sup>15</sup> and Varma and Weber<sup>16</sup>, the presence of saddle points in the electronic band structure near the Fermi surface introduces the anomalous behaviour, while according to Cooke *et al.*<sup>17</sup>, Gupta and Freeman<sup>18</sup> and Klein *et al.*<sup>19</sup>, Fermi surface geometry is responsible for it. Recently, Varma and Weber<sup>20</sup> have been able to predict approximately all the anomalies in Mo and Nb and have concluded that these cannot arise from short-range force constants which are governed by second order elastic constants. In their analysis the dynamical matrix due to perturbation consists of two parts  $D^{(1)}$  and  $D^{(2)}$  which are produced due to the first- and second-order corrections, to electronic energies in the bands near Fermi surface energy, and arise from second- and first-order displacements respectively. They found that the anomalous features are produced as a result of interband scattering in  $D^{(2)}$  near Fermi surface energy. Fielek<sup>1</sup> has emphasized that the shell concept, i.e. a dipole model is a useful phenomenological concept for explaining lattice spectra and anomalous behaviour in bcc transition metals. After modifying the Fielek model<sup>1</sup> properly and analyzing it for many bcc transition metals, we find that Fielek could predict the characteristic anomalies along [100] and [111] directions in L and T branches in the case of Nb only and that too by using an extensive fitting procedure. Our modified model containing  $S_2$  term, said to be responsible for anomalies, could not reproduce the anomalies adequately in Nb and also in other metals. This led us to agree with the explanation of Varma and Weber<sup>20</sup>. Thus, we stress that in cases where anomalies are pronounced, long range forces such as van der Waal forces<sup>21</sup> are required to explain them and the use



of second-order elastic relations to compute the force constants of the model may not be useful as shown by Rao and Rajput<sup>22</sup>.

### References

- 1 Fielek B L, *J Phys F (GB)*, **10** (1980) 1665.
- 2 Gupta K C & Rathore R P S, *Indian J Pure & Appl Phys*, **20** (1982) 851.
- 3 Alonso J A & Santos E, *J Phys & Chem Solids (GB)*, **38** (1977) 307.
- 4 Colella R & Batterman B W, *Phys Rev B (USA)*, **1** (1970) 3913.
- 5 Minkiewics V J, Shrima G & Nathans R, *Phys Rev (USA)*, **162** (1967) 528.
- 6 Powell B M, Martil P & Woods A D S, *Can J Phys (Canada)*, **55** (1977) 160.
- 7 Woods A D B, *Phy Rev (USA)*, **136** (1964) 781.
- 8 Larose A & Brockhouse B N, *Can J Phys (Canada)*, **54** (1976) 1819.
- 9 Singh V P, Prakash J & Hemkar M P, *Nuovo Cimento B (Italy)*, **28** (1975) 476.
- 10 Khanna R N & Rathore R P S, *Indian J Pure & Appl Phys*, **19** (1980) 540.
- 11 Prakash J, Pathak L P & Hemkar M P, *Aust J Phys (Australia)*, **28** (1975) 57.
- 12 Jani A R & Gohel V B, *J Phys F (GB)*, **6** (1976) 125.
- 13 Behari J & Tripathi B B, *J Phys Soc Jpn (Japan)*, **33**(5) (1972), 1207.
- 14 Das S K, Roy D & Sengupta S, *Pramana (India)*, **8** (1977) 117.
- 15 Chui S T, *Phys Res B (USA)*, **9** (1974) 3300.
- 16 Varma C M & Weber W, *Phys Rev Lett (USA)*, **39** (1977) 1094.
- 17 Cooke J F, Davis H L & Mostoller M, *Phys Rev B (USA)*, **9** (1974) 2485.
- 18 Gupta M & Freeman A J, *Superconductivity in d- and f-band metal*, edited by D H Douglas (Plenum, New York), 1976, 313-339.
- 19 Klein B M, Papaconstantopoulos D & Boyer L L, *Superconductivity in d- and f-band metals*, edited by D H Douglas (Plenum, New York), 1976, 339-60.
- 20 Varma C M & Weber W, *Phys Rev B (USA)*, **19** (1979) 6142.
- 21 Mahanti J & Taylor R, *Phys Rev B (USA)*, **17** (1978) 554.
- 22 Rao R R & Rajput A, *Phys Status Solidi b (Germany)*, **106** (1981) 393.



## Hindered Rotation of the Terminal Group in a Schiff Base Mesogen HBT

JAI PRAKASH\*, B RAI† & RAHUL

Department of Physics, University of Gorakhpur, Gorakhpur  
273 001

Received 28 June 1982; revised received 8 February 1983

Dielectric constant and dielectric loss of five dilute solutions of N-(*p*-hexyloxybenzylidene)-*p*-toluidine have been determined at 21.93 GHz at different temperatures, using benzene as a non-polar solvent. Discontinuities around 37 and 46°C have been observed in the dielectric constant and dielectric relaxation time versus temperature curves. Ultrasonic velocity measurements also show discontinuities around 36 and 44°C. It has been suggested that the hindered rotation of the terminal group is probably responsible for these discontinuities.

Dielectric relaxation studies of mesogens have led to the understanding of properties of liquid crystals<sup>1-6</sup>. Study of polar molecules in dilute solutions of a nonpolar solvent gives valuable information. Dielectric absorption and dispersion of MBBA and EBBA in benzene solution have been recorded by Maurel and Price<sup>7</sup> and Arora and Agarwal<sup>8</sup>. This paper reports the dielectric relaxation studies of N-(*p*-hexyloxybenzylidene)-*p*-toluidine (HBT) in benzene. Discontinuities around 37 and 46°C have been observed in the dielectric constant and dielectric relaxation time versus temperature curves. Ultrasonic velocity measurements also show discontinuities around 36 and 44°C. It has been suggested that the hindered rotation of the terminal group is probably responsible for these discontinuities.

HBT (a Schiff base<sup>9,10</sup>) has been procured from M/s E Merck (Germany) and is used as such without further purification. A R grade benzene from M/s BDH (India) has been used after fractional distillation. Dilute solutions of HBT in benzene have been prepared just before the measurements. Dielectric constant ( $\epsilon'_{12}$ ) and dielectric loss ( $\epsilon''_{12}$ ) have been determined at 21.93 GHz following the standing wave method of Heston *et al.*<sup>11</sup> The experimental arrangements are essentially the same as described elsewhere<sup>12,13</sup>. Temperature has been controlled to within  $\pm 0.1^\circ\text{C}$  with the help of a VEB MLW (East Germany) model U 10 Ultrathermostat.  $\epsilon'_{12}$  and  $\epsilon''_{12}$ , presented in Table 1, have been measured with an accuracy of  $\pm 2\%$  and  $\pm 5\%$  respectively. A Belen (India) Model U1-751 ultrasonic interferometer

working at 2 MHz has been used for the measurement of ultrasonic velocity. The accuracy of ultrasonic velocity measurement has been found to be  $\pm 0.1\%$ .

It is apparent from Table 1 that  $\epsilon'_{12}$  shows a linear dependence on mole fraction ( $f_2$ ) for temperatures higher than 50°C whereas at lower temperatures a dip is observed in the range  $f_2 = 0.04-0.05$ . It is also apparent that  $\epsilon'_{12}$  does not decrease systematically with the increasing temperature; rather it is associated with discontinuities. A representative  $\epsilon'_{12}$  versus  $T$  curve, presented in Fig. 1, shows the discontinuities at 37 and 46°C.  $\epsilon'_{12}$  decreases with the increasing temperature as expected except in the temperature range 37-46°C. This behaviour may presumably be due to the hindered rotation of the terminal group attached to the HBT molecule. The contribution of the hindered group rotation starts appearing around 37°C. With the increasing temperature the terminal hindered group becomes more and more free to rotate which around 46°C shows its maximum contribution. No such consistent behaviour in  $\epsilon''_{12}$  has, however, been observed. Dielectric relaxation time of HBT in benzene solution has been evaluated following the single frequency method of Gopalakrishna<sup>14</sup>. It has been shown<sup>15</sup> that  $\epsilon'_{12}$  and  $\epsilon''_{12}$  are related through

$$\epsilon''_{12} = \epsilon_{\infty 12} + \frac{1}{\omega\tau_F} \epsilon'_{12} \quad \dots (1)$$

where  $\epsilon_{\infty 12}$  is the optical dielectric constant in solution,  $\omega$  is the angular frequency and  $\tau_F$  is the relaxation time. It is apparent from Eq. (1) that a straight line results when  $\epsilon'_{12}$  is plotted against  $\epsilon''_{12}$  and the slope gives the value of  $\tau_F$ . Evaluated values of  $\tau_F$  are found to be accurate within  $\pm 10\%$ .  $\tau_F$  as a function of temperature

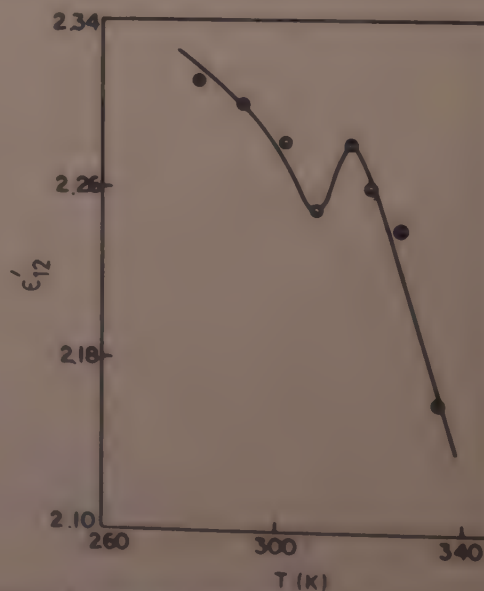


Fig. 1—Dielectric constant as a function of temperature of HBT in benzene for  $f_2 = 0.0104$

\* Present address: Department of Physics, St. Andrews College, Gorakhpur.



Table 1—Dielectric Constant and Dielectric Loss of HBT in Benzene Solution at Different Temperatures

[Frequency of measurement = 21.93 GHz]

Mole-fraction $f_2$	Temperature of measurement, K							
	283	293	303	310	318	323	330	338
0.0104 $\epsilon'_{12}$	2.31 <sub>0</sub>	2.29 <sub>5</sub>	2.28 <sub>0</sub>	2.25 <sub>0</sub>	2.28 <sub>0</sub>	2.25 <sub>0</sub>	2.23 <sub>6</sub>	2.15 <sub>9</sub>
$\epsilon''_{12}$	0.03 <sub>4</sub>	0.04 <sub>5</sub>	0.03 <sub>6</sub>	0.03 <sub>6</sub>	0.02 <sub>4</sub>	0.03 <sub>2</sub>	0.02 <sub>7</sub>	0.04 <sub>1</sub>
0.0325 $\epsilon'_{12}$	2.38 <sub>9</sub>	2.36 <sub>5</sub>	2.31 <sub>8</sub>	2.22 <sub>8</sub>	2.25 <sub>0</sub>	2.26 <sub>5</sub>	2.27 <sub>3</sub>	2.24 <sub>3</sub>
$\epsilon''_{12}$	0.04 <sub>0</sub>	0.04 <sub>9</sub>	0.05 <sub>2</sub>	0.05 <sub>8</sub>	0.05 <sub>4</sub>	0.05 <sub>1</sub>	0.04 <sub>9</sub>	0.06 <sub>1</sub>
0.0487 $\epsilon'_{12}$	2.37 <sub>3</sub>	2.34 <sub>1</sub>	2.31 <sub>8</sub>	2.25 <sub>0</sub>	2.30 <sub>2</sub>	2.29 <sub>5</sub>	2.29 <sub>5</sub>	2.30 <sub>2</sub>
$\epsilon''_{12}$	0.04 <sub>6</sub>	0.05 <sub>0</sub>	0.04 <sub>2</sub>	0.05 <sub>6</sub>	0.05 <sub>2</sub>	0.05 <sub>5</sub>	0.06 <sub>2</sub>	0.07 <sub>7</sub>
0.0652 $\epsilon'_{12}$	2.42 <sub>2</sub>	2.35 <sub>7</sub>	2.33 <sub>3</sub>	2.31 <sub>8</sub>	2.34 <sub>1</sub>	2.33 <sub>3</sub>	2.31 <sub>0</sub>	2.31 <sub>0</sub>
$\epsilon''_{12}$	0.04 <sub>7</sub>	0.05 <sub>7</sub>	0.06 <sub>7</sub>	0.06 <sub>4</sub>	0.05 <sub>4</sub>	0.06 <sub>4</sub>	0.06 <sub>9</sub>	0.08 <sub>0</sub>
0.0814 $\epsilon'_{12}$	2.43 <sub>9</sub>	2.40 <sub>5</sub>	2.38 <sub>9</sub>	2.34 <sub>9</sub>	2.40 <sub>5</sub>	2.36 <sub>5</sub>	2.35 <sub>7</sub>	2.33 <sub>3</sub>
$\epsilon''_{12}$	0.04 <sub>9</sub>	0.05 <sub>3</sub>	0.06 <sub>9</sub>	0.08 <sub>1</sub>	0.07 <sub>9</sub>	0.07 <sub>6</sub>	0.07 <sub>9</sub>	0.08 <sub>9</sub>

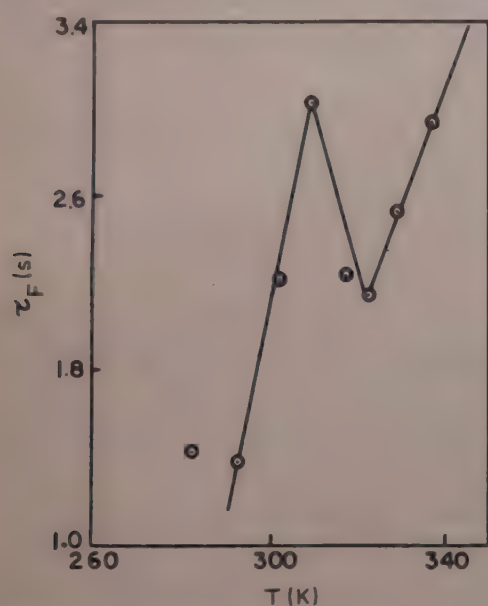
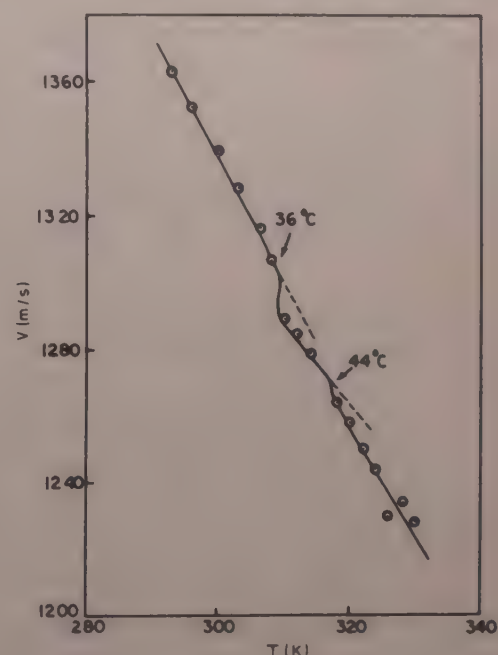


Fig. 2—Variation of the relaxation time with the temperature of HBT in benzene

is shown in Fig. 2. Similar to the behaviour of  $\epsilon'_{12}$  on  $T$ , discontinuities around 37 and 48°C have been observed in  $\tau_F$  versus  $T$  curve also (Fig. 2). It is apparent that  $\tau_F$  increases with increasing temperature except in the temperature range 37–48°C. Although the magnitude of change in  $\tau_F$  with increasing temperature is well within the limit of inaccuracy (e.g.  $\pm 10\%$ ), we consider it particularly because of its reproducibility. Similar conclusions have also been drawn in various runs of experimentation. A possible explanation of this behaviour of  $\tau_F$  on  $T$  may be due to the change of mesomeric moment<sup>16</sup>. The behaviour shown in Figs 1 and 2 may also be due to the hydrogen bonding. It is probable that at lower temperatures polymerization takes place. Consequently, the relaxation time will increase with increasing temperature. It is obvious, however, that no phase transition can occur in HBT in benzene solution as it does not form any lyotropic system. Thus, the only possible change which may occur is the conformational change in molecule/pair of molecules in the region 37–48°C. This conformational

Fig. 3—Ultrasonic velocity ( $v$ ) as a function of temperature of HBT in benzene

change may not be sudden but rather in an extended temperature range of  $\sim 10^\circ\text{C}$  to complete the whole transition.

It should be mentioned again for the sake of clarification, that the changes in the magnitudes of  $\epsilon'_{12}$  and  $\tau_F$  at different temperatures are well within the limits of experimental inaccuracies. However, due to their reproducibility and consistency we planned to substantiate the results through other measurements. Consequently, ultrasonic velocity of HBT in benzene solution at different temperatures (10–57°C) has also been measured. It is apparent from Fig. 3 that discontinuities around 36 and 44°C are present in the ultrasonic velocity versus temperature curve. Obviously, some internal rearrangement either in the form of a change in the mesomeric moment or a hydrogen bonding takes place which prevails in the temperature range 36–44°C. Ultrasonic velocity decreases regularly with the increasing temperature as



expected due to decrease in the density. Discontinuities observed in Fig. 3 support the findings of dielectric relaxation studies. However, the observed discontinuities and deviations can be better explained when similar measurements on other systems are carried out.

The authors are thankful to Prof. Nitish K Sanyal for providing the necessary facilities. Two of the authors (BR & Rahul) are thankful to the CSIR, New Delhi for financial assistance. Thanks are also due to Mr S R Shukla for the help during measurements.

## References

- 1 Gray G W, *Molecular structure and the properties of liquid crystals* (Academic Press, New York) 1962.
- 2 Agarwal V R & Price A H, *J Chem Soc Faraday Trans II (GB)*, **70** (1974) 188.
- 3 Parker J H & Carr E F, *J Chem Phys (USA)*, **55** (1971) 1846.
- 4 Gupta G K, Agarwal V K & Bahadur B, *J Chem Phys (USA)*, **71** (1979) 5290.
- 5 Rondalez F, Diguet D & Durand G, *Mol Cryst Liq Cryst (GB)*, **15** (1971) 183.
- 6 Kresse H, Selbmann Ch & Demus D, *Mol Cryst Liq Cryst (GB)*, **44** (1978) 179.
- 7 Maurel P & Price A H, *J Chem Soc Faraday Trans II (GB)*, **69** (1973) 1486.
- 8 Arora V P & Agarwal V K, *J Phys Soc Jpn (Japan)*, **42** (1977) 908.
- 9 Sarna R K, Bahadur B & Bhide V G, *Mol Cryst Liq Cryst (GB)*, **51** (1979) 117.
- 10 Bahadur B, *J Chem Phys (USA)*, **67** (1977) 3272.
- 11 Heston W M (Jr), Franklin A D, Hennelly E J & Smyth C P, *J Am Chem Soc (USA)*, **72** (1950) 3443.
- 12 Chandra S & Prakash J, *J Chem Phys (USA)*, **54** (1971) 5366.
- 13 Chandra S & Prakash J, *J Phys Chem (USA)*, **75** (1971) 2616.
- 14 Gopalakrishna K V, *Trans Faraday Soc (GB)*, **53** (1957) 767.
- 15 Prakash J, *Indian J Pure & Appl Phys*, **8** (1970) 106.
- 16 Higasi K & Smyth C P, *J Am Chem Soc (USA)*, **82** (1960) 4759.



## Study of $^{50}_{22}\text{Ti}$ Ion Tracks in Soda Glass

SUBHASH CHANDER, SHYAM KUMAR, J S YADAV,  
S K GUPTA & A P SHARMA\*

Department of Physics, Kurukshetra University, Kurukshetra  
132 119

Received 27 July 1982; revised received 31 December 1982

The pre-annealed and pre-etched samples of soda glass are irradiated vertically by  $^{50}_{22}\text{Ti}$  ions of energy 4.9 MeV/N from the Joint Institute of Nuclear Research, Dubna, USSR. These irradiated samples are etched in the etchant 48 vol % HF + 96 vol %  $\text{H}_2\text{SO}_4$  +  $\text{H}_2\text{O}$  in the ratio 6:1:18. The bulk etch rate is measured at different etching temperatures and the activation energy for bulk etching is calculated. The etchpit diameter is also measured with etching time at different etching temperatures. The etched length for tracks of  $^{50}_{22}\text{Ti}$  ion of energy 4.9 MeV/N is measured. The energy loss and the range of  $^{50}_{22}\text{Ti}$  ion in soda glass are calculated theoretically. Comparing the total etchable track length with the theoretical range, the value of critical threshold for etchable track formation is obtained.

During the last two decades, solid state nuclear track detectors (SSNTDs) have found increasing use in various fields<sup>1-3</sup>. Their small weight, mechanical ruggedness, freedom from distortion, easy accessibility and low cost are some of their potential advantages. Glass detectors are one of the important members of SSNTD family. Glass detectors due to their higher threshold for registration of tracks can discriminate the light ionizing particles and are less prone to environmental effects. Thus their use is preferable in certain studies of nuclear physics (low as well as high energy physics), astrophysics and geophysics.

In the present work, we have measured the bulk etch rate of soda glass at different temperatures to calculate activation energy for bulk etching. The etchpit diameter has been measured as a function of etching time. The total etchable track length for  $^{50}_{22}\text{Ti}$  ion tracks has also been measured. The energy loss and the range of  $^{50}_{22}\text{Ti}$  ion in soda glass have been calculated theoretically and compared with the experimental value of total etchable track length to obtain the critical energy loss  $(dE/dx)_{\text{crit}}$  for etchable tracks formation.

**Experimental Details**—Pre-annealed and pre-etched samples of soda glass plates (backing with the nuclear emulsion stack K, composition given in Table 1) were exposed to  $^{50}_{22}\text{Ti}$  ion beams of energy 4.9 MeV/N (N signifies nucleon) vertically from heavy ion accelerator at the Joint Institute of Nuclear Research Dubna, USSR. The pre-irradiation annealing was done to remove/decrease the background tracks and the pre-irradiation etching to

Table 1—Composition of Soda Glass

Oxide	Composition wt %
$\text{SiO}_2$	69.87
$\text{Al}_2\text{O}_3$	4.83
$\text{Fe}_2\text{O}_3$	0.42
$\text{CaO}$	8.00
$\text{MgO}$	3.02
$\text{B}_2\text{O}_3$	1.00
$\text{Na}_2\text{O}$	12.38
$\text{K}_2\text{O}$	0.48

enlarge the background tracks so that they could be distinguished from the tracks registered during irradiation. The exposed samples were etched in the etchant 48 vol % HF + 96 vol %  $\text{H}_2\text{SO}_4$  +  $\text{H}_2\text{O}$  in the ratio 6:1:18 at temperatures 40, 50, 60 and 70°C ( $\pm 1^\circ\text{C}$ ) by using the thermostatically controlled incubator<sup>4</sup>.

The bulk etch rate of the soda glass was measured using the thickness difference measurement technique. A micro-thickness difference measurement technique. A micro-thickness gauge with least count of 2  $\mu\text{m}$  was employed for measuring the thickness of the sample. Microscopic observations were made using a transmitted light microscope 'Olympus' BH having an eyepiece screw micrometer with least count of 0.215  $\mu\text{m}$  for the total magnification of 900  $\times$  (using an objective of 40 $\times$ ). To have a better contrast between the contour of the tracks and the background, the phase contrast technique was used to reduce the error in diameter measurement which might otherwise be up to 1  $\mu\text{m}$ .

**Results and Discussion**—The energy loss rate  $(dE/dx)$  for this ion was calculated using the range-energy equations given by Mukherjee and Nayak<sup>5</sup> which give the elemental stopping power. Different equations valid at different ion energy ranges during the passage of the ion through the medium were used. Assuming the validity of Bragg's additive rule, the stopping power of complex media  $[(dE/dx)_c]_E$  at the ion energy  $E$  in terms of stopping powers of constituent elements  $(dE/dx)_i$  at the same ion energy  $E$  is given as

$$\left[\left(\frac{dE}{dx}\right)_c\right]_E = \frac{1}{A_c} \sum_i y_i A_i \left\{\left(\frac{dE}{dx}\right)_i\right\}_E \quad \dots (1)$$

where  $A_c (= \sum_i A_i y_i)$  is the molecular mass number of the medium,  $A_i$  and  $y_i$  are respectively the mass number and number of atoms per molecule of the  $i$ th atomic species.



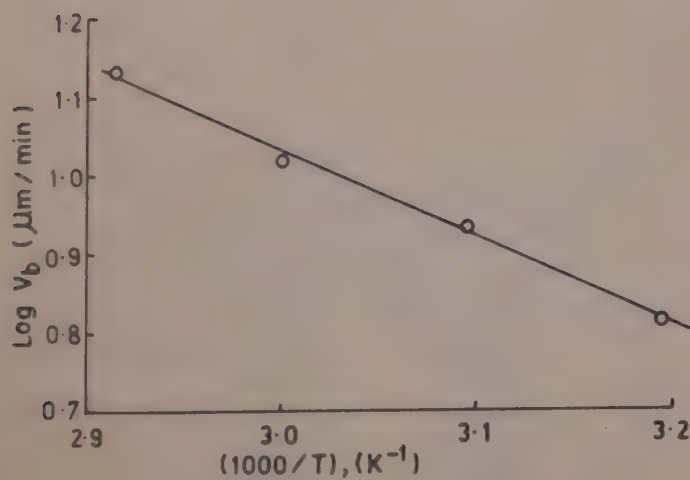


Fig. 1—Log  $V_b$  versus  $1000/T$

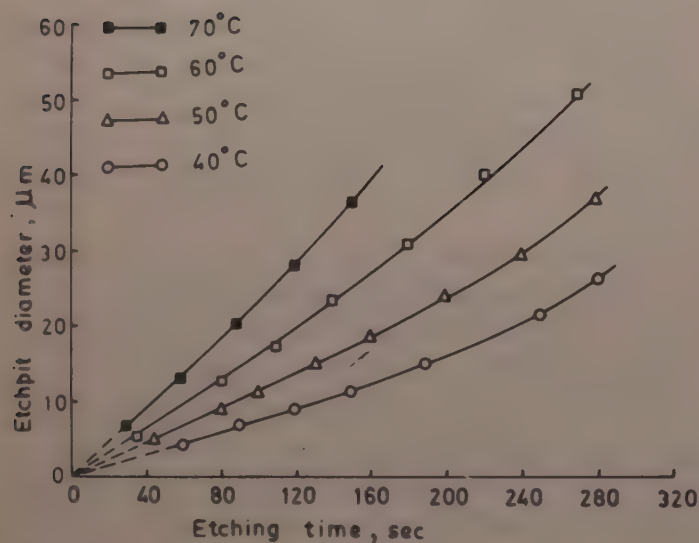


Fig. 2—Variation of etchpit diameter with etching time at different temperatures

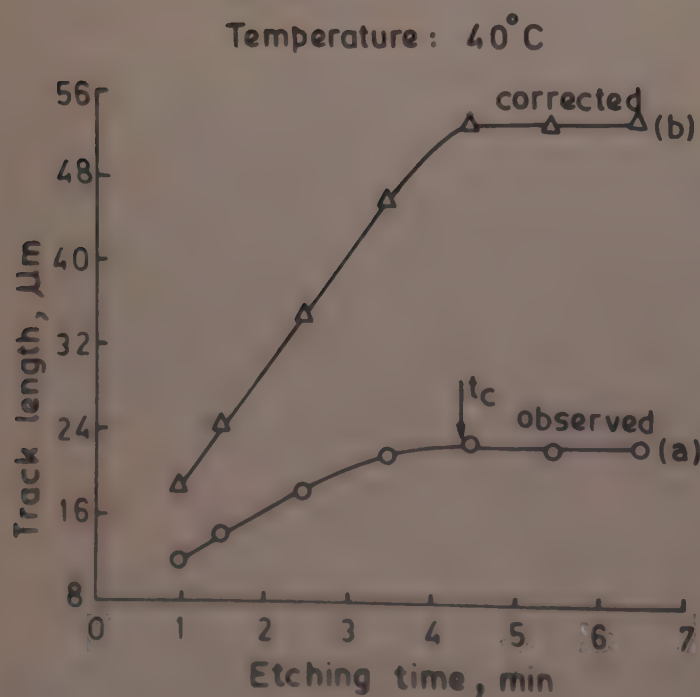


Fig. 3—Track length: (a), observed; (b) corrected, versus  $t$

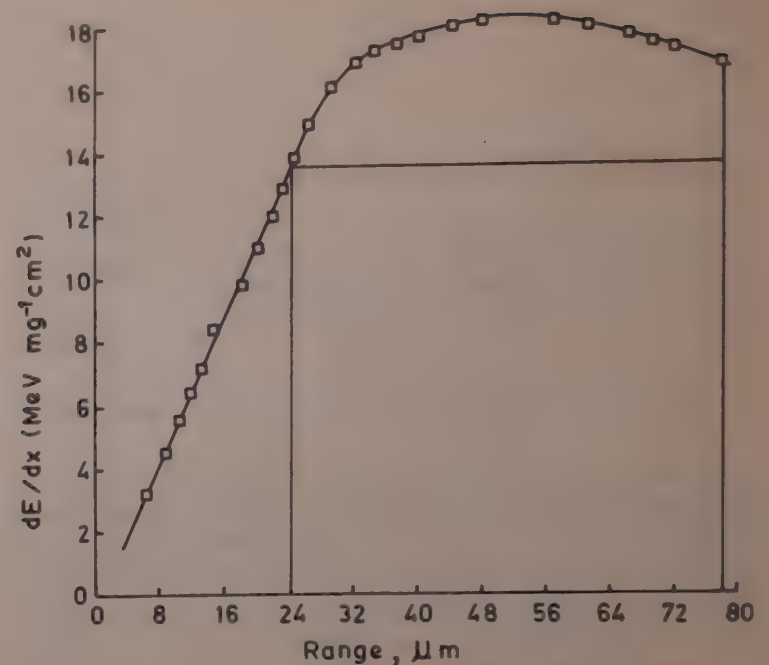


Fig. 4—Variation of  $dE/dx$  with penetration depth (calculated theoretically)

The range (in  $mg/cm^2$ ) is given by

$$\text{Range} = \sum_{E=E_0}^E \frac{\delta E}{[(dE/dx)_c]_E} \quad \dots (2)$$

Here  $(dE/dx)$  is in  $MeV mg^{-1}cm^2$   
 $E_0$  corresponds to  $V_0 = e^2/h$

where  $V_0$  is the electron velocity in hydrogen atom and  $\delta E (= 0.05 MeV)$  the small energy interval over which  $dE/dx$  is assumed to be constant.

The range (in  $\mu m$ ) is given by

$$\text{Range (in } \mu m) = \text{Range (in } mg/cm^2) \times 10.0/\text{density} \quad \dots (3)$$

The measured values of bulk etch rate ( $V_b$ ) varies exponentially with etching temperature ( $T$ ) and can be represented by the following relation

$$V_b = Ae^{-E_b/kT} \quad \dots (4)$$

where  $A$  is a constant,  $E_b$  the activation energy for bulk etching and  $k$  the Boltzmann constant. From the slope of the straight line obtained by plotting a graph between  $\log V_b$  and  $1/T$  (Fig. 1), the value of  $E_b$  is found to be  $22.69 \times 10^{-2} eV$ .

The measured values of etchpit diameter are plotted against etching time (Fig. 2). These results show: (1) the etchpit diameter increases more rapidly at higher  $T$  obviously due to increased etch rate at higher  $T$ , and (2) the slope of the curve increases continuously because the energy loss increases with penetration depth until energy is degraded to  $\sim 1.5 MeV/N$  (the position of Bragg peak in energy loss curve) and after this, the energy loss starts decreasing. The later situation corresponds to a few microns at the end of the track.



Fig. 3(a) shows the variation of observed track length ( $L_{\text{obs}}$ ) with etching time  $t$ .  $L_{\text{obs}}$  increases with  $t$  and after a certain value of  $t$ , called the complete etching time ( $t_c$ ),  $L_{\text{obs}}$  becomes constant. It is due to the fact that, before complete etching, the track etch rate  $V_t > V_b$ ; so track length increases and after complete etching,  $V_t$  becomes equal to  $V_b$  and the track length becomes constant.  $L_{\text{obs}}$  is corrected for surface etching and for overetching using the relation

$$L_c = L_{\text{obs}} + V_b t - V_b(t - t_c) \quad \dots (5)$$

Corrected track length ( $L_c$ ) is plotted against  $t$  (Fig. 3b). The terms  $V_b t$  and  $V_b(t - t_c)$  are the correction factors for surface etching and overetching respectively. The term  $V_b(t - t_c)$  is zero for  $t \leq t_c$ . The total etchable track length for  $^{50}_{22}\text{Ti}$  ion tracks of energy 4.9 MeV/N after correction comes out to  $53.5 \pm 1 \mu\text{m}$ . By comparing the value of the total etchable track

length with the theoretical value of range, we have obtained the value of critical threshold  $(dE/dx)_{\text{crit}}$  for etchable track formation in soda glass as  $13.50 \pm 0.5 \text{ MeV mg}^{-1}\text{cm}^2$  (Fig. 4).

The authors are grateful to Prof. V P Perelygin of the Joint Institute of Nuclear Research, Dubna, USSR, for providing the exposed samples. One of the authors (SK) is thankful to the CSIR, New Delhi, for providing the financial assistance.

## References

- 1 Fleischer R L, Price P B & Walker R M, *Nuclear tracks in solids* (University of California Press, Berkeley), 1975.
- 2 Fleischer R L, *Nucl Instrum & Methods (Netherlands)*, **147** (1977) 1.
- 3 Khan H A & Durrani S A, *Radiat Eff (GB)*, **17** (1973) 133.
- 4 Gomber K L, Yadav J S, Singh V P & Sharma A P, *Can J Phys (Canada)*, **39** (1981) 693.
- 5 Mukherji Shanker & Nayak A K, *Nucl Instrum & Methods (Netherlands)*, **159** (1979) 421.



## Electronic & Infrared Absorption Spectra of 3-Methylpyridazine

NARASIMHA H AYACHIT, K SURYANARAYANA RAO & M A SHASHIDHAR\*

Department of Physics, Karnatak University, Dharwad 580 003

Received 10 August 1982; revised received 24 February 1983

The electronic and infrared absorption spectra of 3-methylpyridazine have been recorded and analyzed. The observed fundamentals and their assignments are reported.

The electronic states of azabenzenes have been studied in great detail by many workers both experimentally and theoretically<sup>1</sup>. Although the 3700 Å system of pyridazine presents a complex vibrational structure, its vibrational analysis was proposed by Tincher<sup>2</sup>. The rotational analysis proposed by Innes<sup>3</sup>, shows that the 3700 Å system is due to the  $^1B_1 \leftarrow ^1A_1$  transition. We have studied the electronic spectra of some substituted azines<sup>4-8</sup>, and in this note the details of the investigation of the infrared and ultraviolet absorption spectra of 3-methylpyridazine are reported.

The sample used was obtained from Aldrich Chemical Co., USA and was stated to be very pure. The electronic absorption spectrum of 3-methylpyridazine was photographed on a Littrow spectrograph using absorption columns of lengths varying from 50 to 100 cm and temperature of the absorbing vapour varying from 10 to 100°C. As the infrared data for this molecule were not available in literature, the same were recorded on a Perkin-Elmer Model 221 automatic spectrophotometer in the pure liquid phase and the instrument was calibrated using an error graph.

Pyridazine has been assigned to the point group  $C_{2v}$  by Innes *et al.*<sup>3</sup>. After substitution of the methyl group, in the 3 position in the pyridazine ring and considering the methyl group to behave as a single mass point and lying in the plane of the ring, 3-methylpyridazine may be considered as belonging to the point group  $C_s$ .

The total number of 33 normal modes of vibrations are then divided into two species  $23a' + 10a''$ . The infrared spectrum of 3-methylpyridazine has been analyzed with the help of the analyzed data of pyridazine<sup>2</sup>, deuterated pyridazines<sup>9</sup> and 3, 6-dichloropyridazine<sup>10</sup>. The observed fundamentals and their visually estimated relative intensities together with their assignments are given in Table 1.

The electronic absorption spectrum of this molecule lies in the region  $\lambda$  3580- 3345 Å and consists of rather narrow bands which are degraded to the red. This band

Table 1—Fundamental Vibrational Frequencies (in  $\text{cm}^{-1}$ ) of 3-Methylpyridazine

Position and intensity* of the bands	Assign	Position and intensity* of the bands	Assign
220 ms	$\gamma_{C-CH_3}$	1185 m	$\nu_{C-CH_3}$
345 s	$\nu_{16a}$	1250 vs	$\nu_3$
420 w	$\beta_{C-CH_3}$	1330 ms	$\nu_{14}$
500 mw	$\nu_{16b}$	1350 ms	$CH_3$ sym def
550 s	$\nu_{6a}$	1380 s	$\nu_{19b}$
635 s	$\nu_{6b}$	1430 s	$\nu_{19a}$
730 sh	$\nu_{11}$	1455 m	$CH_3$ asym def
740 s	$\nu_4$	1470 sh	$CH_3$ asym def
785 s	$\nu_{10}$	1545 s	$\nu_{8b}$
800 s	$\nu_1$	1575 vs	$\nu_{8a}$
940 m	$\nu_{17a}$	2850 m	$CH_3$ sym str
1000 s	$\nu_{12}$	2920 ms	$CH_3$ asym str
1035 s	$CH_3$ rock	2950 ms	$CH_3$ asym. def.
1075 s	$\nu_{15}$	3050 s	$\nu_{20a}$
1090 s	$CH_3$ rock	3070 sh	$\nu_{13}$
1150 s	$\nu_{9a}$	3090 w	$\nu_{7b}$

\*m = medium; ms = medium strong; w = weak; mw = medium weak; s = strong; vs = very strong; sh = shoulder; sym = symmetric; def = deformation; asym = asymmetric; str = stretch; Assign = Assignment.

system corresponds to the  $^1B_1 \leftarrow ^1A_1$  transition in pyridazine. It has been analyzed with the help of our infrared data and also with the help of the corresponding spectra of pyridazine<sup>2</sup> and 3, 6-dichloropyridazine<sup>10</sup>.

The study of the effect of temperature on the band system has facilitated the choice of the band at  $26736 \text{ cm}^{-1}$  as the 0, 0 band. The  $\nu_1$  vibration ( $992 \text{ cm}^{-1}$ ) in the spectrum of benzene represents the C—C stretching vibration. In the spectrum of substituted benzenes, this vibration has been found to be mass dependent and has been identified up to  $700 \text{ cm}^{-1}$  in the ultraviolet, infrared and Raman spectra depending on the mass and nature of the substituent<sup>11,12</sup>. Studies on the vibrational spectra of pyridazine<sup>2</sup> and some of its deuterated analogues show that this vibration is mass dependent. From all these considerations, it appears that the  $\nu_1$  vibration is dependent on the mass of the substituent. In the electronic absorption spectrum of 3-methylpyridazine a strong excited state fundamental at  $722 \text{ cm}^{-1}$ , which may be correlated with the ground state fundamental  $800 \text{ cm}^{-1}$  (the corresponding infrared frequency being  $800 \text{ cm}^{-1}$ ), has been observed. This excited state fundamental  $722 \text{ cm}^{-1}$  has been found to combine with most of the other fundamentals and is also excited



up to 3 quanta. Therefore, it can be taken as a totally symmetric vibration and has been assigned to the  $\nu_1$  vibration in benzene.

In the spectrum of benzene,  $\nu_6$  represents the carbon planar deformation vibration of  $e_{2g}$  type. Under  $C_s$  point group the degeneracy is removed and the two vibrations appear separately and they will have totally symmetric character. Studies on the infrared spectrum of pyridazine<sup>2</sup> and some of its deuterated compounds<sup>9</sup> show that the lower component is mass dependent while the higher one remains around  $640\text{ cm}^{-1}$ . In the present electronic spectrum, two strong excited state fundamentals at  $463\text{ cm}^{-1}$  (appearing up to 3 quanta) and  $580\text{ cm}^{-1}$  have been observed. These two fundamentals combine with most of the other fundamentals in the excited state. The corresponding ground state fundamentals are at  $553$  and  $635\text{ cm}^{-1}$  which agree well with the infrared bands at  $550$  and  $635\text{ cm}^{-1}$  respectively. These vibrations may be assigned as the components of  $\nu_6$  vibration in benzene. The excited state fundamentals  $1197$  and  $1314\text{ cm}^{-1}$  may be correlated with the infrared bands at  $1330$  and  $1430\text{ cm}^{-1}$  respectively. They form combinations with other totally symmetric excited state fundamentals and in the analyzed spectra of pyridazine<sup>2</sup>, frequencies around these values have been assigned to the C—C stretching mode. Accordingly, the excited state fundamentals  $1197$  and  $1314\text{ cm}^{-1}$  may correspond to  $\nu_{14}$  and  $\nu_{19a}$  vibrations in benzene respectively.

The medium strong excited state fundamentals  $942$  and  $1037\text{ cm}^{-1}$  may be correlated with the infrared bands at  $1000$  and  $1150\text{ cm}^{-1}$ . They occur in some cases up to 2 quanta and form combination with other totally symmetric vibrations. They may represent respectively  $\nu_{12}$  and  $\nu_{9a}$  vibrations in benzene. In the electronic absorption spectra of similar molecules, fundamentals around these values have been attributed to the above said vibrations.

The excited state fundamentals  $1137$  and  $380\text{ cm}^{-1}$  (ground state frequency being  $415\text{ cm}^{-1}$ ) corresponding to the infrared bands at  $1185$  and  $420\text{ cm}^{-1}$  which form combination with the other totally symmetric vibrations may be assigned to the C—CH<sub>3</sub> stretching and C—CH<sub>3</sub> in-plane bending vibrations, in accordance with the assignment that has been made in several of the methyl substituted benzenes studied<sup>13–16</sup>.

In 3-methylpyridazine, sequences of  $27$  and  $120\text{ cm}^{-1}$  are observed and they may be assigned in accordance with the assignment made in pyridazine<sup>2,3</sup> and 3,6-dichloropyridazine<sup>10</sup> to the 1-1 transitions of  $\nu_{16b}$  and  $\nu_{16a}$  in benzene respectively. These difference frequencies are used in assigning some of the less prominent bands. Similar values of frequencies were

Table 2—Prominent Absorption Bands (in  $\text{cm}^{-1}$ ) of 3-Methylpyridazine

Wavenumber and intensity*	Assign	Wavenumber and intensity*	Assign
25936 m	0,0–800	27773 ms	0,0+1037
26064 w	0,0–553–120	27846 mw	0,0+380+722
26101 mw	0,0–635	27873 ms	0,0+1137
26156 mw	0,0–553–27	27882 mw	0,0+3×380
26183 m	0,0–553	27933 ms	0,0+1197
26198 w	0,0–415–120	28056 m	0,0+1314
26293,	0,0–415–27	28068 w	0,0+380+942
26321 ms	0,0–415	28090 w	0,0+1037+316
26590 w	0,0–120–27	28133 mw	0,0+3×463
26616 ms	0,0–120	27176 mw	0,0+2×722
26709 s	0,0–27	28223 w	0,0+463+1037
26736 vs	0,0	28256 w	0,0+380+1137
26878 mw	0,0+942–800	28317 w	0,0+380+1197
26992 mw	0,0+380–120	28395 w	0,0+463+1197
37042 w	0,0+942–635	28436 w	0,0+380+1314
27116 s	0,0+380	28460 w	0,0+580+1137
27175 ms	0,0+463–27	28506 w	0,0+463+1314
27199 s	0,0+463	28594 w	0,0+4×463
27268 m	0,0+942–415	28627 m	0,0+2×942
27297 ms	0,0+1197–635	28647 w	0,0+722+1197
27316 ms	0,0+580	28779 w	0,0+722+1314
27355 m	0,0+1037–415	28819 mw	0,0+2×1037
27430 mw	0,0+722–27	28900 mw	0,0+3×722
27458 s	0,0+722	29004 mw	0,0+2×1137
27495 m	0,0+2×380	29063 w	0,0+1137+1197
27581 mw	0,0+380+463	29136 w	0,0+2×1197
27650 mw	0,0+942–27	29375 w	0,0+2×1314
27661 m	0,0+2×463		
27678 ms	0,0+942		
27744 mw	0,0+1037–27		

\* W=weak; mw=medium weak; m=medium; s=strong; ms=medium strong; vs=very strong; Assign = Assignment

observed in pyrazine<sup>17</sup> and they were also assigned in a similar way by others<sup>4–8,17</sup>.

The prominent absorption band data and their probable assignments are given in Table 2.

One of the authors (NHA) is thankful to the CSIR, New Delhi, for the award of a Junior Research Fellowship.

## References

- 1 Innes K K, Byrne J P & Ross I G, *J Mol Spectrosc (USA)*, **22** (1967) 125.
- 2 Tincher W C, *Vibrational analysis of the  $\pi^* \leftarrow n$  transition of pyridazine*, Ph D thesis, Vanderbilt University, Tennessee, USA, 1960.
- 3 Innes K K, Tincher W C & Pearson E, *J Mol Spectrosc (USA)*, **36** (1970) 114.
- 4 Shashidhar M A, *Indian J Pure & Appl Phys*, **12** (1974) 726.
- 5 Shashidhar M A & Suryanarayana Rao K, *Indian J Phys*, **49** (1975) 128.
- 6 Shashidhar M A & Suryanarayana Rao K, *Indian J Pure & Appl Phys*, **14** (1976) 689.
- 7 Narasimha H Ayachit & Shashidhar M A, *Indian J Phys*, **B56**, (1982) 124.



- 8 Narasimha H Ayachit & Shashidhar M A, *Indian J Phys*, **B56** (1982) 313.
- 9 Stidham H D & Tucci J C, *Spectrochim Acta (GB)*, **A23** (1967) 2233.
- 10 Nitish K Sanyal, Srivastava S L, Goel A K & Sharma S D, *Proc Indian Acad Sci Sect A*, **88** (1979) 279.
- 11 Whiffen D N & Stojiljlovic A, *Spectrochim Acta Vol A (GB)*, **12** (1950) 42.
- 12 Whilmsharst J K & Bernstein H J, *Can J Chem (Canada)*, **35** (1957) 911.
- 13 Shashidhar M A, *Indian J Pure & Appl Phys*, **12** (1974) 532.
- 14 Singh R N, Prasad S C & Prasad P K, *Spectrochim Acta Vol A (GB)*, **34** (1978) 39.
- 15 Fox J J & Martin A E, *Proc Soc, London (GB)*, **175** (1940) 208.
- 16 Mooney F F, *Spectrochim Acta (GB)*, **20** (1964) 134.
- 17 Hirt R C, *Spectrochim Acta (GB)*, **12** (1958) 114.



## SCOPE

The journal welcomes, for publication, full papers and short notes, reporting significant new results of research, in all areas of physics except space physics. The applied fields covered are electronics, electrical engineering, instrumentation and applied mathematics. However, papers in applied mathematics with emphasis on only derivation and proofs and having no direct physical significance, will not be considered. Review articles are not published normally.

## SUBMISSION OF MANUSCRIPT

Manuscripts for consideration should be submitted, *in duplicate*, to Editor, Indian Journal of Pure & Applied Physics, Publications & Information Directorate, Hillside Road, New Delhi 110012. They should neither have been already published nor be under consideration elsewhere.

Manuscripts should be in English and typewritten on only one side of good quality paper, in double space, with adequate margin on all four sides. One original and one carbon or photo-copy, each complete in all respects including abstract, illustrations, appendixes, etc. are to be submitted.

## PREPARATION OF MANUSCRIPT

Authors may consult recent issues of the Journal to familiarize themselves with the general style and practices adopted in regard to the various elements of a paper.

### General

Manuscript should be presented in as concise a form as possible. Good attention should be given to spelling and grammar. In giving names of chemical compounds and structures, abbreviations of units of measurements, symbols and notations, the style and practices recommended by the IUPAP and IUPAC, should be followed.

Frequently repeating combinations of words, e.g. electric field gradient (EFG), junction field effect transistor (JFET), stimulated Raman emission (SRE), should be abbreviated subsequently, indicating the abbreviated form in parenthesis, as shown, at the place of their first occurrence.

Pages should be numbered consecutively and arranged in the following order: Title, authors' names with their institutional affiliations and abstract, along with relevant footnotes whenever necessary (on a separate sheet); introduction; experimental details/theory/method/analysis; results; discussion; conclusion(s); acknowledgement; references and appendixes. Tables, captions for figures (with legends) and appendixes should be typed *on separate sheets* and attached at the end of the manuscript.

### Title

The title should be neither too brief/general nor unnecessarily long. It should reflect the content of the paper so as to derive the maximum advantage in indexing. If a paper forms part of a general series, a specific subtitle, indicating the particular aspect of the work covered in the paper, should be provided.

A short running title for the paper, the broad subject heading under which it should be classified in the contents page (authors may consult recent numbers of the journal for this purpose), and the author (indicated by an asterisk on the relevant author's name) and address for correspondence, should also be provided on the title page.

### Abstract

The abstract, usually not exceeding 200 words, should indicate the scope and significant content of the paper,

highlighting the principal findings and conclusions. It should be in such a form that abstracting periodicals can use it without modification.

## Introduction

Long and elaborate introduction should be avoided. It should be brief and state the exact scope of the study in relation to the present status of knowledge in the field. Literature review should be limited strictly to what is necessary to indicate the essential background and the justification for undertaking the study.

## Materials, methods, apparatus, etc.

The sources of materials and their purity, methods of preparation, procedure for measurements and their accuracies, etc. should be clearly stated to enable any other worker to repeat the work if necessary. New methods, techniques, theories, etc. should be described in adequate detail; but if they are well known, a mere literature reference to them will do; differences from standard ones, improvements or innovations should, however, be clearly mentioned.

## Results

Only such primary data as are essential for understanding the discussion and main conclusions emerging from the study should be included. All secondary data as are of interest to a specific category of readership *should not be included* in the paper. Such data should be retained by the authors for supply, on request, to any interested research worker. A footnote to this effect may be inserted at the relevant place in the paper.

The results must be presented in a coherent sequence in a unified logical structure, avoiding repetition or confusion. Limitations of the results should be clearly stated.

The same data should not be presented in both tabular and graphic forms. Only such tables and figures as are essential should be included. Simple linear plots that can easily be discussed in the text, should not be included. Infrared, ultraviolet, NMR and other spectra, DTA curves, etc. should be included only if they pertain to new compounds and/or are essential to the discussion; otherwise only significant numerical data should be given in the text or in a table.

## Discussion

Long rambling discussion should be avoided. The discussion should deal with the interpretation of results without repeating information already presented under results. It should relate new findings to the known and include logical deductions. A separate section on 'conclusions' can be given only when they are well established and of outstanding significance. Mere observation of qualitative trends of results should be distinguished from firm conclusions. Also, limitations, if any, to the conclusions should be clearly pointed out.

## Mathematical portions

Special attention should be given to the mathematical portions of the paper. Equations must be well separated from the text and written clearly with good separation between the successive lines. The usual norms of breaking long mathematical expressions should be adhered to. Equations should be numbered consecutively in Arabic numerals with the number in parenthesis near the right hand margin. Superscripts and subscripts should be clearly indicated in pencil by V and  $\wedge$  sign respectively. Capital and small letters,



particularly of the same letter when both occur, as well as letters or symbols likely to be confused one for the other, should be clearly distinguished. Special characters (e.g. Greek, script, vector, tensor, etc.) required must be indicated by marginal notes. Letters and symbols which should appear in bold face must be clearly indicated. To simplify typesetting: (i) long and complicated mathematical expressions which are frequently repeated should be replaced with single letter/symbol, without clashing with the others used in the paper; (ii) the "exp" form of complex exponential functions should be used; and (iii) to simplify fractions, the solidus (/) is to be used and fractional exponents are to be used instead of root signs, e.g.

write  $\exp\{-i\omega_0(t_1 - t_2)/2\}$  and not  $e^{-i\omega_0(t_1 - t_2)/2}$

write  $(4\omega_{pl} K_{3\lambda}^2 / \tilde{\omega} K_D^2)^{1/2}$  and not  $\sqrt{\frac{4\omega_{pl} K_{3\lambda}^2}{\tilde{\omega} K_D^2}}$

## Tables

Tables should be numbered consecutively in Arabic numerals and should bear brief titles. Column headings should be brief. Units of measurement should be abbreviated and placed below the headings. Nil results should be indicated and distinguished clearly from absence of data. Inclusion of structural formulae inside the tables should be avoided as far as possible. Tables should be referred to in the text by numbers and not by terms like 'above', 'below', 'preceding' or 'following'. Results should not be presented to a greater accuracy than that of the method employed.

## Illustrations

The number of illustrations should be kept to the minimum. Wherever possible, e.g. a number of individual analogous figures referring to different variables, substances, molecules, etc. may be combined into one composite figure. All illustrations should be numbered consecutively in Arabic numerals. Captions and legends to the figures should be self-explanatory. Line drawings should be made with Indian ink on white drawing paper/cellophane sheet/tracing cloth, and drawn to approximately twice the printed size.

The lettering should be uniform, preferably in stencil, so as to be not less than 1.5 mm after reduction widthwise to full page size (165 mm) or column size (80 mm). The size of geometrical shapes (used to distinguish different graphs), dots, lines, etc. should be sufficiently large to permit the necessary reduction without loss of detail. In the case of photographs, prints must be on glossy paper and contrasty. If an illustration is taken from another publication, reference to the source should be given and prior permission secured. Illustrations should be referred to in the text by numbers and not by terms like 'above', 'following' etc.

## Acknowledgement

Acknowledgements should not be exuberant and must be made only to real assistance rendered in connection with the work reported in the paper.

## References

References cited should be limited to the absolute minimum (particularly in the case of short notes) based on their essential relevance. In the text, references to literature should be numbered consecutively, in the order of their first occurrence, and should be indicated by superscript Arabic numbers at the relevant places; as far as possible the placement of references on numerals or other symbols should be avoided; in such cases the reference may be given in parenthesis in running text, e.g. "this yielded for  $n$  a value of 2.3 (Ref. 5)". Full bibliographic details for all the references mentioned in the text should be listed in serial order at the end of the paper.

In citing references to research papers, names and initials of authors should be followed, in order, by the title of the periodical in the abbreviated form (underlined), the volume number (two lines underneath), the year within circular brackets and the page number [e.g. Chandra B P & Shrivastava K K, *J Phys & Chem Solids (GB)*, 39 (1978) 939]. For names of periodicals, the abbreviations followed by the *Physics Abstracts* should be used. For periodicals not covered by *Physics Abstracts*, the title abbreviations should be according to the *Bibliographic Guide for Editors and Authors*, 1974, published by the American Chemical Society, Washington DC, USA; additionally the country from which the journal is published should be given in parenthesis immediately after the title abbreviation. If a paper has been accepted for publication, the names of the authors and the journal (with volume number and year, if known) should be given followed by the words "in press" [e.g. Wahi P K & Patel N D, *Can J Spectrosc (Canada)*, in press.].

In references containing up to four authors, the names of all the authors with their respective initials should be given. The abbreviations *et al.*, *idem* and *ibid* should be avoided. When there are more than four authors, only the names of the first three authors with their respective initials should be given, followed by the words 'et al.'

Reference to a book should include details in the following order: name and initials of authors, the title of the book (underlined), name of publisher and place of publication within circular brackets and year and page (s) [e.g. Clayton G B, *Operational amplifiers* (Newnes-Butterworths, London), 4th Edn, 1977, 26]. If the reference is to the work of an author published in a book by a different person, the fact that it is cited from the source book should be clearly indicated [e.g. Turnhout Van J, 'Thermally stimulated discharge of electrets' in *Topics in applied physics*: Vol. 33—*Electrets*, edited by C M Sessler (Springer Verlag, Berlin), 1980, 130].

Proceedings of conferences and symposia should be treated in the same manner as books. Reference to a paper presented at a conference, the proceedings of which are not published, should include, in the following order, names and initials of authors, title of the paper (underlined), name of the conference, and where and when it was held (e.g. Herczeg P, *Symmetry-violating kaon decays*, paper presented to the International Conference on High Energy Physics and Nuclear Structure, Vancouver, Canada, 13-17 August 1979).

Reference to a thesis should include the name of the author, title of the thesis (underlined), university or institution to which it was submitted and year of submission (e.g. Mehrotra S N, *Many-body techniques and their applications to interacting bosons*, Ph D thesis, Ranchi University, 1976).

Reference to a patent should include names of patentees, country of origin (underlined) and patent number, the organization to which the patent has been assigned (within circular brackets), date of acceptance of the patent and reference to an abstracting periodical where available [e.g. Labes M M, *US Pat.* 4,066,567 (to Temple University), 3 January 1978; *Chem. Abstr.*, 88 (No. 20) (1978), 138350 n].

## PROOFS & REPRINTS

Authors will receive galley proofs and a reprint order form. The galley proofs, indicating the essential corrections, should be returned to the Editor without delay, enclosing the reprint order form. Authors are given 25 free reprints for each paper. Extra reprints can be had at cost. If the reprint order is not received with the corrected proofs, it will be presumed that the author needs no extra reprints. Later requests for more reprints cannot be complied with. Covers for reprints cannot be provided.



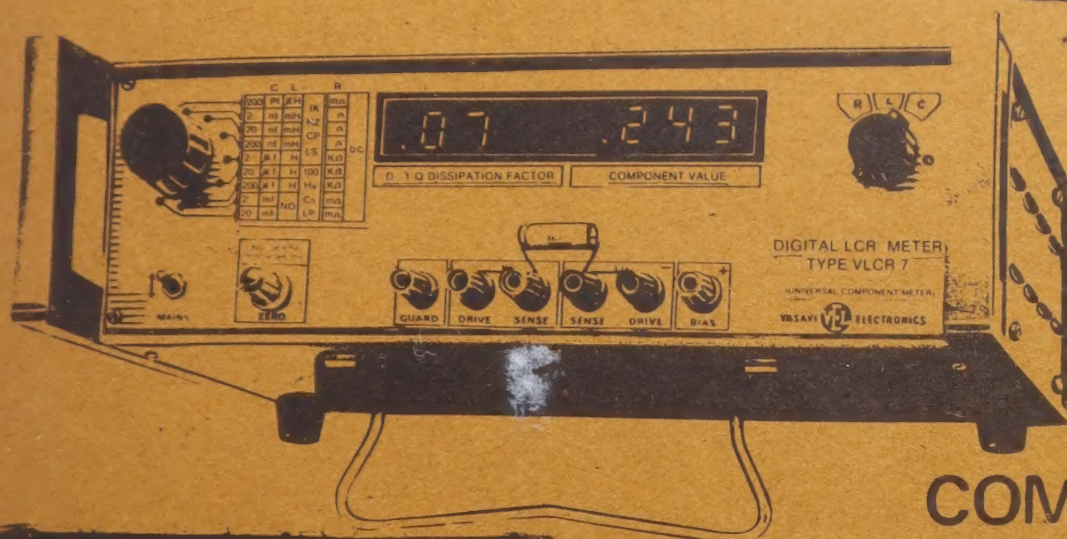
# VASAVI INTRODUCED

FOR YOU A WIDE RANGE  
OF DIGITAL LCR METERS

YOU NO MORE AVOID  
LCR MEASUREMENTS



ULTIMATE IN LCR METERS  
WITH WIDEST RANGE  
BEST RESOLUTION  
SIMPLEST OPERATION AND  
SIMULTANEOUS DISSIPATION  
FACTOR DISPLAY

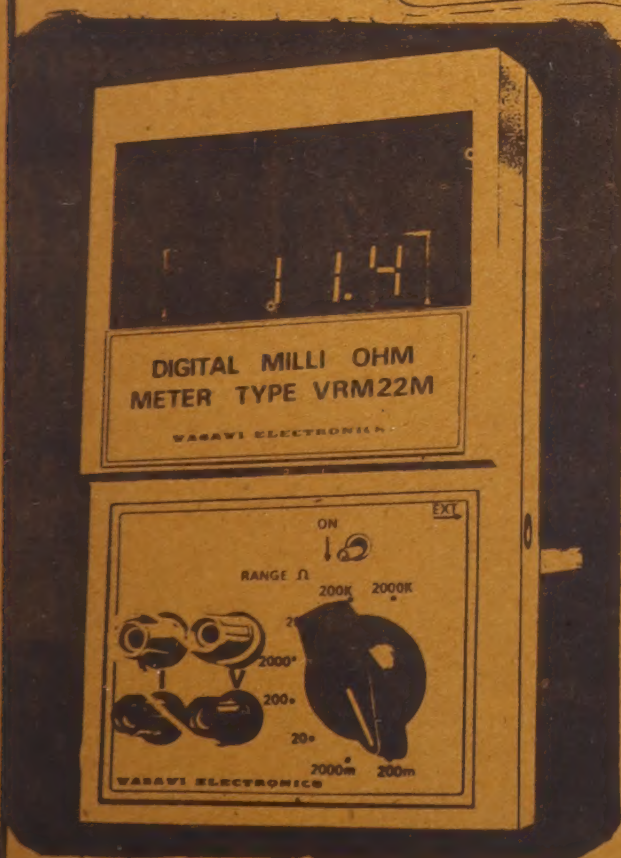


MODEL VLCR 7

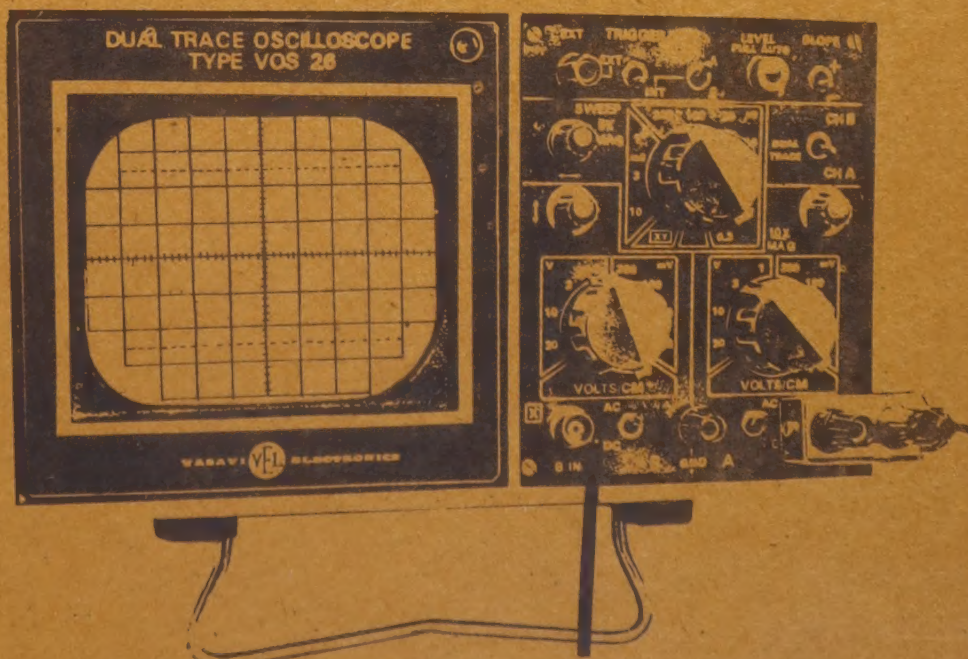
has the widest range

0.1 Pf/ $\mu$ H/m $\Omega$  (0.0001 $\Omega$ ) to  
20,000  $\mu$ F/200H/20 M $\Omega$

OSCILLOSCOPES  
with  
COMPONENT TESTER  
add new dimensions



VRM 22M 100 micro OHM resolution and employs 4 terminal measurement technique to overcome problems in low resistance measurement. VRM 22M operates on internal batteries and mains operation



AND OTHER **Digital** PRODUCTS

- Frequency Counter
- precision multimeter
- DC MICRO VOLT METER

For your requirements please write to

M/S VASAVI ELECTRONICS  
162, Vasavinagar, Secunderabad-500 005 (INDIA)  
Grams: VELSCOPE PHONE: 70995



# ECIL's proven range of Analytical Instruments...

... for accurate and reliable chemical analysis.

## Digital Spectrophotometer GS 5700

Wavelength range: 340 to 950 nm



### Features:

- Single beam grating monochromator
- High sensitive phototubes, (Blue and Red) as detectors premounted with selector knob

## Spectrophotometer GS865D

Covers the ultraviolet and visible spectrum from 200 to 650 nm, extendable to 930 nm.

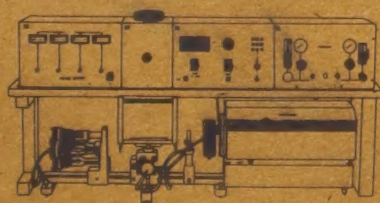


### Features:

- High resolution single beam, grating monochromator
- High sensitive Photomultiplier as radiation detector

## Atomic Absorption Spectrophotometer AAS4103

Employs a high resolution single beam, grating monochromator optics.

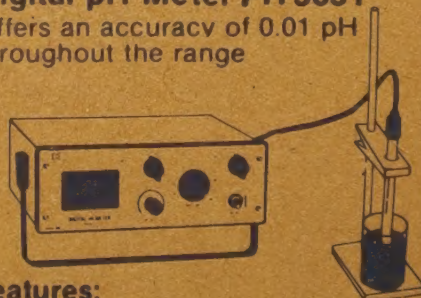


### Features:

- Modular design on optical rail
- Digital readout of absorbance, transmittance, concentration

## Digital pH Meter PH 5651

Offers an accuracy of 0.01 pH throughout the range



### Features:

- Digital LED display
- High degree of accuracy
- Range 0 to 14 pH and 0 to  $\pm 1999$  mv
- Readout — Digital LED display

## Fluorometer FL6209

Fluorescence from 1 ppm quinine sulphate in 0.1N sulphuric acid (primary 366 nm) produces full scale voltage



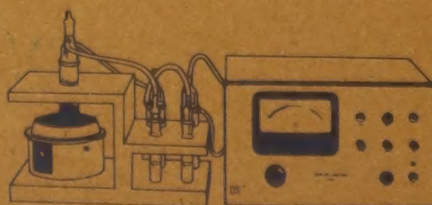
### Features:

- Mercury lamp as radiation source
- High sensitive photomultiplier detector
- $3\frac{1}{2}$  digit digital display

ECIL's range of Analytical Instruments, designed and manufactured to high standards, undergo several rigorous tests to ensure flawless performance. These rugged, reliable and precision-engineered instruments perform to their rated specifications and find application in research and industry.

## Mercury Analyser MA5800A

Offers a measuring range of 20 to 200 ng in solutions.



### Features:

- Determination of mercury in nanograms
- Cold vapour atomic absorption technique

# ECIL

Electronics Corporation of India Limited

(A Govt. of India — Dept. of Atomic Energy — Enterprise)

INSTRUMENTS GROUP — MARKETING, HYDERABAD 500 762

Tel: 78311 Telex: 0155 - 254 ECIL HD

Branches: BANGALORE BOMBAY CALCUTTA MADRAS NEW DELHI

Phones: 77072

4227760 240273

442339 311007